PB-241 806

RELATIONSHIP BETWEEN CIRCUMSOLAR SKY BRIGHTNESS AND ATMOSPHERIC AEROSOLS

ALASKA UNIVERSITY

JUNE 1974

DISTRIBUTED BY:

NTIS

National Technical Information Service
U. S. DEPARTMENT OF COMMERCE

TECHNICAL REPORT DATA
(Please read Instructions on the reverse before completing)

1. REPORT NO. EPA-650/4-75-012	2.
3.	PB 241 806
4. TITLE AND SUBTITLE: RELATIONSHIP BETWEEN CIRCUMSOLAR SKY BRIGHTNESS AND ATMOSPHERIC AEROSOLS	5. REPORT DATE: June 1974
	6. PERFORMING ORGANIZATION CODE
7. AUTHOR(S): Glenn E. Shaw and Charles S. Deehr	8. PERFORMING ORGANIZATION REPORT NO.
9. PERFORMING ORGANIZATION NAME AND ADDRESS: Geophysical Institute, University of Alaska, Fiarbanks, Alaska 99701	10. PROGRAM ELEMENT NO. 1AA009 ROAP No. 26AAS
	11. CONTRACT/GRANT NO. 801113
12. SPONSORING AGENCY NAME AND ADDRESS: Environmental Protection Agency-NERC, Meteorology Laboratory (MD-80), Research Triangle Park, N. C. 27711	13. TYPE OF REPORT AND PERIOD COVERED: Final Report 9/72-6/74
	14. SPONSORING AGENCY CODE

15. SUPPLEMENTARY NOTES

16. ABSTRACT

Measurements of the sky intensity in the solar vertical plane and in the solar almucantar were taken at an arctic location near Barrow, Alaska (71°19'N, 156°37'W), a sub-arctic location at Ester Dome, Alaska (64°53'N, 148°03'W), and a tropical station at Loiyengalani, Kenya (2°45'N,36°42'E). The data were used to obtain the aerosol scattering phase function for various synoptic conditions and air-mass types. The scattering phase functions were compared to calculated phase functions obtained by assuming various forms of the aerosol size distribution function. Based on the criteria of the best fit of the phase functions the corresponding aerosol size distribution function and the quasi-monochromatic optical depth, numerical estimates were made of the columnar aerosol mass loading. Typical of continental observations, a Junge power-law aerosol size distribution approximates the observed scattering phase function rather well. The observations indicate that the Junge power-law exponent, ν, depends upon air mass type and to a lesser extent on local climatological conditions. Relatively large values for the exponent (ν = 4.0) were obtained for aerosols due to smoke from a forest fire in Siberia. Smaller values of the exponent (ν = 2.5 to 3.0) were obtained for clear conditions in an unstable convecting atmosphere.

17. KEY WORDS AND DOCUMENT ANALYSIS

a. DESCRIPTORS	b. IDENTIFIERS/OPEN ENDED TERMS	c. COSATI Field/Group
Sky Brigthness Particle size distribution	Relation between sky brightness and atmospheric aerosol distributions	

Reproduced by
NATIONAL TECHNICAL INFORMATION SERVICE
US Department of Commerce
Springfield, VA. 22151

18. DISTRIBUTION STATEMENT: Release Unlimited	19. SECURITY CLASS (This Report): Unclassified	21. NO. OF PAGES: 115
	20. SECURITY CLASS (This page): Unclassified	22. PRICE: 5.25/2.25

PRICES SUBJECT TO CHANGE

EPA-650/4-75-012

RELATIONSHIP BETWEEN CIRCUMSOLAR SKY BRIGHTNESS AND ATMOSPHERIC AEROSOLS

by

Glenn F. Shaw and Charles S. Deehr

University of Alaska
Fairbanks, Alaska 99701

Grant No. 801113
ROAP No. 26AAS
Program Element No. 1AA009

EPA Project Officer: Edwin Flowers

Meteorology Laboratory
National Environmental Research Center
Research Triangle Park, North Carolina 27711

Prepared for

U. S. ENVIRONMENTAL PROTECTION AGENCY
OFFICE OF RESEARCH AND DEVELOPMENT
WASHINGTON, D. C. 20460

June 1974

ia

EPA REVIEW NOTICE

This report has been reviewed by the National Environmental Research Center - Research Triangle Park, Office of Research and Development, EPA, and approved for publication. Approval does not signify that the contents necessarily reflect the views and policies of the Environmental Protection Agency, nor does mention of trade names or commercial products constitute endorsement or recommendation for use.

RESEARCH REPORTING SERIES

Research reports of the Office of Research and Development, U.S. Environmental Protection Agency, have been grouped into series. These broad categories were established to facilitate further development and application of environmental technology. Elimination of traditional grouping was consciously planned to foster technology transfer and maximum interface in related fields. These series are:

1. ENVIRONMENTAL HEALTH EFFECTS RESEARCH
2. ENVIRONMENTAL PROTECTION TECHNOLOGY
3. ECOLOGICAL RESEARCH
4. ENVIRONMENTAL MONITORING
5. SOCIOECONOMIC ENVIRONMENTAL STUDIES
6. SCIENTIFIC AND TECHNICAL ASSESSMENT REPORTS
9. MISCELLANEOUS

This report has been assigned to the ENVIRONMENTAL MONITORING series. This series describes research conducted to develop new or improved methods and instrumentation for the identification and quantification of environmental pollutants at the lowest conceivably significant concentrations. It also includes studies to determine the ambient concentrations of pollutants in the environment and/or the variance of pollutants as a function of time or meteorological factors.

This document is available to the public for sale through the National Technical Information Service, Springfield, Virginia 22161.

Publication No. EPA-650/4-75-012

ABSTRACT

The color distribution and brightness gradient of diffuse skylight within an angular distance of roughly thirty to forty degrees from the sun depends critically on the composition, size distribution, and concentration of aerosols in the atmosphere. This circumsolar brightness is added to the skylight which results from scattered sunlight in a pure Rayleigh atmosphere. It is called the solar "aureole" and its magnitude and spatial distribution is dependent on the physical characteristics of aerosols in the free atmosphere. In an attempt to relate these characteristics to the observation, a description of the sky radiation in a turbid atmosphere was developed using the theory of radiative transfer and a perturbation method which treats the aureole sky intensity as a perturbation on an equivalent Rayleigh scattering mechanism where all orders of scattering are considered.

In order to make accurate measurements of the diffuse sky intensity within several degrees of the sun, it was necessary to develop a specialized instrument (sky coronameter), similar in nature to a solar coronagraph, to reduce instrumentally-scattered light from the bright solar disk immediately outside of the field-of-view. A well-baffled photometer for sky radiation measurements outside 10° from the sun was also designed and built, along with a precision direct sun photometer, used for making complementary multi-wavelength atmospheric transmission measurements.

Examples of sky intensity in the solar vertical plane and in the solar almucantar (an azimuth sweep through the sun at constant elevation angle) are presented from an arctic location near Barrow, Alaska (71°19'N, 156°37'W), a sub-arctic location at Ester Dome, Alaska (64°53'N,

148°03'W), and a tropical station at Loiyengalani, Kenya (2°45'N, 36°42'E). Estimates of the aerosol scattering phase function, $P(\theta)$, were derived from the observations which include a variety of synoptic conditions and different air-mass types. The aerosol scattering phase functions are then compared to a library of pre-calculated phase function curves made for various assumed forms of aerosol size distribution functions. In addition, numerical estimates were made of the columnar aerosol mass loading, γ (the total weight of aerosols contained in a vertical column with unit cross-section) based on the best fit aerosol size distribution and the quasi-monochromatic optical depth. Typical of continental observations, it was found that a Junge power-law aerosol size distribution function approximates the observed scattering phase function rather well. More complex distribution functions cannot be inferred legitimately from the measurements because of cumulative errors in the process of calculating the scattering phase function from the sky-brightness observations.

The Junge power-law exponent, ν, seems to depend upon air mass type, and to a lesser extent on local climatological conditions (ground cover, etc.). Relatively large values of ν (i.e., ν=4) were found during an episode of advected forest fire smoke from Siberia into Alaska. Smaller values (ν=2.5 to 3.0) were found during clear conditions in an unstable, convecting atmosphere.

Table of Contents

	Page
FIGURE CAPTIONS	vii
TABLE CAPTIONS	x
ACKNOWLEDGEMENTS	xi
CONCLUSIONS	xii
RECOMMENDATIONS	xiv
INTRODUCTION	1
General	1
The relation between aerosols and global climate	2
The brightness or intensity of the day sky	4
THEORY OF RADIATIVE TRANSFER IN A TURBID ATMOSPHERE	9
General remarks and theory	9
Primary scattering atmosphere	12
THE EFFECT OF AEROSOLS TREATED AS A PERTURBATION ON THE RAYLEIGH SCATTERING MECHANISM	17
First order aureole for an atmosphere containing non-absorbing aerosols	19
INSTRUMENTATION	21
Direct sun photometer	21
Calibration of sun photometer	24
Photoelectric coronameter	28
Calibration of photoelectric coronameter	34
RESULTS AND DISCUSSION	37
Overview	37
Measurements on April 11, 1973	38
Measurements on May 1973, at Interior Alaska	38
Measurements during forest fire episode, July 1973	41
Aerosol optical depths inferred from sky intensity	50
African measurements	53
Measurements on August 20, 1973	56
Measurements on August 2, 1973	63
The effect of cirrus clouds on sky brightness	66
Measurements on September 3, 1973	68

	Page
Aerosol mass loading	68
Measurements in Arctic Alaska, March 25-31, 1974	72
Measurements on May 2, 1974	81
THE RELATION BETWEEN THE JUNGE POWER-LAW EXPONENT AND THE AUREOLE BRIGHTNESS GRADIENT	85
REFERENCES	89
APPENDIX A	91
Units of sky brightness	91
APPENDIX B	97
Computation of geometrical parameters	97
A) The solar zenith angle	97
B) The air mass, m(z)	98
C) Scattering angle, θ	99
D) Effects of altitude, h	100

FIGURE CAPTIONS

		Page
Figure 1a	Polar plot of sky intensity for a molecular atmosphere. Intensity is expressed in units of solar flux divided by π.	5
Figure 1b	Sky intensity in the solar vertical plane for a molecular atmosphere with three values of surface albedo, A.	6
Figure 2	Polar plot of sky intensity as observed at Collge, Alaska on April 26, 1974 at 500nm. Sky radiance $=\pi I/Fo$.	7
Figure 3	Geometry relevant to solution of the radiative transfer problem for a plane, parallel atmosphere.	10
Figure 4a	Sky intensity in the solar vertical plane computed by single-scatter approximation (dotted) and by complete solution to the equation of transfer (solid). Sky intensity = $\pi I/Fo$.	15
Figure 4b	Same as above except computed for the solar almucantar. Sky intensity = $\pi I/Fo$.	15
Figure 5	Photograph of the direct-sun photometer.	22
Figure 6	Schematic of electronics for direct-sun photometer.	23
Figure 7	Setup for optical calibration of sky brightness photometer.	26
Figure 8	Optical diagram of the sky-brightness photoelectric coronameter.	29
Figure 9	Fieldstop in photoelectric coronameter.	31
Figure 10	Optical housing of photoelectric coronameter.	33
Figure 11a	Sky intensity on April 11, 1973 at College, Alaska at 500nm. Normalized to 1.0 intensity unit at the zenith.	39
Figure 11b	Sky polarization ratio in solar vertical plane.	39
Figure 12	Sky intensity in the solar almucantar at 500nm and 700nm normalized to 1.0 intensity unit at $\phi = 5°$.	40
Figure 13a	Sky intensity in the solar almucantar on July 25, 1973 at λ = 500nm, College, Alaska.	42
Figure 13b	Same as above, except at λ = 700nm.	43
Figure 13c	Sky intensity in the solar vertical plane on July 25, 1973 at λ = 500nm.	44
Figure 13d	Same as above, except at λ = 700nm.	45

		Page
Figure 14	Aerosol scattering phase function, $P(\theta)$, for July 25, 1973. Curves computed for power-law distribution are shown as light lines for different values of power-law exponent.	49
Figure 15	Scattering phase function, $P(\theta)$, computed for different aerosol size distribution functions.	51
Figure 16a	Rayleigh sky intensity, $\pi I/Fo$, in the solar almucantar at an angular distance of 50° from the sun plotted against optical depth τ for three values of surface albedo, A.	52
Figure 16b	Same as above except for four values of μ_o.	52
Figure 17a	Sky intensity, $\pi I/Fo$, in the solar vertical at Loiyengalani, λ = 500nm.	57
Figure 17b	Same as above, except λ = 700nm.	58
Figure 17c	Sky intensity, $\pi I/Fo$, in the solar almucantar at Loiyengalani, λ = 500nm.	59
Figure 18	Aerosol scattering phase functions deduced from sky brightness measurements.	60
Figure 19a	Sky intensity in the solar almucantar on August 20, 1973, λ = 700nm.	61
Figure 19b	Sky brightness in the solar vertical plane on August 20, 1973, λ = 500nm.	62
Figure 20a	Sky intensity in the solar vertical plane on August 2, 1973, λ = 500nm.	64
Figure 20b	Same as 20a, except for λ = 700nm.	65
Figure 21	Temporal variation of sky intensity centered on an evaporating jet contrail.	67
Figure 22	Sky intensity $\pi I/Fo$, on September 3, 1973, in the solar almucantar from Ester Dome, Alaska (solid) and from College (dashed).	69
Figure 23	Volume extinction coefficient calculated for Junge power-law distribution for constant aerosol mass loading of 50 $\mu g/m^3$.	71
Figure 24	Aerosol optical depth versus wavelength for 3 days in March 1974, Barrow, Alaska.	74

Page

Figure 25 Volume extinction coefficient versus wavelength calculated for Junge size distribution function and constant volumetric mass loading for various combinations of lower, r_1, and upper, r_2, cutoff radii. 76

Figure 26 Temporal variation of coronameter output voltage, Barrow, Alaska. 77

Figure 27 Diurnal variation of circumsolar sky intensity at angular distances of 1.2^0 and 6.2^0 from the sun's limb on March 26, 1974 at Barrow, Alaska. 79

Figure 28 Sky intensity, $\pi I/Fo$, in the solar almucantar on May 2, 1974, λ = 500nm, College, Alaska. 82

Figure 29 Langley plot of direct-sun data on May 2, 1974 at College, Alaska. 83

Figure 30 Wavelength dependency of aerosol optical depth on May 2, 1974 at College, Alaska. 84

Figure 31 Ratio of sky intensity at 1.2^0 and 6.2^0 as a function of the Junge power-law exponent, ν. 87

TABLE CAPTIONS

		Page
Table 1	Photoelectric coronameter specifications.	32
Table 2	Values of surface albedo measured at College, Alaska.	47
Table 3	Values of aerosol optical depth at Loiyengalani, Kenya, at 500 nm and 700nm.	54
Table 4	Values of columnar aerosol mass loading.	70
Table AC-1	Radiant intensities of some natural sources at λ = 550nm.	A5

ACKNOWLEDGMENTS

We wish to thank Drs. Edwin Flowers and George Griffing for helpful suggestions. We also appreciate the interest shown in our work by Mr. Richard Latimer.

Dr. Donald Pack and his associates helped arrange facilities for our use at Barrow.

Our thanks go to Mrs. Kathy Blagrove and Vicki Wade for typing the manuscript.

Partial support was provided for this study under NSF contracts GA-36871 and GU-40427 and by State of Alaska funds. The major support was provided by EPA grant number R801113.

CONCLUSIONS

Measurement of the brightness gradient and absolute intensity of scattered sky radiation in the circumsolar region within about thirty degrees from the sun provides a practical and useful method for assessing certain physical properties of atmospheric aerosols. For example, the columnar mass loading and an estimation of the size distribution function for the atmospheric aerosols can be obtained from the sky-brightness data.

The general method of analysis is most accurate, and hence most useful for atmospheres with low turbidity. Thus, the technique is especially useful for aerosol studies at locations far removed from urban pollution effects. In this regard, experiments done in interior Alaska and arctic Alaska using quasi-monochromatic sky radiation measurements obtained with specialized instrumentation, demonstrate that the aerosol size distribution and concentration sometimes fluctuates on time scales as short as hours.

There seems to be a complex relationship between the aerosol size distribution function and air mass type. Generally it is observed that polar air masses have lower columnar concentrations and a relatively larger ratio of small to large particles within the particle size spectrum. Forest fire smoke advected into interior Alaska from Eastern Siberia had a size spectrum which could be approximated by a Junge power-law distribution with an exponent value, ν, numerically equal to 4.0 ± 0.2. Aerosols generated by local convection have been observed to have power-law exponent equal to 2.5 ± 0.3.

The measurements of circumsolar sky intensity yield useful estimation of aerosol parameters even for extremely transparent atmospheres. We believe that the technique has application in connection with studies that involve the transport and origin of atmospheric aerosols.

RECOMMENDATIONS

The aureole method of studying aerosol size distribution and mass loading yields useful quantitative information in pure low turbidity atmospheres. As such, the technique has the potential for monitoring and studying aerosols at locations far from urban centers where air purity is high. Studies of the properties of the background aerosols are fundamentally important. For example, there has been much speculation recently by scientists that the background aerosol loading may be increasing globally due to the industrial activities of man. If in fact this hypothesis is correct, it eventually may have an impact on global climate because the aerosols effectively alter the radiation budget of the earth-atmosphere system. Considerations such as these make the problem of monitoring and quantifying the global distribution and temporal variations of the background aerosol a fundamental one in atmospheric science.

We strongly recommend that a network of stations be established at existing high-altitude mountain observatories and at some high latitude stations to monitor the solar aureole and establish important baseline information on the concentration and size distribution of the background aerosols. In view of the increasing worldwide industrialization, we feel that it is imperative to implement these programs as rapidly as possible.

INTRODUCTION

General

The free atmosphere is charged with small particulates (atmospheric aerosols) which are of the same order of size as the wavelength of visible light and which, as a result, interact strongly with the solar radiation field. Because of this strong optical interaction, the color, intensity and polarization of the day sky are modified by the presence of these suspended particulates. Optical effects are particularly strong at small angular distances from the sun because the aerosols diffract relatively large amount of radiant energy in the forward, or near forward direction, and relatively lesser amounts into the backward or side directions. As a result, a whitish glow or aureole, which can be attributed to the aerosols, is often observed to surround the sun.

For the reasons just stated, the circumsolar aureole is a sensitive indicator of the presence of atmospheric particulate material, and in fact exceedingly minute quantities of dust, such as might be found in pure non-urban atmospheres, can cause a detectable solar aureole to occur (Eiden, 1968; Green, Deepak, Lipofsky, 1971). Moreover, the optical characteristics of the aureole, such as the distribution of absolute intensity as a function of scattering angle or wavelength, are related to the physical properties of the aerosols themselves. This implies that it should be possible to obtain numerical estimates of the particulate size distribution and columnar mass concentration from measurements of the absolute diffuse intensity and its gradient near the sun.

As it happens, the analysis methods used to relate measurements of sky aureole intensity to aerosol parameters are most accurate when

applied to atmospheres of low turbidity. This means that photometric measurements of the solar aureole may be used to study the properties of aerosols in atmospheres of small optical depths where the aerosol content is hardly even detectable by other methods. Thus, the aureole method has the advantage that one may deduce the characteristics of the aerosols directly without disturbing or altering them in any manner. In addition, the method relates to total aerosol content in the atmosphere, integrated over height, and the properties are less affected by local surface conditions and more representative of the background conditions. The inherent disadvantages of direct sampling methods are thus avoided.

The Relation Between Aerosols and Global Climate

One of the reasons for studying the background aerosols is related to their important role in the regulation of global climate. Rasool and Schneider (1971), for instance, estimated that if the average global aerosol optical depth were to increase, a net cooling of the earth's surface would result which could, if the aerosol loading were sufficiently large, trigger an ice age. It has since been pointed out by several investigators (Mitchell, 1971, for example) that the effect of aerosols on climate is complex, and in fact a net heating or cooling may result depending upon the particle composition and size distribution, as well as other physical parameters such as the particulate height distribution and optical and thermal properties of the underlying surface.

It is a disturbing fact that rising industrialization around the world may eventually generate enough particulates to affect the climate. A case in point is the possibility of climate change brought about by

a stratospheric layer which might be created by large fleets of supersonic transport aircraft flying in the stratosphere. Although the optical depths involved in such a layer are likely to be small, the material is distributed globally because of stratospheric winds and diffusion processes. Hence the effects would be widespread, and may alter the radiation matrix at places as remote as the polar regions which are thought to be particularly sensitive to changes in radiation climatology (Fletcher, 1965). It is therefore all the more important to establish a baseline of global aerosol distribution as rapidly as possible.

Photometry of the solar aureole allows one to determine two parameters that are relevant to possible climate changes caused by aerosols: the aerosol size distribution, and the aerosol columnar mass loading.

The Brightness or Intensity of the Day Sky

If the atmosphere were free of aerosols, the sky intensity would be nearly constant with angle near the sun, and no major brightness gradient would be associated with the location of the solar disk itself. In other words, if one were to blot out the sun with an occulting disk and inspect the diffuse sunlight around the disk, one would find, in the case of an absolutely pure atmosphere, a smoothly varying gradation in sky intensity. The sky near the sun would be deep blue and relatively homogeneous (Figure 1). However, observations of the diffuse sky intensity have never documented such homogeneous sky conditions up to within a degree or so of the solar disk. Instead, it is more usual to find a strong whitish glow of light around the sun with a steep brightness gradient typically falling off rapidly with increasing angular distance from the sun (Herman et al., 1971) (Figure 2), but sometimes having more complex structure with hints of ring phenomena. Occasionally, the aureole has colors associated with it, although the hues are generally poorly saturated and subtle. The angular dimension of the aureole varies from place to place, and at any given location there are temporal variations, with significant changes in form and intensity sometimes occurring in time periods of less than one hour.

Generally speaking, the solar aureole is difficult to view with the unaided eye, partly because of its inherent brightness; but more importantly because of the overwhelming brightness of the direct sun. With some experience, however, one can learn to observe the aureole by blocking out the sun with a distant tree or pole, for instance, and inspecting the region around the sun through a neutral density filter with a transmissivity of about 10 percent. Using this technique, and

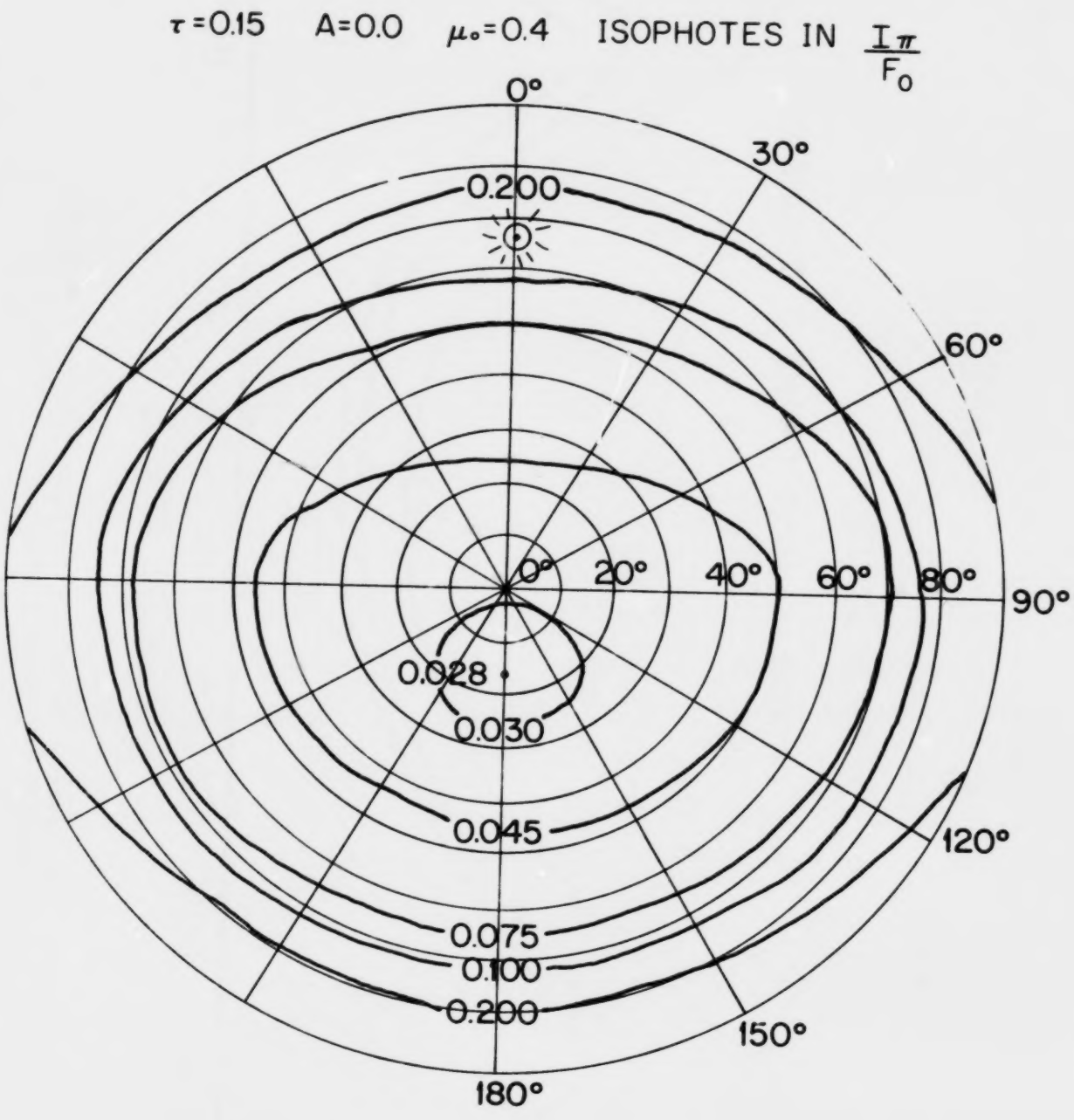

Figure 1a Polar plot of sky intensity for a molecular atmosphere. Intensity is expressed in units of solar flux divided by π.

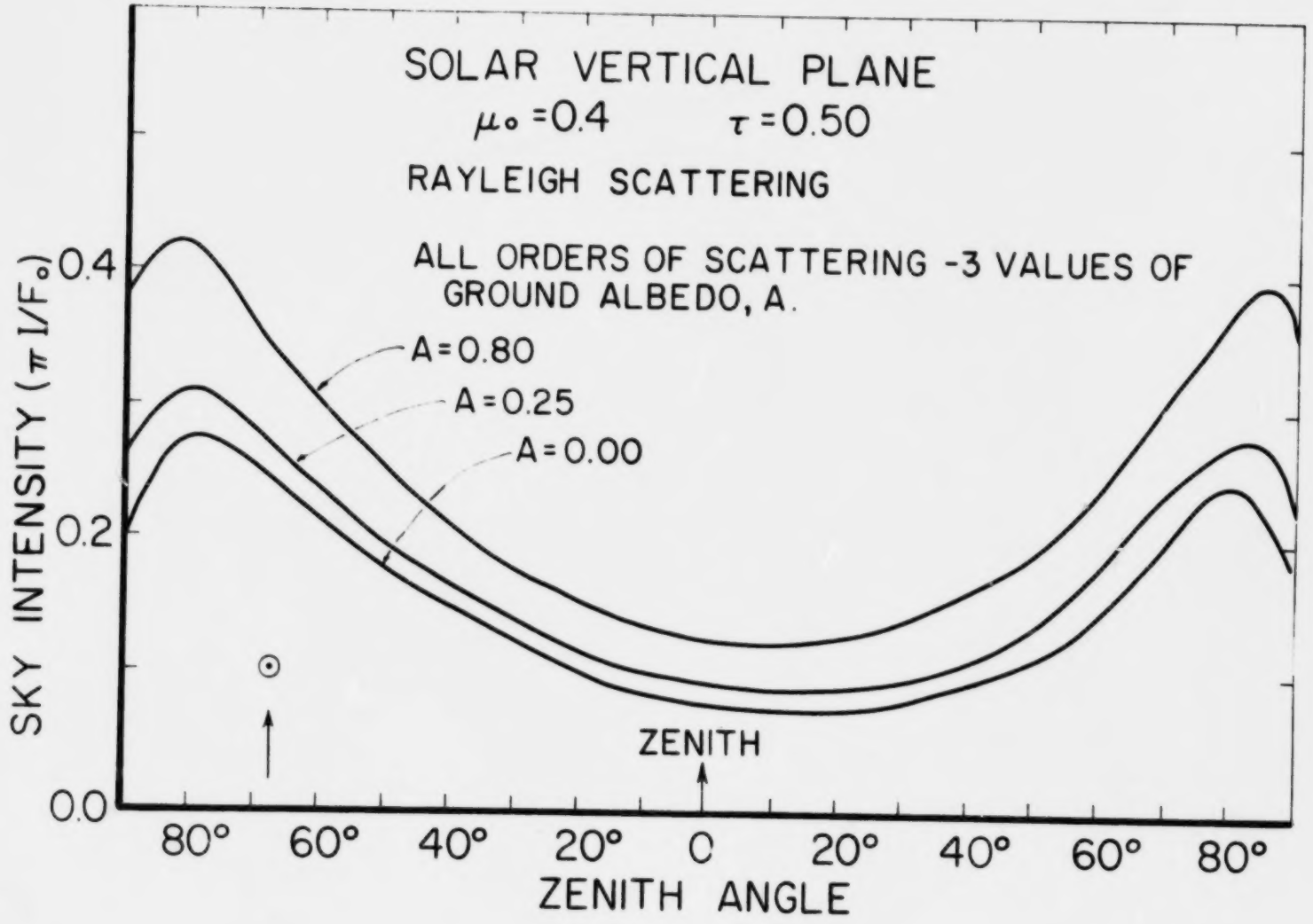

Figure 1b Sky intensity in the solar vertical plane for a molecular atmosphere with three values of surface albedo, A.

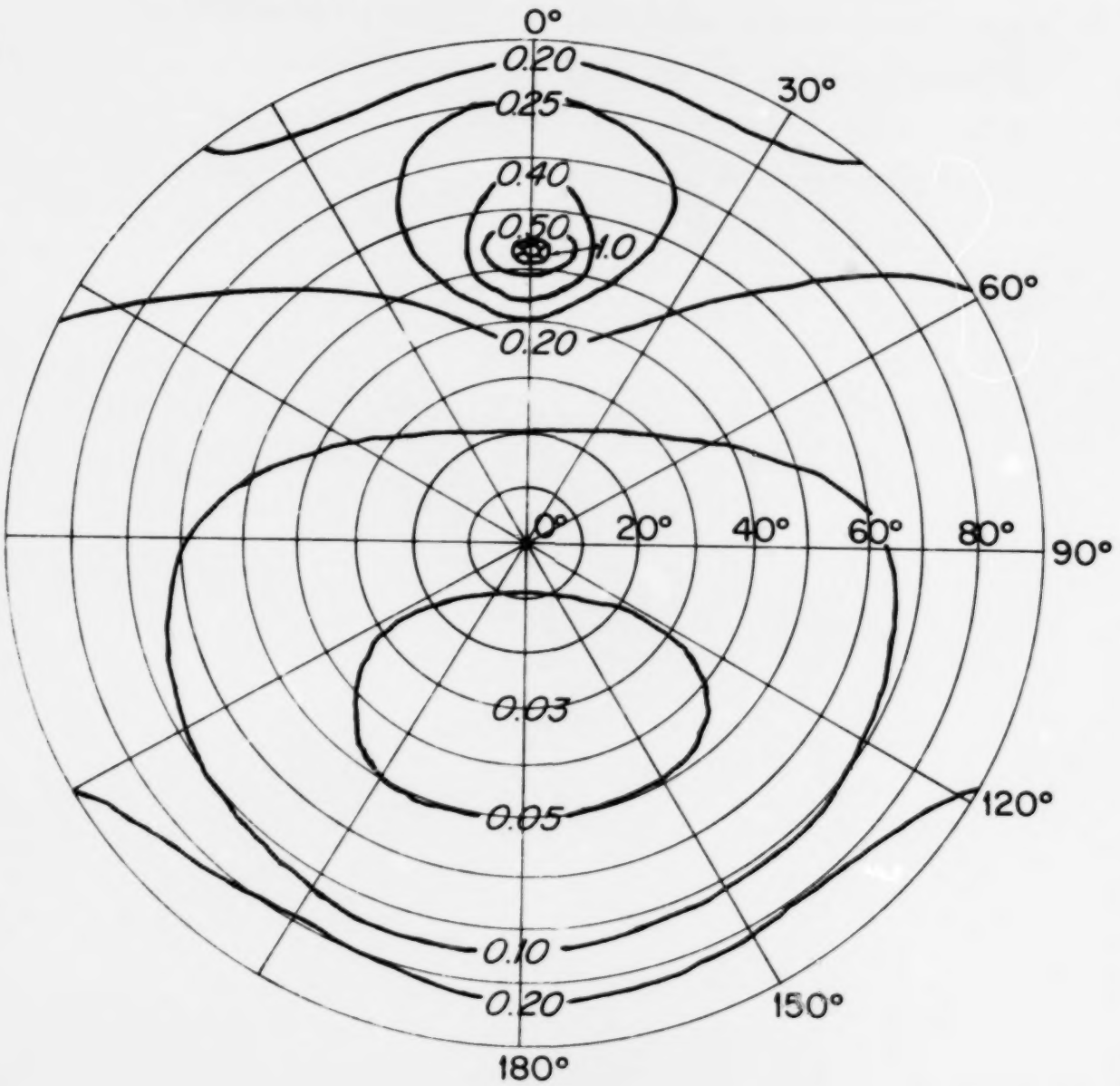

Figure 2 Polar plot of sky intensity as observed at Collge, Alaska on April 26, 1974 at 500nm. Sky radiance $=\pi I/Fo$.

making careful observations during clear periods, the aureole can be seen to vary from time to time and and can be placed into one of several classifications based on color, size and brightness. Such observations are highly subjective, however, and it is a distinct necessity to develop and use instrumentation particularly adapted to the problems and purposes of solar aureole measurements.

THEORY OF RADIATIVE TRANSFER IN A TURBID ATMOSPHERE

General Remarks on the Theory

In order to discuss the observational results which will be presented, we must first develop some theoretical background. In particular, we wish to address ourselves to the problem of specifying the i^{th} Stokes component of radiation field, I, of scattered light in a turbid atmosphere, (e.g., an atmosphere containing particulate material illuminated from the top by parallel radiation). For the sake of simplicity, we shall assume that the atmosphere can be approximated as being plane-parallel and infinite in extent and horizontally homogeneous. This approximation is valid, provided that both the elevation angles of the source of radiant energy (the sun), and the direction of view in which one requires the radiation field to be specified, are larger than approximately ten degrees or so. The geometry of the situation is illustrated in Figure 3.

The i^{th} Stokes parameter of the radiation field, I_i, may be obtained by solving the equation of radiative transfer (Chandrasekhar, 1950) which, for a plane parallel atmosphere, can be written as,

$$\mu \frac{dI_i(\tau,\mu,\phi)}{d\tau} = - I_i(\tau,\mu,\phi) + \frac{\tilde{\omega}}{4\pi} \int_0^{\pi} \int_0^{2\pi} [P_i(z,\phi;z',\phi') I_i(\tau,z',\phi') \sin(z')] dz' d\phi'$$

$$+ \frac{\tilde{\omega}}{4\pi} P_i(z,\phi;z_o,\phi_o) F_o e^{-\tau/\mu_o} \qquad 1)$$

where $\mu = \cos z$, with z being the zenith angle of the direction of view at which the radiation field is to be specified (μ is positive for downward directed radiation); z_o is the direction of the incident solar radiation, ϕ is the corresponding azimuthal angle referred to the sun's azimuth, $\tilde{\omega}$

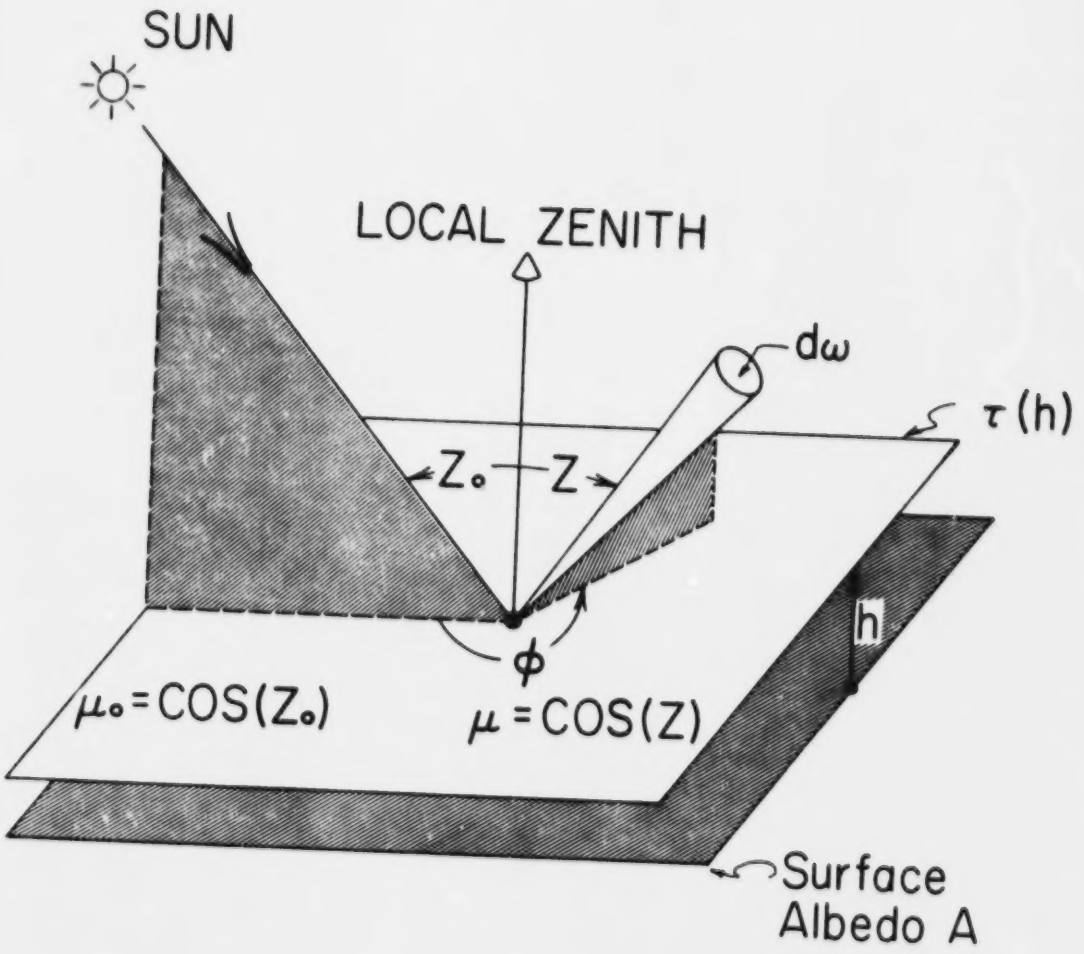

Figure 3 Geometry relevant to solution of the radiative transfer problem for a plane, parallel atmosphere.

represents the albedo for single scattering, F_o is the Stokes vector of the incident flux,and P_i is the normalized Stokes scattering matrix (van de Hulst, 1957) for the particular atmospheric scattering media.

The parameter, τ, is a quasi-monochromatic optical depth defined as

$$\tau(h) = \int_h^\infty [\beta_{abs}(h) + \beta_{sc}(h)]dh \qquad 2)$$

here β_{abs} and β_{sc} are the volume absorption coefficient and the volume scattering coefficients respectively, evaluated for a sample of the atmospheric media at height h.

The Stokes scattering matrix for a volume of the scattering medium, $P(\theta)$, is evaluated at scattering angle θ (see equation B7 in appendix B) and each element is normalized according to

$$\int_{4\pi} P_i(\theta)d\omega = 4\pi \qquad 3)$$

where $d\omega$ represents a differential solid angle, and the integration extends over 4π steradians.

The optical depth, τ, the albedo of single scattering, $\tilde{\omega}$, and the scattering phase function, P_i, depend upon the physical nature of the gases and particulate material contained in a representative volume sample of the atmosphere medium at height h. In practice, one evaluates these optical parameters separately for the molecular gas (the Rayleigh component) and for the particulates. The optical parameters for interaction of radiant energy on particulate material are generally evaluated by assuming that the particulates contained in a volume of air can be approximated by an ensemble of spherical particles distributed over a range of particle radii as specified by the particle size distribution function $\psi(r)$. The theory describing the electromagnetic scattering from an ensemble of spherical particles was first formulated by George

Mie in 1908. A brief description of Mie's scattering theory was given by van de Hulst (1957).

A turbid atmosphere is not homogeneous with respect to its scattering properties; that is, each element of the scattering matrix must be written in the weighted form (Deirmendjian, 1970),

$$P_i(\theta) = \frac{\beta_{SCR}\, P_R(\theta) + \beta_{SCM}\, P_M(\theta)}{\beta_{SCR} + \beta_{SCM}} \qquad 4)$$

where the subscripts SCR and SCM refer to scattering portions of the volume extinction coefficient for gaseous molecules (Rayleigh component) and for particulates (the Mie component). P_R and P_M are the "Rayleigh" and "Mie" scattering phase functions at height h in the atmosphere. In addition, for a volume of turbid air, Deirmendjian points out that the effective albedo for single scattering is given as,

$$\tilde{\omega} = \frac{\beta_{SCR} + \beta_{SCM}}{\beta_{SCR} + \beta_{ABSR} + \beta_{SCM} + \beta_{ABSM}} \qquad 5)$$

where β_{ABSR} and β_{ABSM} are the absorption components of the "Rayleigh" and "Mie" extinction coefficients respectively. The resultant albedo, $\tilde{\omega}$ is dependent on the type of scattering particle.

Primary-Scattering Atmosphere

It will be useful for our purposes to consider an approximate solution to the equation of transfer for a turbid atmosphere where only primary scattering is considered. This means, effectively, that we assume the integral term in Eq. 1) to be negligibly small. In addition, one assumes that $\tilde{\omega}$ and P are, to a first approximation, independent of height, and Eq. 1) may be integrated directly to obtain the first-order scattering term of the Stokes parameter, I_i, as,

$$I_i(\tau,\mu,\mu_o,\phi) = \frac{\tilde{\omega}}{4\pi} P_i(\theta) F_o \frac{\mu_o}{\mu_o - \mu} \left(e^{-\tau/\mu_o} - e^{-\tau/\mu}\right) \qquad 6)$$

Equation 6 neglects high-order scattering effects and we re-emphasize that it therefore represents only an approximate solution to the radiative transfer processes in the atmosphere. There are certain instances, however, where one may justifiably employ a single-scatter model to describe the diffuse radiation field. The accuracy of the model's predictions of the radiation environment increases as total optical depth diminishes, and in the limit $\tau \to 0$, the approximate single-scatter solution becomes exact. The accuracy to which Eq. 6) approximates a "true", or exact, solution also depends on the magnitude of the solar elevation angle, and less obviously, on the form of the scattering phase matrix. A practical example showing where one might utilize the single-scatter model to predict the diffuse radiation field can be found in areas requiring sky polarization and intensity prediction at aircraft or rocket altitudes where the optical depth remaining above the observer may approach small values (i.e., $\tau \lesssim 0.1$). Another example, and one that is more relevant to the problems at hand, involves the use of a single-scatter model in the interpretation of sky radiance in the red and near infrared regions of the electromagnetic spectrum, between gaseous absorption features, where optical depths are small (i.e., $\tau_R = 0.04$ at $\lambda = 1\mu$). In this regard, it is assumed of course that optical effects for aerosols can be ignored. In other words, the results would be expected to be valid only in the case of extremely pure atmospheres such as may be found over the polar regions, for instance. However, as will be demonstrated later, it is likely that such an assumption is rarely met in practice, and that in fact the optical effects arising from even

minute aerosol loading can be of great importance in the radiation environment. Nonetheless, from a pedagogical point of view, it may be of value to compare results of predictions of a single-scatter model (i.e., Eq. 6) with those obtained by exact solution of the equation of transfer including all orders of scattering. In this regard, techniques have been described by Chandrasekhar (1950) for solving the transfer equation exactly for a Rayleigh-scattering mechanism. Coulson, Dave and Sekera (1960) implemented Chandrasekhar's solution and compiled the results of the solution in tables for various numerical values of optical depth, τ, ground albedo, A, solar zenith angle, μ_0, observed zenith angle, z, and relative azimuth, ϕ.

Figure 4 shows a comparison of sky intensity as obtained by using the single-scatter approximation (Eq. 6), (dotted line) and as obtained from Coulson et al.'s tables. Curves are shown for a ground albedo, A, equal to 0.00. Parameters in Figure 4 are as follows: τ = 0.05, $\mu=\mu_0=0.4$. The curves in Figure 4 refer to the solar vertical plane. Note that the single-scatter approximation is reasonably close to the actual true radiation values as predicted by Coulson et al.'s tables, except for low elevation angles, near the horizon, where the results diverge.

One must remember that the single-scatter approximation to the solution of the equation of transfer is indeed only an approximation to the true radiation field, and high-order scattering can in fact make a significant contribution to the total radiation field. In general, the contribution of multiple scattered radiation becomes more important near the horizons,and relatively speaking, it also becomes more important as the optical depth increases above approximately 0.1.

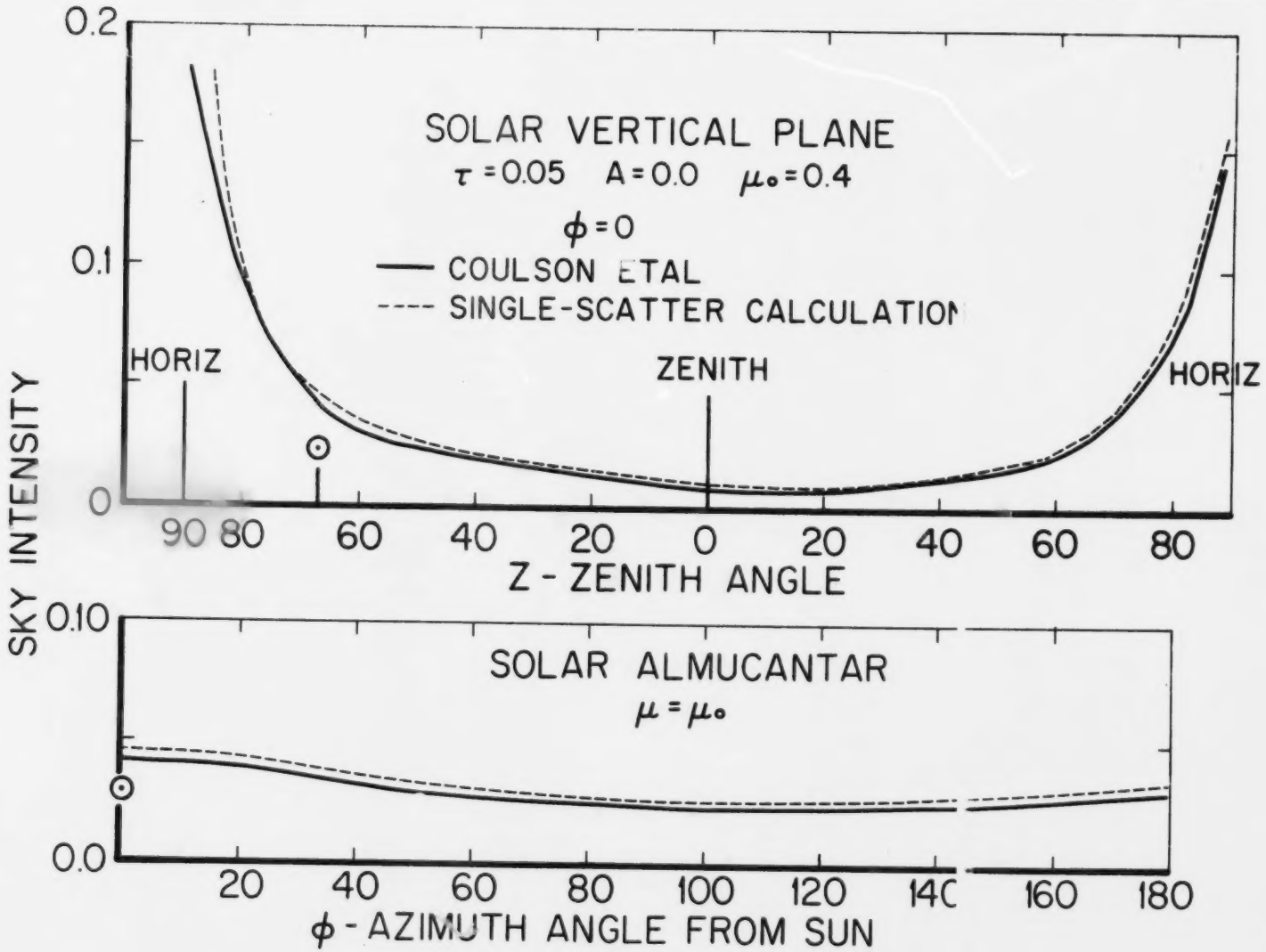

Figure 4a Sky intensity in the solar vertical plane computed by single-scatter approximation (dotted) and by complete solution to the equation of transfer (solid). Sky intensity = $\pi I/F_0$.

Figure 4b Same as above except computed for the solar almucantar. Sky intensity = $\pi I/F_0$.

In view of the fact that optical depths for realistic atmospheres in the mid-visible are of the order of τ=0.15, the effects of multiple scattering can not be neglected if high accuracy is wanted, and it is advisable to incorporate, by some method, the effects of multiple scattering in a model of the circumsolar radiation. This is done by considering the effect of the scattering by aerosols as a perturbation on an equivalent Rayleigh scattering mechanism which, as we have already pointed out, has been solved for all orders of scattering (Coulson et al., 1960). As we will see, this method of treating the effect of aerosols as a perturbation allows one to devise a useful and relatively simple method for use in quantitatively interpreting the circumsolar sky radiation.

THE EFFECT OF AEROSOLS TREATED AS A PERTURBATION ON THE RAYLEIGH SCATTERING MECHANISM

If one neglects high-order scattering, and considers primary scattering only, then one may solve two separate equations (one for aerosol scattering and one for molecular scattering), of a form similar to Eq. 1, but excluding the integral term. A solution is then obtained by adding the individual Rayleigh and Mie components. However, this technique would be rather unrealistic, because solutions to the equation of transfer exist, including all orders of scattering, for a Rayleigh scattering phase function. In view of this, a more reasonable approach is to incorporate the total Rayleigh solutions as tabulated by Coulson et al. (1960), and treat the effect of the aerosols as a perturbation on the Rayleigh scattering mechanism. To do this, we follow Deirmendjian (1970) who shows that the i^{th} component of the scattering matrix, $P_i(\theta)$, for a sample of turbid air, may be written in the form (essentially equation 4 in a different form),

$$P_i(\theta) = P_{iR}(\theta) + \frac{\beta_{SCM}}{\beta_{SCR} + \beta_{SCM}} (P_{iM}(\theta) - P_{iR}(\theta)) \qquad 7)$$

where, in the strictest sense, β_{SCR} and β_{SCM}, and therefore $P_i(\theta)$ are functions of height, h. Notice that the multiplier of the second term, the turbidity coefficient $\beta_{SCM}/(\beta_{SCR}+\beta_{SCM})$, vanishes when the aerosol loading becomes negligibly small, a desirable characteristic for a "perturbation" scheme.

When the scattering matrix (Eq. 7) is introduced into the equation of transfer (Eq. 1), the resultant equation can be expressed as the sum of two separate equations, written for the Rayleigh component, I_R, and the perturbation component, I_D. Each of these equations may, at least in principle, then be solved and the field can be obtained by simple

addition of terms. The tabulation of Coulson et al. (1960), for example, can be used, appropriately interpolated, to obtain the solution I_R.

The equation for the perturbation component, I_D, has been derived by Deirmendjian (1970), and the result is,

$$\mu \frac{dI_D(\tau,\mu,\mu_o,\phi)}{d\tau} = - I_D + \frac{f(\tau)}{4\pi} e^{-\tau/\mu_o} P_D(\theta)\cdot F_o \qquad 8)$$

$$+ \frac{f(\tau)}{4\pi} \int_{\Omega} [P_D(\theta) \cdot I_R(\tau,z',\phi') + I_D(\tau,z',\phi')]d\omega$$

$$+ \frac{1}{4\pi} \int_{\Omega} [P_R(\theta) \cdot I_D(\tau,z',\phi')]d\omega$$

where $f(\tau) = \beta_{SCM}/(\beta_{SCR} + \beta_{SCM})$, $P_D = P_M - P_R$, and θ is the scattering angle between the directions z', ϕ' and z, ϕ.

As Deirmendjian points out, Equation 8 is amenable to solution in various approximations, depending upon the particular aspect of the problem of interest. For instance, one can disregard the integral term which is equivalent to neglecting high-order scattering effects which arise from the aerosols. The resulting equation will yield a first-order approximation which accounts for primary scattering according to the virtual phase function $P_D = P_M - P_R$. In a clear atmosphere with low turbidity, this approximation should be most suitable for estimating the radiation field in the vicinity of the sun within angular distances up to approximately 40^o. Deirmendjian indicates that the effects of turbidity on the sky light at larger angular distances from the sun is such that the integral terms in Eq. 8) cannot be neglected anymore. One could, of course, utilize an iterative method and obtain a first-order approximation to the perturbation field, I_D, by the technique just

described, after which the solution could be substituted in the integral expression in Eq. 8) to obtain a second-order approximation, $I_D^{(2)}$. The procedure, which is somewhat tedious to carry out, could be continued in an iterative fashion until the trial solutions agreed with the calculated solution to within some pre-specified accuracy criteria. In any event, the total field representing the sky radiation in a turbid atmosphere, would then simply be,

$$I(\tau',z_o,z,\phi) = I_R(\tau',z_o,z,\phi) + I_D(\tau',z_o,z,\phi). \qquad 9)$$

It should be kept in mind that the optical depth τ' in the above equation refers to the total (aerosol plus Rayleigh) value.

First-Order Aureole for an Atmosphere Containing Nonabsorbing Aerosols

If, one neglects the high-order scattering terms in the equation for the perturbation stokes parameter, I_D, (i.e., the integral expressions in Eq. 8), then, the solution to the resulting ordinary inhomogeneous differential equation may be expressed as,

$$I_D^{(1)}(\tau';z_o,z) = \frac{(P_M - P_R)}{4\pi} F_o \sec(z)\, e^{-\tau'\sec(z)} \qquad 10)$$

$$\cdot \int_0^{\tau'} \frac{\beta_{SCM}(h)}{\beta_{SCR}(h) + \beta_{SCM}(h)} e^{-|\sec(z_o) - \sec(z)|\tau} d\tau.$$

In general, the integral expression in Eq. 10 must be evaluated by numerical methods. However, if the shape of the size distribution function and the composition of the aerosols is independent of height so that only the total number density varies, the evaluation of the integral term can be simplified considerably. For the sake of simplicity, we follow Deirmendjian's (1970) suggestion and consider an atmosphere

with homogeneous turbidity which means that we replace the actual vertical distribution by a virtual distribution with a constant mixing ratio of particle to molecules, so that the total numbers in a vertical column remain unchanged. In other words, we set,

$$\frac{\beta_{SCM}(h)}{\beta_{SCR}(h) + \beta_{SCM}(h)} = \frac{\tau'_M}{\tau'_R + \tau'_M} = \text{Constant} \qquad 11)$$

The substitution of Eq. 11 into Eq. 10 results in,

$$I_D^{(1)}(\tau', z_o, z) = \frac{(P_M - P_R)}{4\pi} F_o \frac{\sec(z)}{|\sec(z) - \sec(z_o)|} \left(\frac{\tau'_M}{\tau'_R + \tau'_M}\right) \cdot \left| e^{-\tau' \sec(z_o)} - e^{-\tau' \sec(z)} \right| . \qquad 12)$$

Notice that the Eq. 12) is identical in form to the solution of the equation of transfer for single scattering (Eq. 6), except that it is multiplied by a turbidity factor equal to $\tau_M/(\tau_M + \tau_R)$, and it employs a virtual phase function $(P_M - P_R)$.

Deirmendjian points out that the simple first-order solution (Eq. 12), should be used only when one is interested in a) the radiation field at the bottom of the atmosphere and b) values of z and z_o less than approximately 80^o so that the effects of the curvature of the atmosphere do not invalidate the initial assumption of a plane-parallel atmosphere.

INSTRUMENTATION

Direct Sun Photometer

In order to assess atmospheric aerosol parameters using sky intensity measurements one must know the optical depth of the atmosphere, $\tau_T(\lambda)$. This parameter was determined in this study by using a battery operated photometer which was constructed to measure the ground-level solar flux at narrow wavelength intervals; it is shown in Figure 5. The photometer uses interchangeable 25mm diameter interference filters to define wavelength intervals typically about 10nm wide. The optical head of the device consists of a 30mm diameter, 200mm focal length, objective lens, a field aperture and a solid state silicon photodetector. The field aperture is used to define a 3^0 diameter field of view. In use, the optical head is pointed at the sun with the aid of a small peep sight.

The electric current from the photodetector is amplified with a feedback-controlled operational amplifier circuit. The schematic diagram of the electronics is shown in Figure 6.

The feedback resistors are a carbon film type to minimize resistivity changes with temperature. The unit employs an FET input high impedence operational amplifier with an input bias current less than 1 pa.

The planar photodetector is operated in an unbiased photo voltaic mode with a temperature coefficient of about $0.1\%/^oC$. There are five ranges of sensitivity each differing by a factor of ten times from its adjacent position. On maximum sensitivity, full scale deflection is provided by a radiant flux (at λ = 500nm) of 2×10^{-5} $\mu w\ cm^{-2}nm^{-1}$ from a

Figure 5 Photograph of the direct-sun photometer.

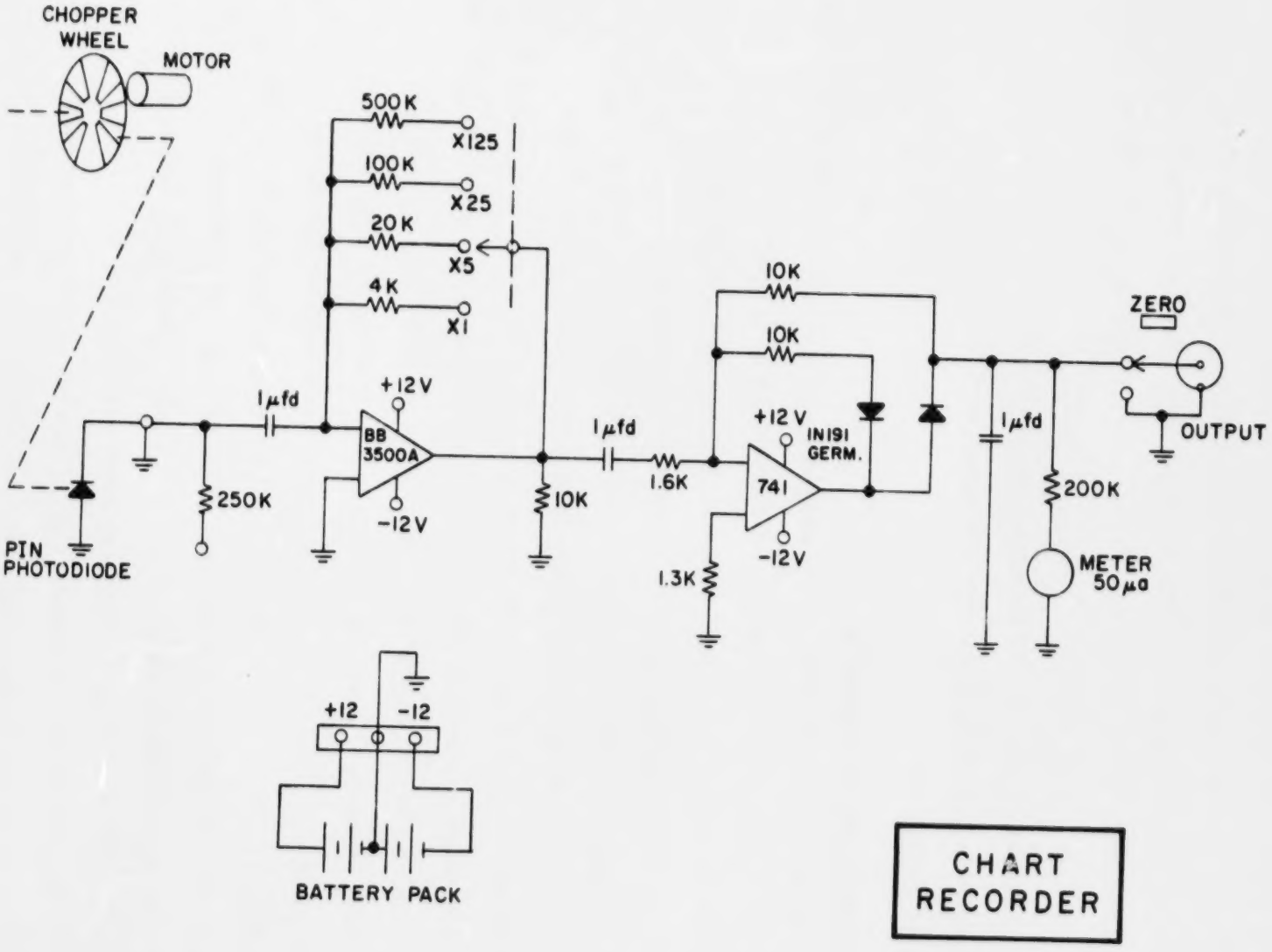

Figure 6 Schematic of electronics for direct-sun photometer.

point source. If the source is diffuse, a uniform intensity of 6.5×10^{-2} $\mu w\ cm^{-2} nm^{-1} sr^{-1}$ will give full scale reading on the most sensitive scale. Minimum detectable signal is roughly equal to 1% of the most sensitive scale which corresponds to a value of intensity (at λ = 500nm) of 6.5×10^{-4} $\mu w\ cm^{-2} nm^{-1}\ sr^{-1}$.

In order to use the instrument to measure direct solar radiation, we employ a reduced aperture with a diameter of 0.5mm to limit the incoming radiant energy.

Calibration of Sun Photometer

A 200 watt quartz iodine lamp powered by a regulated constant-current source (Stair, Schneider and Jackson, 1963) is used to calibrate the sun photometer. During the calibration, one must use extreme care to insure accurate results; we have heard many reports of standardized lamps suddenly changing irradiance. To insure against this eventuality, we intercalibrate among three separate standard lamps; this procedure increases the confidence of the calibration and it is highly recommended as a standard calibration procedure. It is also important to have a constant current supply because lamp radiance is especially sensitive to current variations. The lamp housing is also a matter of some importance; ideally it should consist of a dead black surface with no internal reflections and an adequate air supply to prolong lamp life. One must check against reflections from walls, ceilings and components within the calibration room. We use a room that is specially designed with extensive baffling to reduce spurious reflections.

The calibration for radiant flux is carried out by pointing the photometer at the standard lamp. Because radiant flux decreases ac-

cording to r^{-2}, one can, by varying the photometer-lamp distance, adjust the incoming flux over known relative ratios; this provides a method of checking photometer linearity. In this fashion we have experimentally determined that the sun photometer output voltage is linearly related to the input radiant flux to better than one percent over a range of four orders of magnitude of input radiance.

The photometer can also be used to measure diffuse radiation (intensity) but the calibration procedure is slightly different. For this case, one views a white Lambertian screen (Figure 7) that is directly illuminated by a point source of light (a 200 watt quartz iodine standard lamp).

Accuracy requirements of optical calibration are important. As an example, we consider the precision necessary for calibrating a sun photometer. If one assumes that a negligible amount of diffuse radiation enters the field of view of the photometer in comparison to the direct solar flux, then, for a linear instrument, one may write the Lambert-Beer extinction law in terms of photometer voltages as

$$V(\tau,\lambda) = V^{1}(\lambda)\, e^{-\tau(\lambda)\cdot\sec(z_o)} \qquad 13)$$

where $V(\tau,\lambda)$ represents the measured photometer voltage resulting from direct solar radiation attenuated by an atmosphere of optical depth $\tau(\lambda)$. The term $V^{1}(\lambda)$ is the estimated photometer voltage that would arise in the absence of an attenuating atmosphere. This term can be derived through a standard lamp calibration method provided one knows the value of the solar spectral radiance and the lamp spectral radiance at wavelength λ. The value of V^{1} can also be derived by extrapolating direct sun photometer measurements made at different values of solar zenith

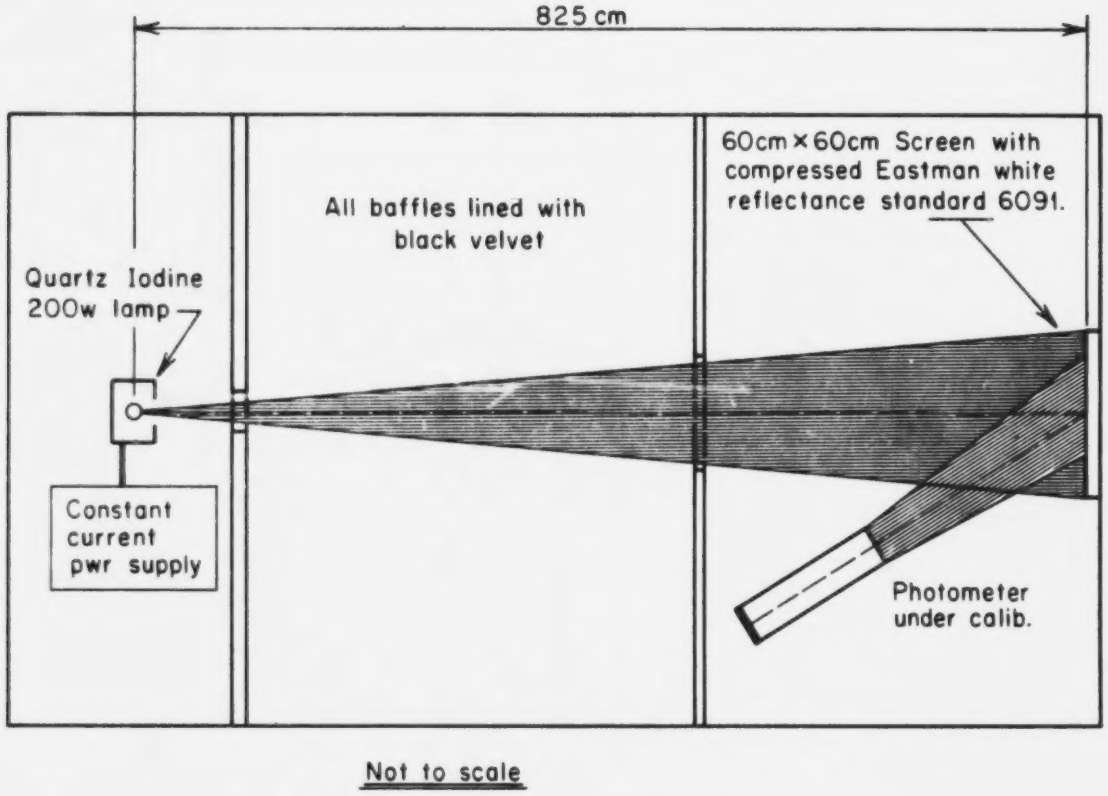
825 cm
60cm × 60cm Screen with compressed Eastman white reflectance standard 6091.
All baffles lined with black velvet
Quartz Iodine 200w lamp
Constant current pwr supply
Photometer under calib.
Not to scale

Figure 7 Setup for optical calibration of sky brightness photometer.

angle z, through the atmosphere; that is to say, a point where $\tau \cdot \sec(z)$ equals zero. Either way can be used, and in practice we have found that a combination of the two methods, using solar radiation measurements only for the clearest days, gives the most accurate results. Once V^1 is established, variations in V^1 caused by photometer aging can be assessed by monitoring, upon occasion, the standard lamps. In this way one can periodically update the so-called intercept voltage, V^1, to take account of long term drifts in photometer sensitivity.

In any event, the value of V^1, for a given photometer, is built up from the results of sun and standard lamp measurements, and any errors, caused by inaccuracies in τ or by temporal variations in τ during the times the direct sun measurements are being accumulated. Assuming that the photometer voltage, $V(\tau,\lambda)$ is measured with perfect accuracy, what then are the requirements on V^1, and thus calibration accuracy, if we want to know τ to some stated accuracy? This is easily assessed by differentiating equation 13 to give

$$0 = dV^1(\lambda)e^{-\tau/\mu_o} - V^1(\lambda)e^{-\tau/\mu_o} d\tau/\mu_o \qquad 14)$$

As a numerical example, if we wish to determine τ to an absolute accuracy of 0.010, for $\mu_o = 0.25$ ($z=75.6^o$) one will require that dV^1/V^1 be known to within 0.04. This accuracy is difficult to obtain by optical calibration methods, but it is certainly possible provided one makes every effort to assess and to minimize optical calibration errors.

Photoelectric Coronameter

It is difficult to make accurate measurements of sky radiation close to the sun because of problems with instrumental scattering and diffraction from the bright solar disk just outside the field-of-view of the instrument. In practice, one must utilize special techniques to reduce these instrumental effects when attempting to make photometric measurements closer than approximately five or ten degrees from the solar limb. Recall that these measurements close to the sun are in fact extremely important for our purposes because the sky brightness in this region is highly dependent on the aerosol content of the atmosphere. Because of this, we devoted considerable attention during this study to designing an instrument which could be used to measure sky intensity close to the sun's limb. The resultant instrument uses a photoelectric detector and in many respects is similar to a solar coronagraph (Eddy, 1961; Evans, 1948).

Figure 8 illustrates, in a schematic way, the construction of the photoelectric coronameter. The design is similar to a visual sky brightness photometer described by Evans (1948). Its operation may be explained as follows:

Light from the region of the sky surrounding the sun passes through aperture a_1. Filter f_1 defines a narrow wavelength interval for the observations. The direct radiation from the solar disk is blocked from entering aperture a_1 by the occulting disk O_1. In other words, the disk O_1 is made large enough so that no portion of the solar disk can be "seen" from any point in a_1. Lens L_1 forms an image of the sky around the sun at the field stop. Aperture a_2 and occulting disk O_2 define an annular field of view.

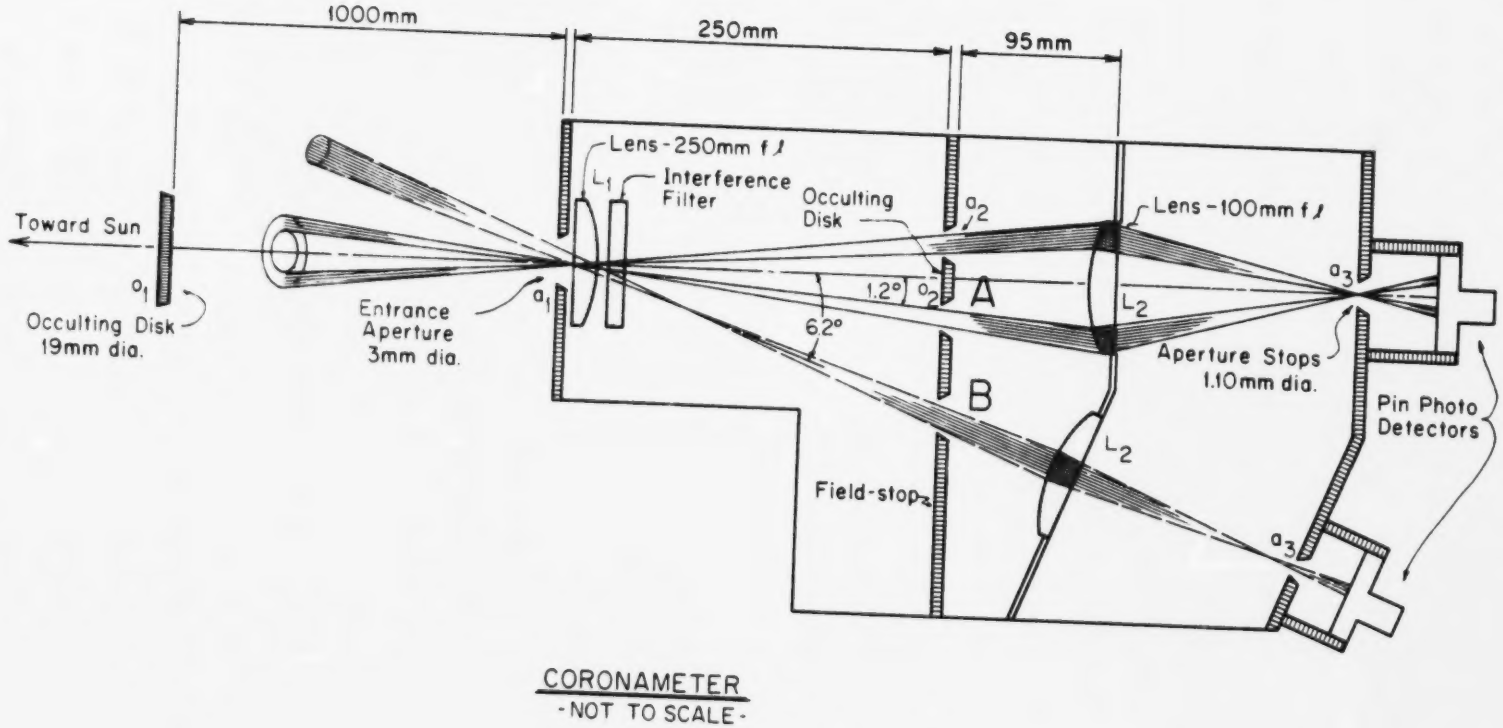

Figure 8 Optical diagram of the sky-brightness photoelectric coronameter.

Diffracted light from around O_1 is prevented from entering through the system by making occulting disk O_2 large enough to block the slightly out of focus image of O_1. Lens L_2 in conjunction with lens L_1 forms a low power (2.5X) telescope. When viewed through L_2, one sees an in-focus image of the backside of occulting disk O_2 surrounded by an image of the sky around the sun.

Although primary diffracted light emanating at the edge of occulting disk O_1 has been suppressed, there is yet another source of diffraction, namely the edges of the entrance aperture a_1. This source of diffraction is eliminated by placing aperture a_3, slightly smaller than the exit pupil of the telescope system, at the image of a_1 formed by lens L_2. The light rays passing through the aperture finally impinge on a PIN-doped silicon photodetector, PD, to generate an electric current which is amplified and registered on a panel meter or chart recorder.

The diameter of a_2 and O_2 in conjunction with the focal length of lens L_1 determine the inner and outer angular diameters of the annular field of view from which sky radiation is accepted. In the instrument designed for this study, we employed two optical systems designed to accept radiation from two regions of the sky corresponding to two different scattering angles. Figure 9 shows the details of the field stop that is located at the focal point of lens L_1. As already mentioned, the instrument has two optical paths; one accepts radiation from an annular region (A). The other channel accepts radiation from the partial annular region (B). The areas A and B are equal so that if there were no brightness gradient in the aureole, the radiant flux passing into the two apertures would be equal.

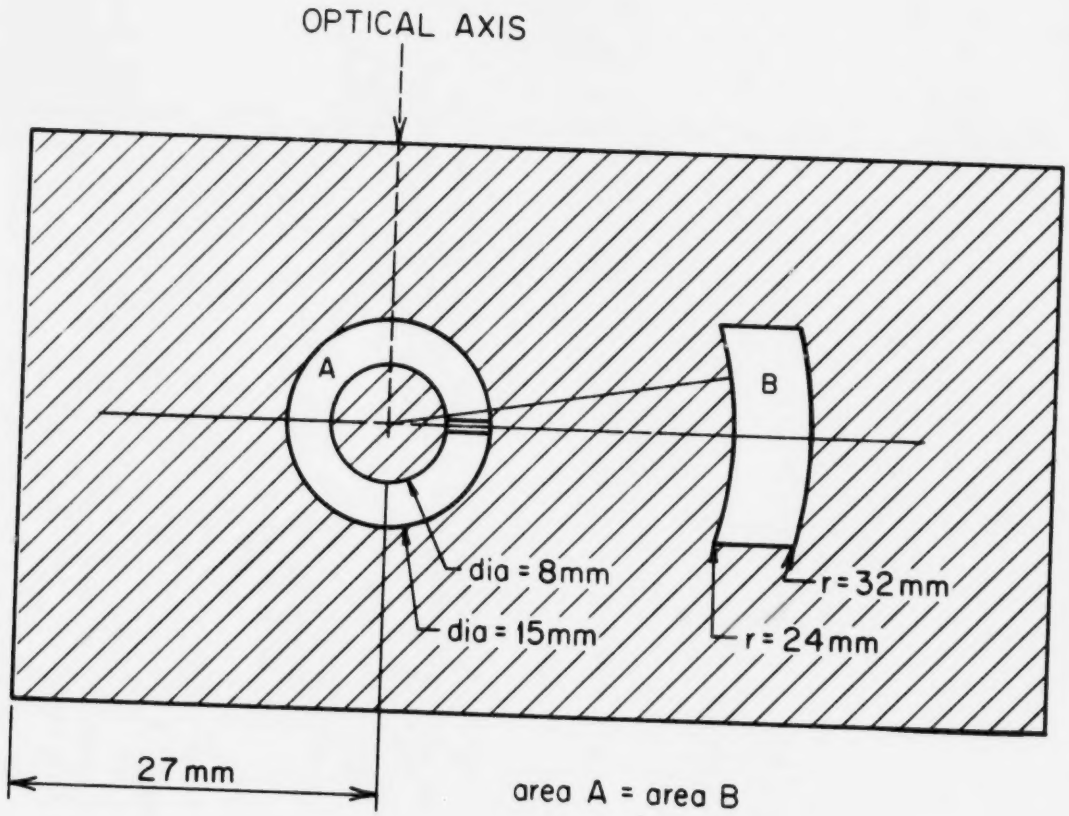

Figure 9 Fieldstop in photoelectric coronameter.

Behind the aperture A and B there are two cylindrical "eyepiece" assemblies each containing lens elements (L_2) and apertures a_3. The photodetector, PD, is in a removable mount which can be placed over each "eyepiece" assembly to obtain a measurement. Notice that the "eyepiece" assembly which receives light from aperture A_1 is on axis with a line drawn from the sun to the entrance aperture a_1. The "eyepiece" assembly that receives radiant flux through the optical path marked "B" in Figure 8, however, is canted off along a line drawn from L_1 through the mid-point of aperture B. It may be noted that when the photodetector unit, PD, is removed, one may directly view the solid angle of the sky from which radiation is being accepted. This is useful to insure that the optics are properly aligned and also to insure that nothing is blocking the field of view. Figure 10 shows the optical housing of the corona-meter.

In use, the instrument must be pointed accurately at the sun. This is done by centering the shadow of the occulting disk on the entrance aperture. The front portion of the instrument is supported on a camera tripod. The elevation angle is changed by cranking the center post of the tripod and azimuth angle is adjusted with a rack and pinion on the head of the tripod.

The coronameter is portable and easy to set up in the field. Total weight including tripod is about 10 kg.

Relevant instrument parameters are listed in Table 1.

Table 1

Photoelectric Coronameter Specifications

Diameter of primary occulting disk O_1	19mm
Diameter of entrance aperture a_1	3mm
Separation of O_1 and a_1	1000mm

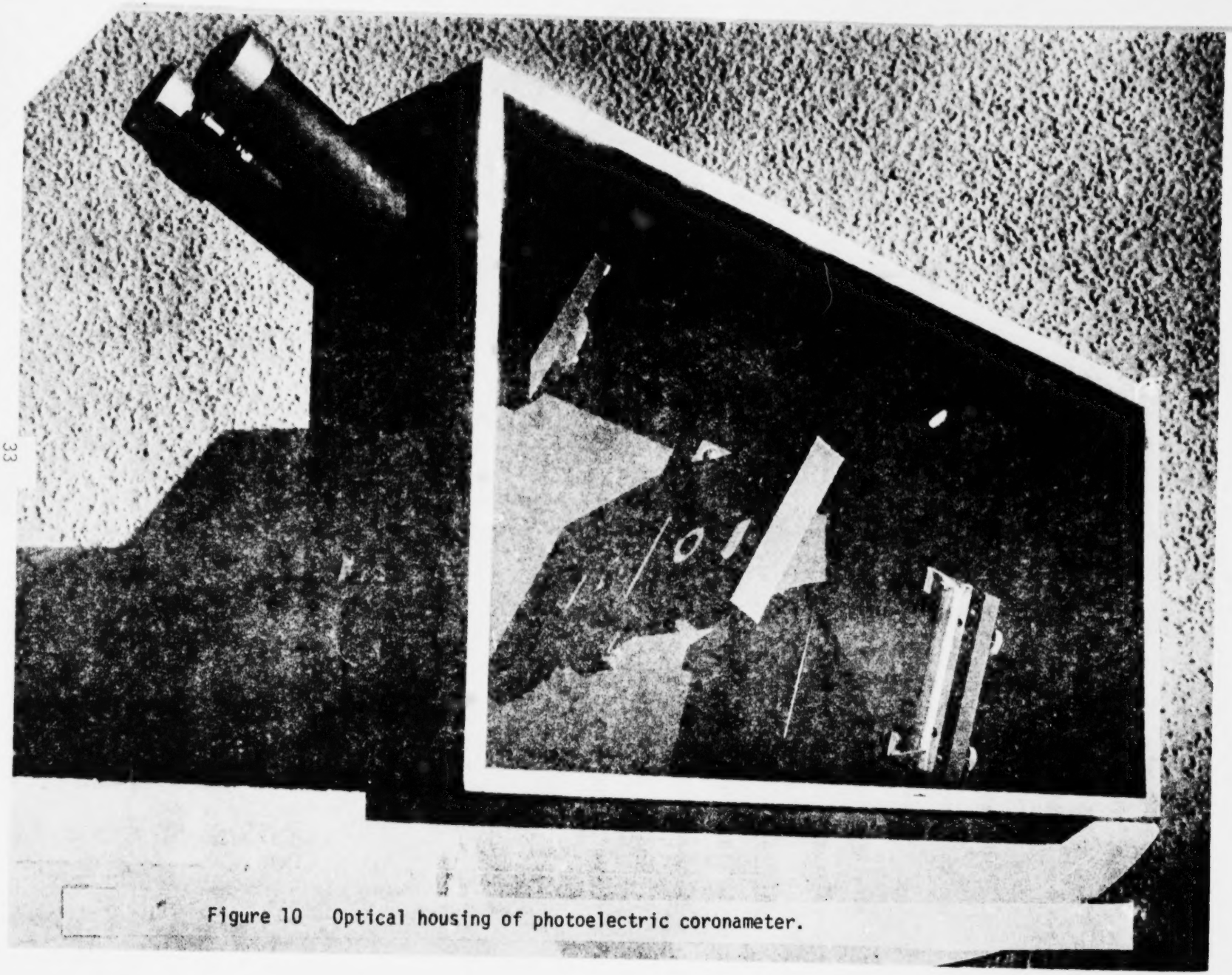

Figure 10 Optical housing of photoelectric coronameter.

Focal length of objective lens L_1	250mm
Focal length of field lens L_2	100mm
Diameter of exit aperture a_3	1.1mm
Photo detector	Silicon, PIN-doped
Mean Scattering Angle (Chan. 1)	1.1^o (from solar limb)
Mean Scattering Angle (Chan. 2)	6.2^o (from solar limb)

The two channel design allows one to evaluate quickly and easily the scattered sunlight at two different scattering angles from the solar limb. These two data points are supplemented with readings of sky intensity made with a sky photometer that is equipped with a well-baffled collimator and is used for scattering angles larger than ten degrees.

Calibration

The photoelectric coronameter is calibrated by pointing it at a diffuse Lambertian screen placed exactly perpendicular to the sun and illuminated by the direct solar radiation. The illumination of the screen by the direct sun and sky may be written as,

$$I_{S+D} = \frac{R_{SC}}{\pi} \cdot F_o \cdot T_{ATMOS} + \int_{\pi} I_{SKY} \cos(\theta_{12})\, d\omega \qquad 15)$$

where I_{S+D} = diffuse screen intensity ($\mu w\ cm^{-2} nm^{-1} sr^{-1}$) resulting from direct radiation, S, plus diffuse radiation, D

R_{SC} = Hemispherical screen reflectivity (0.99 at $\lambda = 0.5\mu$)

F_o = Incident solar flux ($\mu w\ cm^{-2} nm^{-1}$)

T_{ATMOS} = Slant path atmospheric transmission evaluated at mean observation wavelength

I_{SKY} = Diffuse incoming sky intensity

θ_{12} = Angle between solid angle cone, $d\omega$, and direction to sun.

The integration is carried out over the hemisphere above the screen.

This integral term represents the component of screen intensity due to the illumination of the screen by the diffuse sunlight and reflected ground radiance. In clear atmospheres it is typically about one tenth as large as the first (direct solar radiation) term.

In practice, the transmission of the atmosphere, T_{ATMOS}, is determined by measuring the direct incoming solar flux with the sun photometer, as described in the preceeding section.

The second term in Eq. 15 corresponding to the component of screen intensity due to illumination by diffuse light is accounted for experimentally by blocking out the direct component of solar flux and allowing the screen to be illuminated by diffuse radiation only. By measuring photometer current arising from the screen when illuminated by direct sun plus "diffuse" sky, I_{S+D}, and then subtracting the current which arises from the screen when it is shadowed from direct radiation, one may infer the photometer current which would arise from direct solar radiation alone, i.e.:

$$i_S = i_{S+D} - i_D \qquad 16)$$

which, in turn, allows one to derive an expression for the calibration constant of the instrument,

$$C = \frac{(i_{S+D} - i_D)\,\pi}{R_{SC} F_o T_{ATMOS}} = \text{amperes/intensity unit.} \qquad 17)$$

Typically, the calibration gives a day-to-day repeatability to better than about 5%. When the instrument is taken from a room temperature environment and used in very low temperatures ($T = -30^{o}C$), an insignificant shift in calibration of a few percent is found to occur, probably

due to slight changes in the optical alignment. We have used the instrument over a range of air temperatures $-35^{o}C < T < 40^{o}C$ with a total change in calibration of less than five percent.

RESULTS AND DISCUSSION

Overview

During the period extending from February, 1973 to the time of this writing (June 1974), we made numerous measurements of sky intensity and atmospheric transmission. Only a small sample of the data taken, however, are illustrated here. One reason for this is that only a few measurements are necessary to demonstrate the general technique used; another reason is that the quality of the data improved steadily as the instruments and methods of data acquisition were improved. Emphasis is therefore directed toward the more recently acquired data.

As we have mentioned previously, the perturbation method of analysis is most useful and should therefore have the greatest application for studies involving clear, homogeneous atmospheres. As a result, we have made the great majority of our measurements at times when air purity was high and when urban contamination was negligible. In other words, we directed our efforts towards assessing the "background" aerosol.

We have made measurements from the following locations: in Alaska, at Ester Dome, Alaska ($64^{o}53'N$, $148^{o}03'W$); from the roof of the C.T. Elvey building on the "west ridge" of the University of Alaska campus at Fairbanks ($64^{o}52'N$, $147^{o}51'W$), and from the NOAA Geophysical Monitoring Site at Barrow, Alaska ($71^{o}19'N$, $156^{o}37'W$). In addition, we have measured sky intensity at Tucson, Arizona at The Institute of Atmospheric Physics ($32^{o}14'N$, $110^{o}57'W$) and from an equatorial location at Loiyengalani, Kenya ($2^{o}45'N$, $36^{o}42'E$). Eventually, we hope to make sky intensity measurements at the NOAA background monitoring station at Mauna Loa to intercompare with existing radiation measurements that are being gathered there.

Measurements on April 11, 1973

The course of sky intensity and sky polarization is illustrated in Figure 11 for April 11, 1973 at Fairbanks. The curves correspond to sky intensity at a mean wavelength of 500nm in the solar vertical plane (solid) and the solar almucantar (dotted). The measurements were made with an early version of a sequence of several sky photometers. We learned, unfortunately after the measurements were taken, that this photometer in its early design had a calibration uncertainty and as a result, the ordinate values cannot be expressed reliably in absolute units, instead the ordinate scale is in relative units normalized to 1.0 at the zenith (Note that a logarithmic scale is used).

The conditions during the measurements of Figure 11 were as follows: the sky was clear of clouds and the snow cover was approximately 50%. A measure of the ground albedo gave A_{GND} = 28%. Horizontal visibility during the measurements was judged to be approximately 160 km (the Alaska Range at a distance of 144 km could be seen with medium contrast). The summit of Mt. McKinley (d = 240km) was not visible.

The curves displayed in Figure 11 show, qualitatively speaking, the features that one might expect for a relatively pure atmosphere. A polarization maximum occurs at a primary scattering angle of approximately 90^{o}. A minimum in intensity is seen at approximately 87^{o} from the sun. A marked aureole is present and extends out several tens of degrees from the sun.

Measurements on May 1973, at Interior Alaska

Figure 12 illustrates sky brightness at two wavelengths (500nm and 700nm) in the almucantar on May 3 and 4, 1973. Conditions on May 3 were

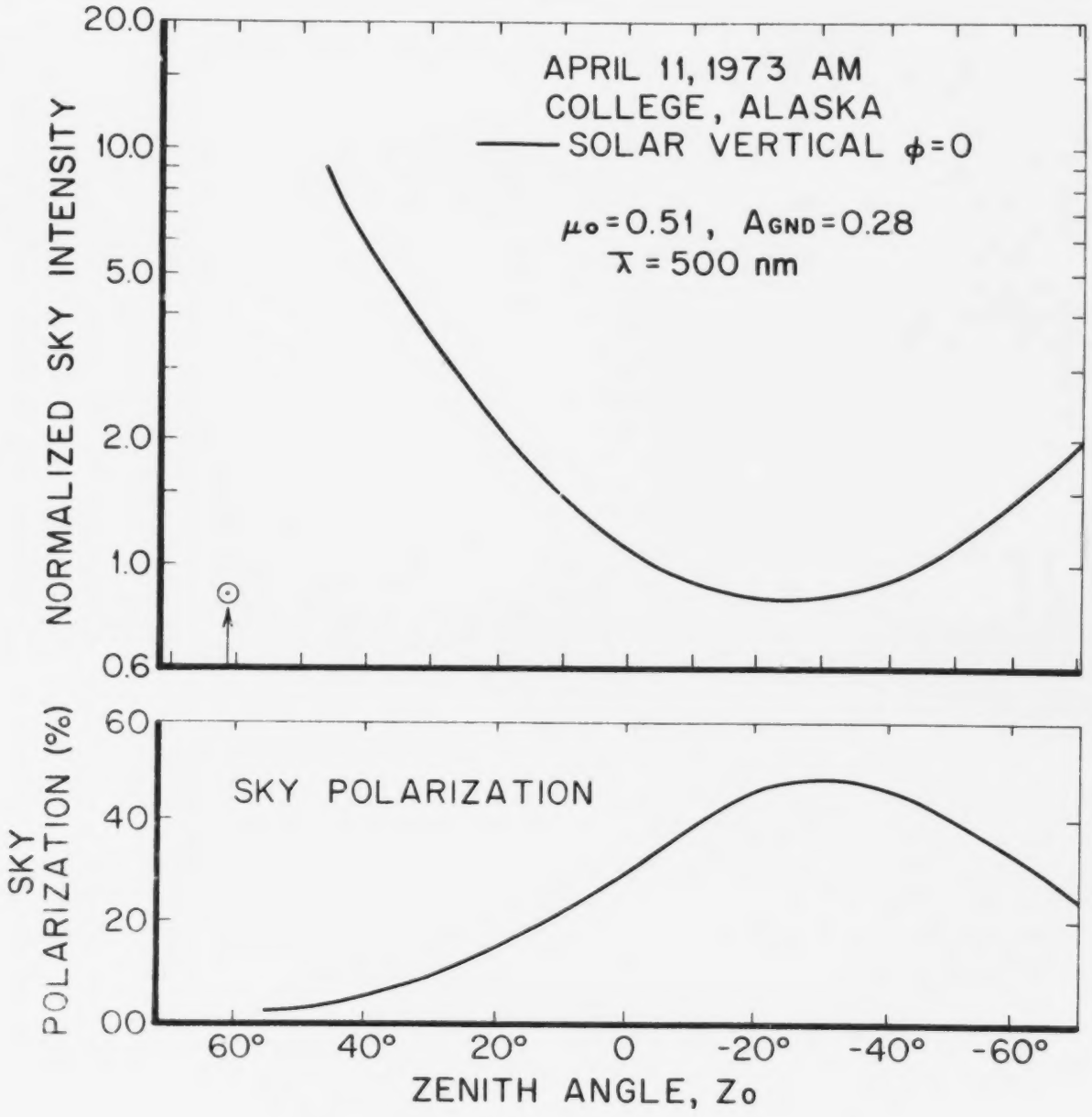

Figure 11a Sky intensity on April 11, 1973 at College, Alaska at 500nm. Normalized to 1.0 intensity unit at the zenith.

Figure 11b Sky polarization ratio in solar vertical plane.

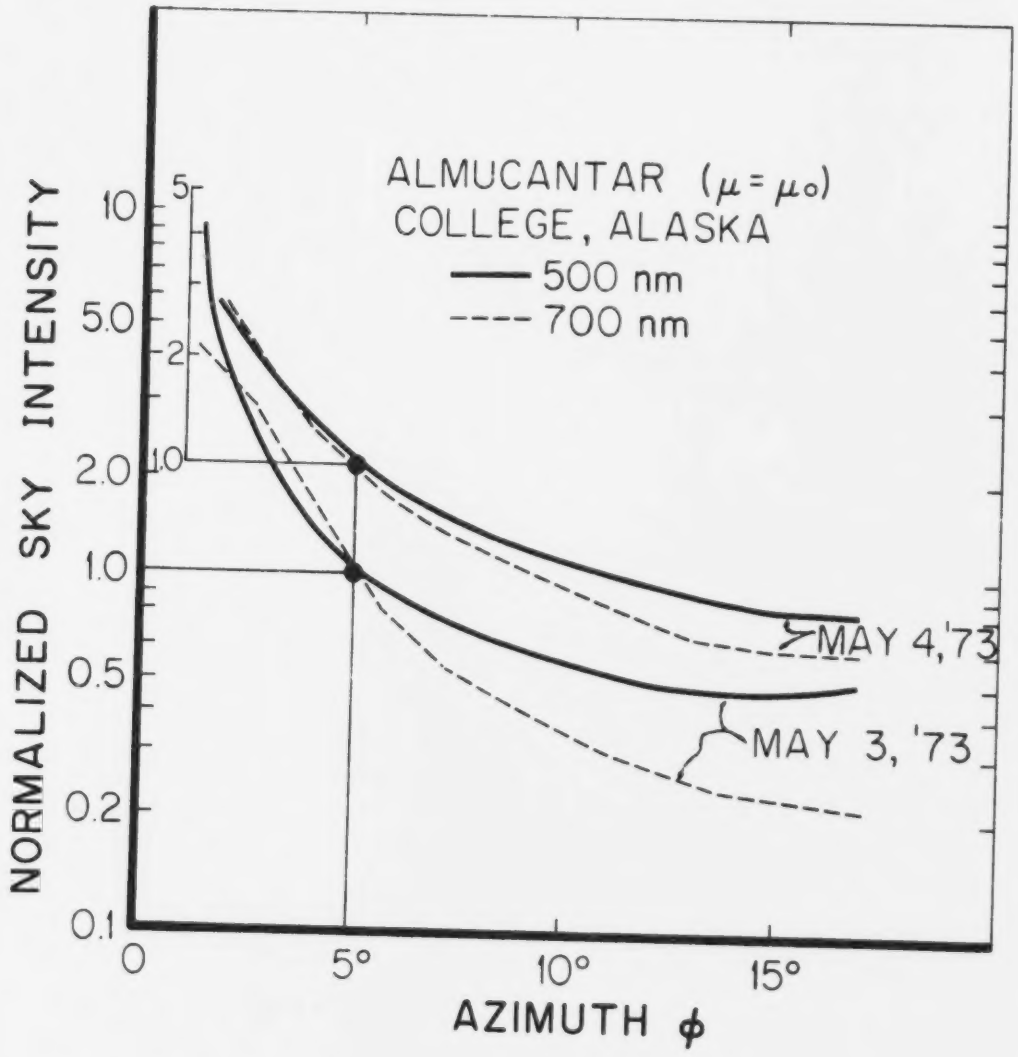

Figure 12 Sky intensity in the solar almucantar at 500nm and 700nm normalized to 1.0 intensity unit at ϕ = 5°.

as follows: horizontal visibility, 225km; air temperature, 18°C; wind, from E at 7 m/s; sky cover less than 5% cirrus. Slight mottling noticed near horizons. The data in Figure 12 were acquired with a collimator photometer, MKI, which was later superseded by a more carefully designed model with better baffling. Again, as in Figure 11, the ordinate scale intensities are normalized, in this case to 1.0 at 5° azimuth from the sun. Figure 12 also illustrates similar data for May 4, 1973, from the C.T. Elvey building in Fairbanks. Visibility, 250km; temperature, 23°C; wind, 12 m/s from N.E. The aureole brightness gradient is slightly smaller on this day in comparison to May 3 (Figure 12).

Measurements During Forest Fire Episode-July, 1973

Figure 13 shows measured (solid) sky intensity (in absolute intensity units) in the solar almucantar (Figs. 13a and 13b) and in the solar vertical plane (Figs. 13c and 13d) on July 25, 1973, during a time when an intrusion of smoke had penetrated into interior Alaska from forest fires which were burning at the time in Eastern Siberia. Curves are presented for mean wavelengths of 500nm (green) in Figures 13a and 13c and 700nm (far red) in Figures 13b and 13d. Figures 13a and 13b refer to the solar almucantar, and Figures 13c and 13d refer to the solar vertical plane. The optical depths, measured with the sun photometer, during the period were: $\tau_T(500nm) = 0.360$, $\tau_T(700nm) = 0.190$. Subtraction of the components arising from Rayleigh scattering and ozone absorption (Elterman, 1968) yields the following numerical values for aerosol, or Mie, optical depths: $\tau_M(500nm) = 0.214$, and $\tau_M(700nm) = 0.146$.

In Figure 13, we show curves of sky intensity (dashed-lines) that would result from a pure Rayleigh-scattering atmosphere with no contamination,

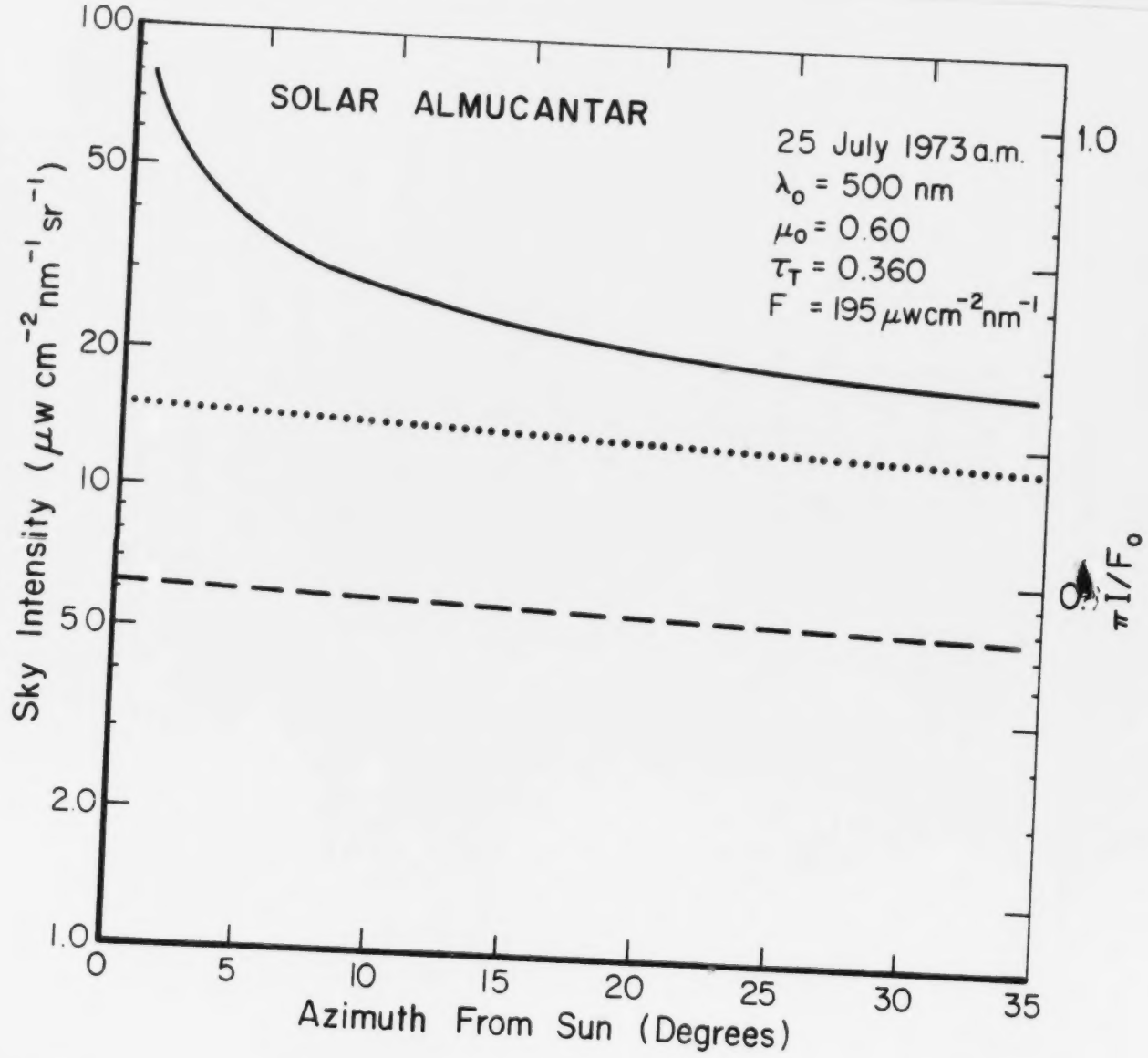

Figure 13a Sky intensity in the solar almucantar on July 25, 1973 at λ = 500nm, College, Alaska.

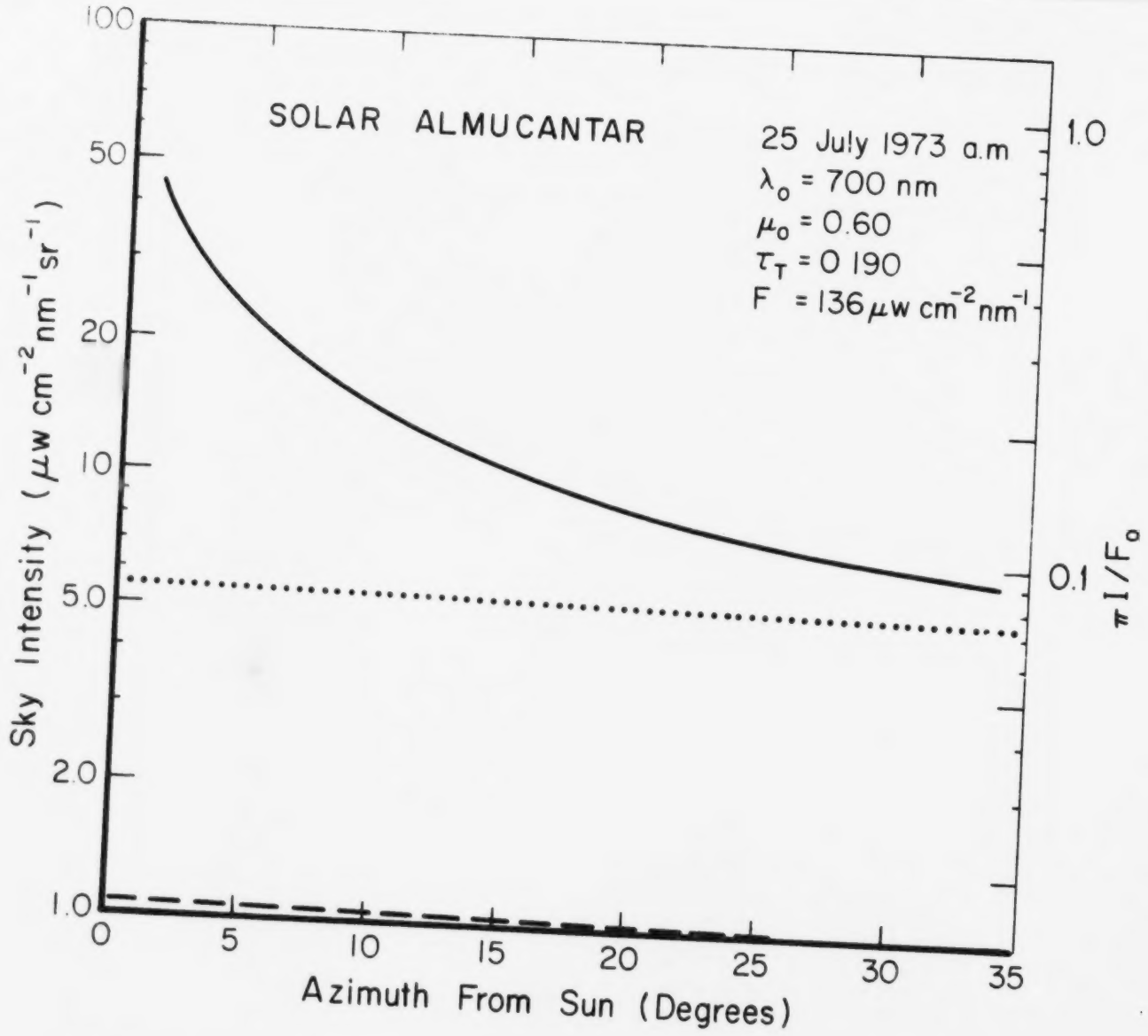

Figure 13b Same as above, except at λ = 700nm.

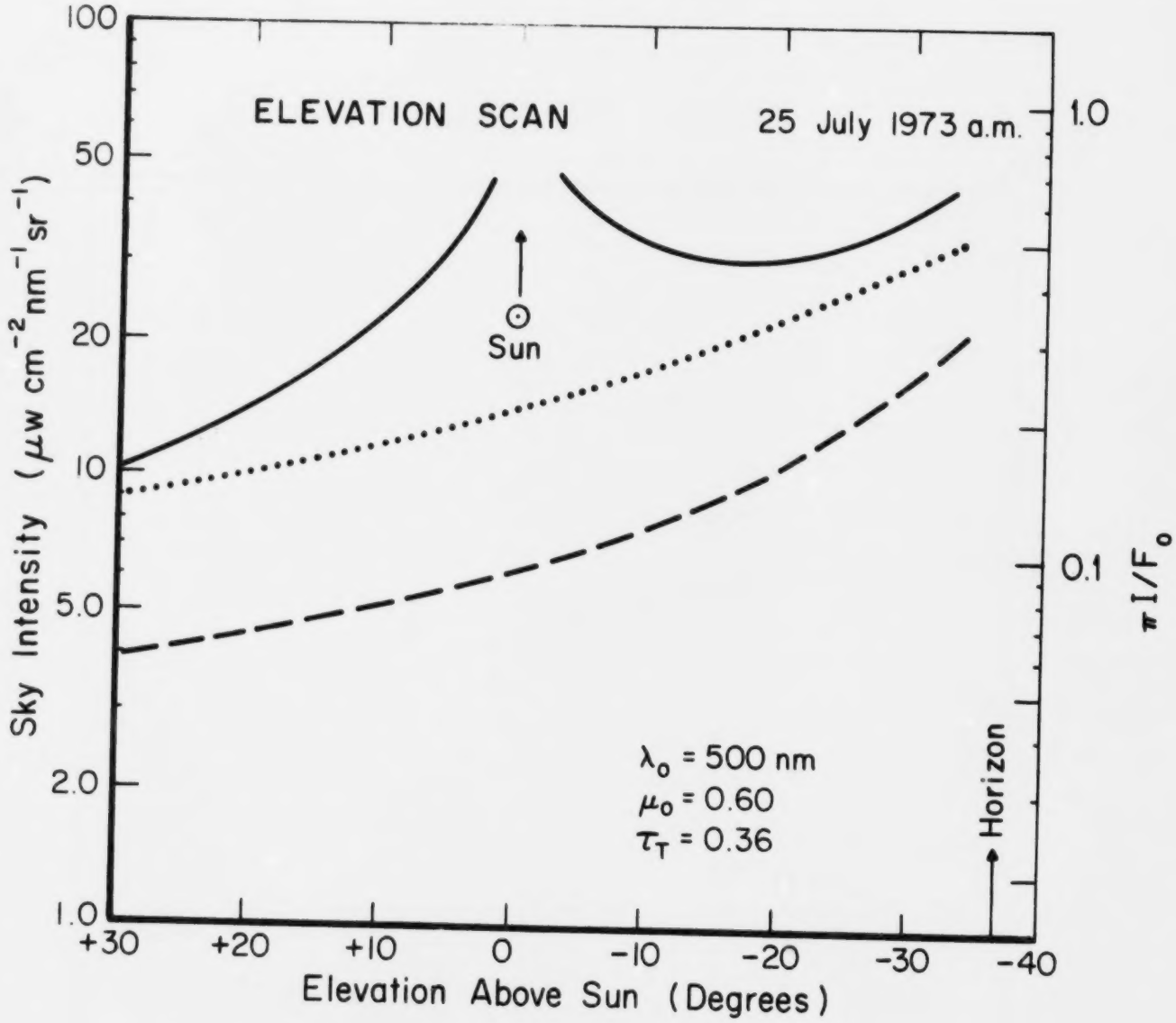

Figure 13c Sky intensity in the solar vertical plane on July 25, 1973 at λ = 500nm.

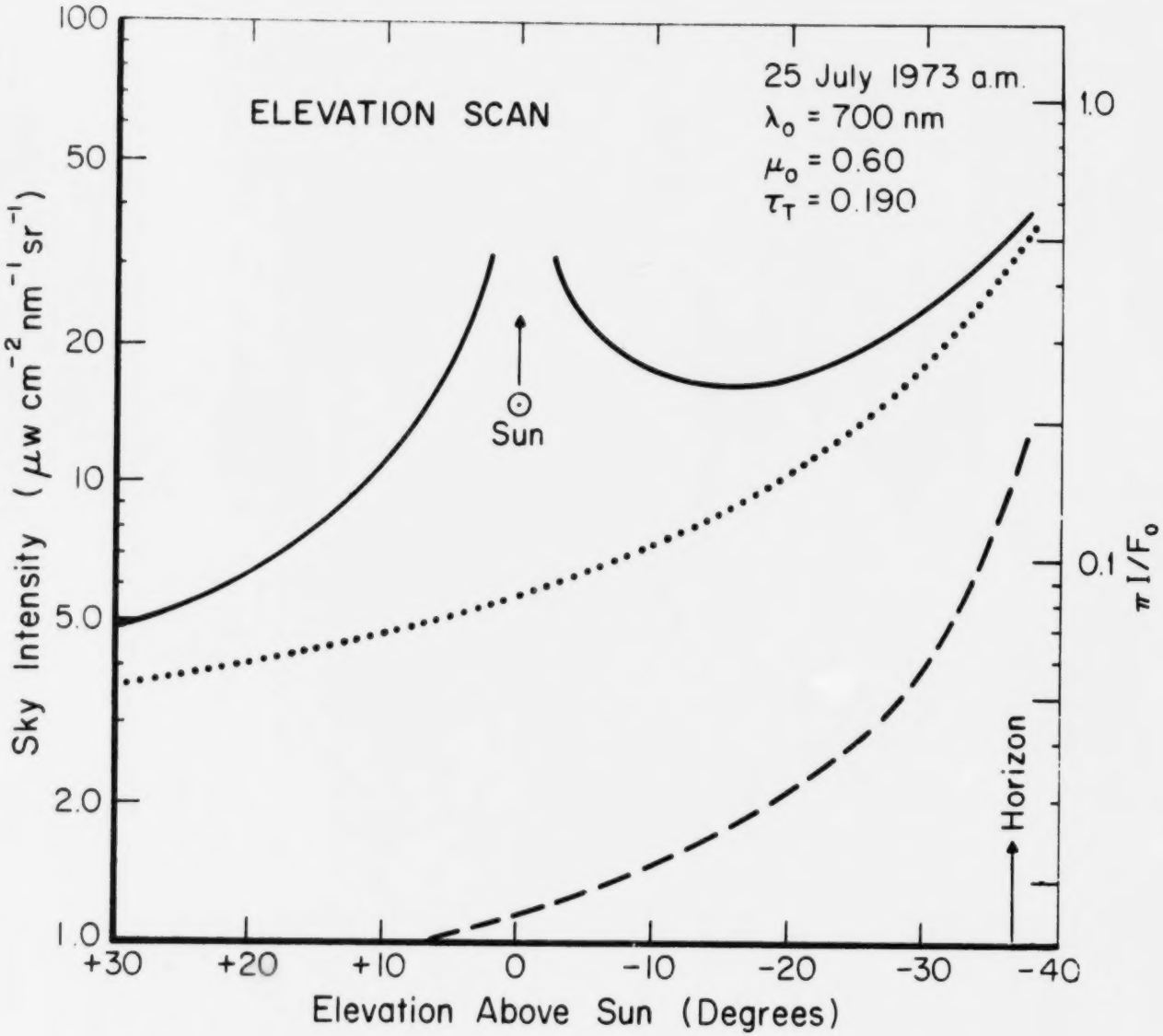

Figure 13d Same as above, except at λ = 700nm.

i.e., $\tau = \tau_{Rayleigh}$. These curves were extrapolated from the tables of Coulson et al. (1966) and include effects of multiple scattering and surface reflectivity. The dotted curves correspond to an atmosphere having optical depth equal to the total observed (Mie plus Rayleigh) optical depth on July 25th and scattering in accordance to the Rayleigh scattering mechanism. It is obvious that this theoretical curve is a better approximation to the observed sky intensity in Figure 13. The observed intensity is larger than the equivalent Rayleigh atmosphere for relatively small scattering angles, but smaller at larger angles. This implies that the aerosol scattering function $P(\theta)$, is strongly "peaked" in the near-forward direction and the deficit radiation at large scattering angles (where $I_{obs} < I_{\tau_{equiv}}$) is compensated for by enhanced scattering in the forward directions. Qualitatively, a strongly peaked phase function is consistent with the hypothesis of scattering from a volume of air containing aerosol particles that have sizes "of the order" of the wavelength of the illuminating radiation.

A value of surface albedo equal to 0.15 was used to obtain the calculated curves in Figure 13. This value seems reasonable for the conditions that existed at that time, namely full vegetative growth of mixed coniferous forests and scrub black spruce interspersed with low brush and clear areas.

To support the value of A = 0.15, we made measurements of surface albedo from the roof of the Elvey building on July 25, 1973. During these measurements, the solar elevation was within five degrees of its value for the sky brightness data shown in Figure 13. Table 2 shows the averaged results.

Table 2

Values of surface albedo measured at College, Alaska

Type of surface	Albedo at 500nm* (percent)	Albedo at 700nm* (percent)
Coniferous forest	3%	7 to 9%
Green freshly cut lawn	5%	10 to 12%
Dead grass	10%	20 to 24%
Asphalt Pavement	6%	22%

*Albedo values are with respect to a perfect horizontal Lambertian reflector.

The atmospheric sky intensity in Fig. 13 is substantially larger than theoretical predictions based on a Rayleigh atmosphere; the difference of course is due to scattering by aerosols, which were smoke particles in this case.

The data illustrated in Figure 13 were taken with a photometer with a collimating tube containing many baffles. The calibration procedure which is required to convert the raw voltage readings into radiant absolute intensities has been described in a previous section. The calibration constant for the instrument is considered to be accurate to within one or two percent at large angles from the sun; but degrades slightly for measurements taken closer than approximately fifteen degrees from the sun due to the extraneous light that enters the optical system from diffraction of sunlight at the entrance aperture and baffles.

Meteorological conditions during the observations of July 25, illustrated in Figures 13a through 13d, were as follows: temperature, $+22^{o}C$; wind from E at 7 m/s; mean solar elevation, 37^{o}; horizontal visibility estimated at 20km. The sky was clear, but the horizon was indistinct; the sky near the horizon appeared yellowish-brown and the

air quite obviously smokey. Visually, the aureole around the sun appeared much larger than usual and brighter, although these observations of aureole appearance are quite subjective.

The aerosol scattering phase function, $P(\theta)$, was derived from the curves in Figure 13 by the perturbation method described previously. Figure 14 illustrates the phase function (heavy line) so derived. Notice that the scattering phase function has a smooth monotonic shape with little indication of diffraction ring phenomena such as one might find if the aerosols were mono-disperse. Computed phase-functions for aerosols distributed with a Junge power-law distribution are shown for comparison (deBary et al., 1965). Although the observed curve does not match any of the "computed" curves exactly, there is reasonable agreement to the curve computed for Junge exponent value, ν, equal to 4.0. One can, in any case, state that there is a tendency toward the larger (i.e., ν=4) values of ν.

In view of the various inaccuracies that come into play (such as instrumental diffraction, uncertainities in ground albedo, and the deviation between an exact solution to the equation of radiative transfer and the approximate solution based on first-order perturbation theory), one is probably not justified in trying to obtain more exact matches to $P(\theta)$ curves computed for more complex aerosol distribution functions.

The scattering phase function, $P(\theta)$, on July 25th corresponds to scattering mostly from relatively small particles because the $r^{-(\nu+1)}$ dependence of the Junge size distribution function implies relatively smaller concentrations of giant and large particles when ν is fairly large as it is during this episode (Junge, 1963). This observation is

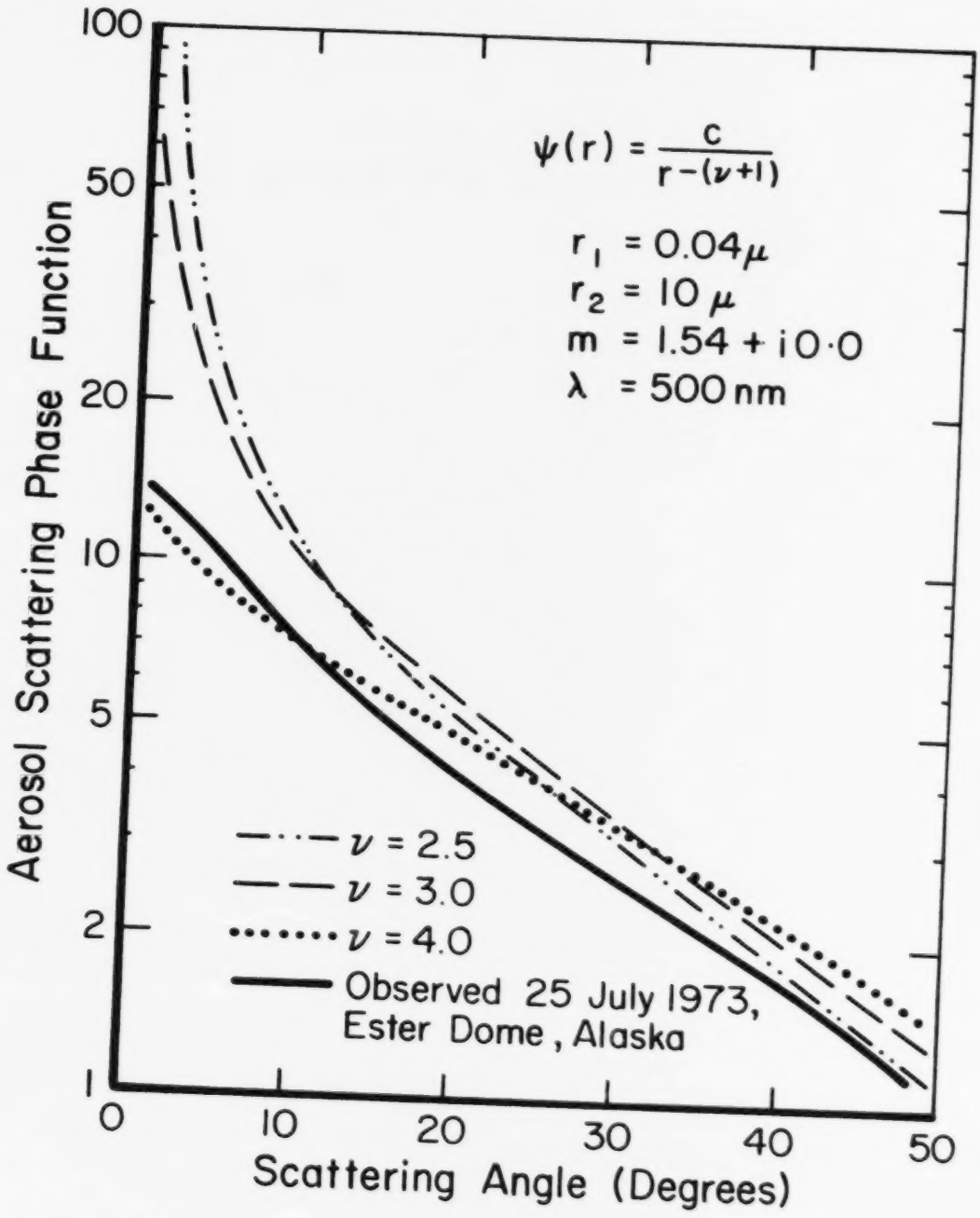

Figure 14 Aerosol scattering phase function, $P(\theta)$, for July 25, 1973. Curves computed for power-law distribution are shown as light lines for different values of power-law exponent.

consistent with the hypothesis that the aerosols derived from forest fire smoke consist of large concentrations of particles in the $r < 1.0\mu$ size.

Aerosol Optical Depths Inferred from Sky Intensity

The aerosol optical depth, $\tau_M(\lambda)$, can be inferred to some extent from the sky intensity measurements themselves. From Eq. 12, one can see that when $P_M(\theta) = P_{RAYLEIGH}$ the perturbation intensity is zero and therefore the measured sky intensity should be equal to the "equivalent Rayleigh" sky intensity computed for $\tau=\tau_T$. When plotted together on a graph, the value of the Rayleigh function, $P_R(\theta) = 0.75(1 + \cos^2\theta)$, and a typical aerosol phase function, $P_M(\theta)$, become about equal at a scattering angle of approximately 50^o (see Figure 15). The exact angle depends, of course, somewhat on the nature of the aerosol distribution function, but it is not as sensitive as one might expect, and $P_{(M)} = P_{(R)}$ varies only from 48 to 55 degrees as the power-law exponent varies from $\nu=2.5$ to $\nu=4.0$. Also shown in Figure 15 are curves for Deirmendjian's "haze M, L and H" (Deirmendjian, 1969).

In any event, the "crossing" of the $P_M(\theta)$ curve with the $P_{Ray}(\theta)$ curves would be expected to occur in the range $\theta = 45\text{-}55^o$ for any "reasonable" distribution of aerosols. One can thus immediately derive an estimate of the aerosol optical depth, $\tau_M(\lambda)$, by measuring the monochromatic sky intensity in the almucantar at a scattering angle (not to be confused with an azimuth angle) of 50^o from the sun and matching to pre-computed curves of sky intensity for a Rayleigh atmosphere as a function of optical depth, $\tau(\lambda)$. Figure 16 shows curves of sky intensity in the almucantar at an angular distance of 50^o from the sun as a function of total optical depth. Figure 16a shows the sky intensity for

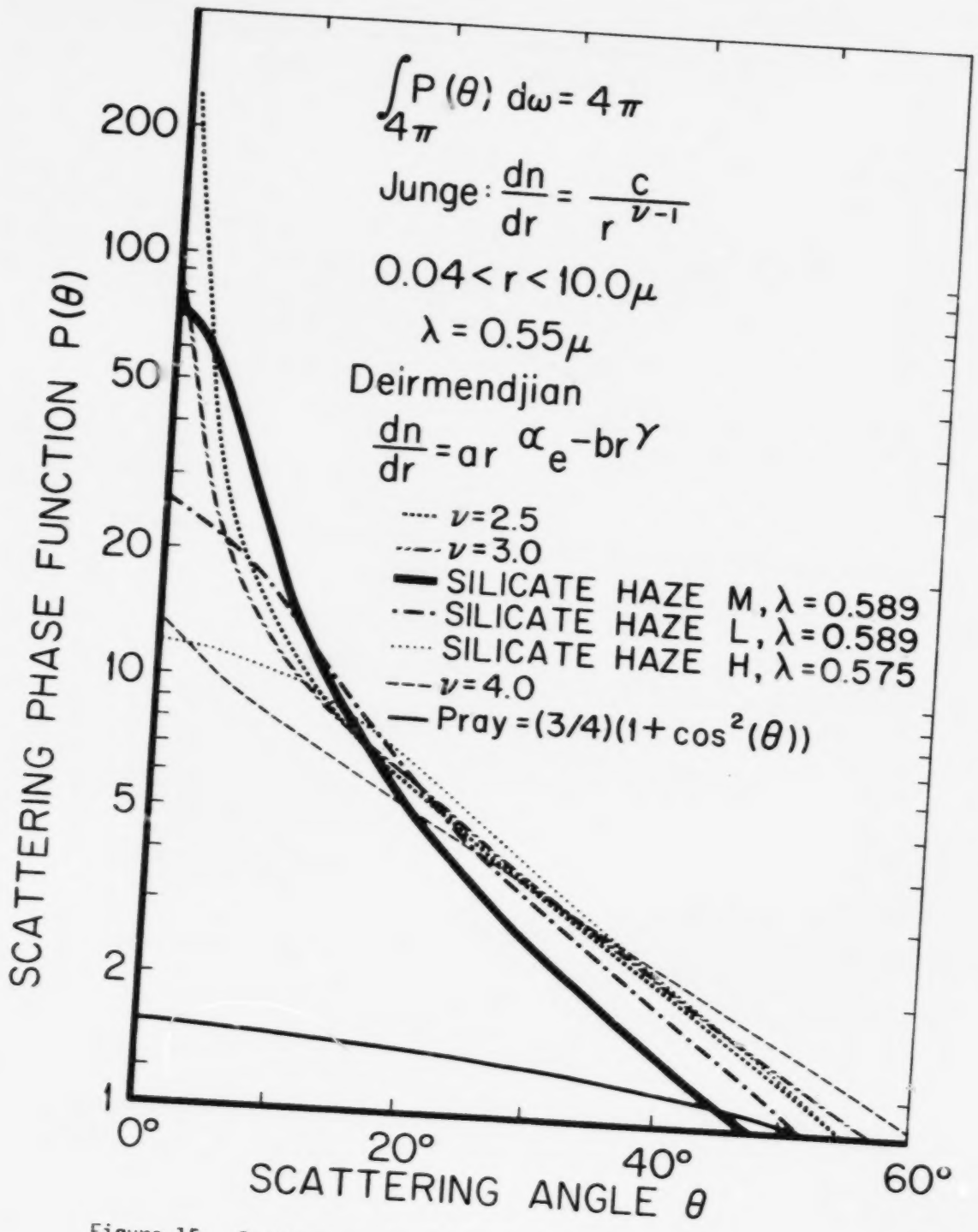

Figure 15 Scattering phase function, $P(\theta)$, computed for different aerosol size distribution functions.

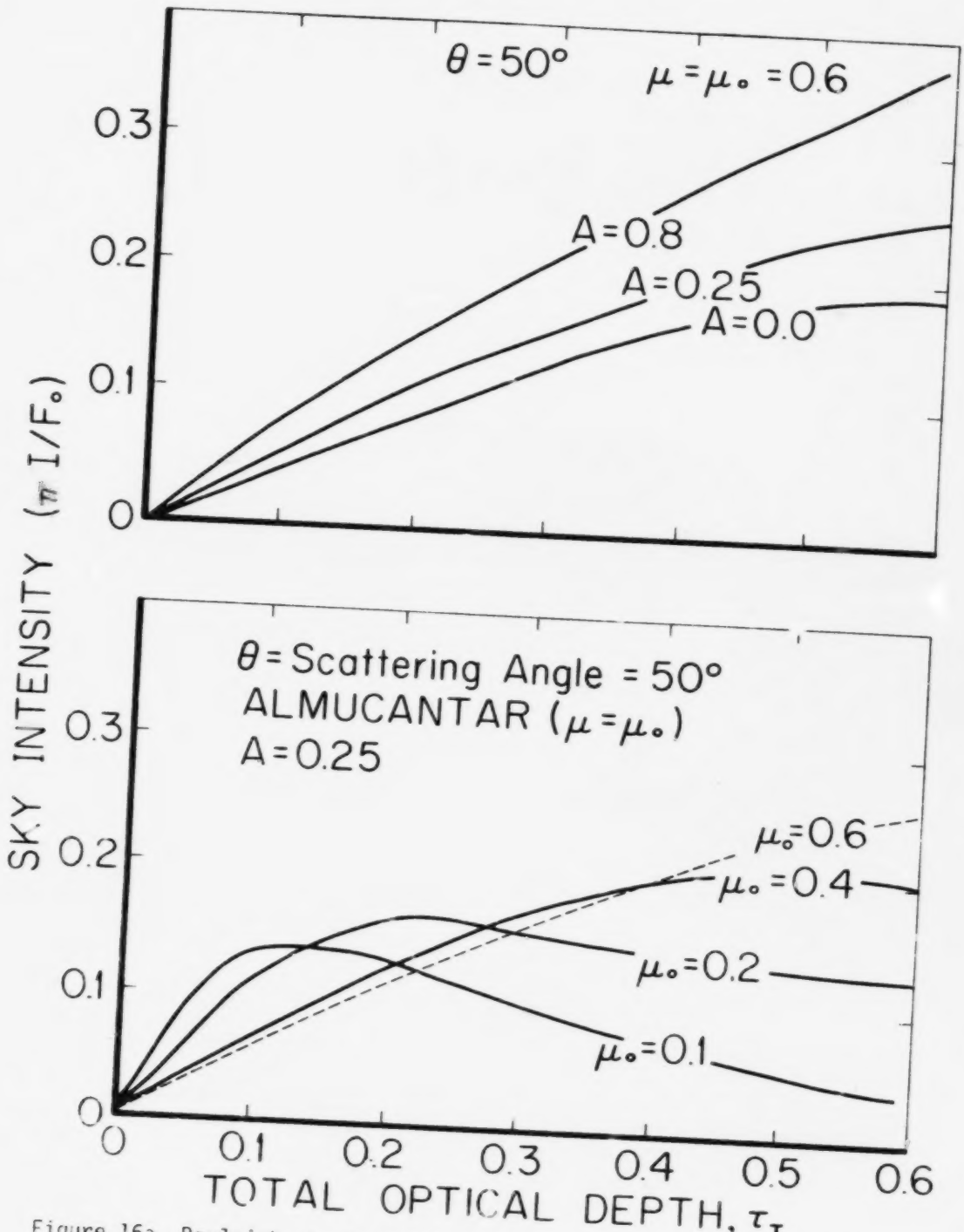

Figure 16a Rayleigh sky intensity, $\pi I/F_0$, in the solar almucantar at an angular distance of 50° from the sun plotted against optical depth τ for three values of surface albedo, A.

Figure 16b Same as above except for four values of μ_0.

three values of ground albedo, A, for $\mu=\mu_o=0.6$. Notice that one must know the ground albedo rather accurately in order to use this method of deducing optical depth. The curves in Figure 16 were derived from the computed solution to the equation of transfer for a Rayleigh scattering mechanism (Coulson et al., 1966). Figure 16b illustrates the dependence of sky brightness (at $\theta = 50^o$ in the almucantar) with total optical depth for several different values of $\mu=\mu_o$.

One can deduce the total optical depth from sky intensity as follows: First, one measures the absolute sky intensity in the almucantar at $\theta=50^o$. Secondly, depending upon the value of μ_o, one can deduce τ_T from Figure 16. This method works best when the sun is relatively high (say, for example, $\mu=\mu_o=0.6$) it has important potential applications for deducing air turbidity values at background locations such as in the polar regions or in the central Pacific where the air turbidity can be extremely small and hence difficult to measure accurately by using standard sun photometry techniques.

African Measurements

During the 1973 African solar eclipse expedition, one of the authors (G.S.) made measurements of sky intensity from Loiyengalani, Kenya ($2^o45'N$, 36^o 42'E, elevation 370m msl) on the southeast shores of Lake Rudolf (Shaw, 1974). The aerosol optical depth on June 15, 1973 was measured to be 0.155 at λ = 500nm and 0.171 at λ = 700nm. Large values of τ, such as the ones just stated were commonly observed at Loiyengalani. Table 3 lists measured values from the period 6-13-73 to 6-30-73 at 500nm and 700nm.

Table 3

Values of aerosol optical depth at Loiyengalani, Kenya at wavelengths of 500 nm (Gn), and 700 nm (Rd).

Date (1973)	τ_M(Gn)	τ_M(Rd)	Date (1973)	τ_M(Gn)	τ_M(Rd)
6-13	0.36	-	6-20	0.225	0.25
6-14	0.35	-	6-22	0.15	0.20
6-15	0.15	0.17	6-24	0.17	0.22
6-16	0.11	0.175	6-25	0.095	0.16
6-17	0.15	0.195	6-27	0.040	0.095
6-18	0.15	0.19	6-30	0.29	0.17
6-19	0.15	0.20			

As can be seen from Table 3, the aerosol optical depth in the red (700nm) is generally larger than in the green (500nm). This anomalous behavior is probably due to the fact that the African sub-Sahara aerosols have many larger size particulates ($r>1$ micron). This suggests that the aerosols might originate from windblown dust which is probably carried to great heights by convection. This surmise is strengthened by concurrent estimates of the horizontal visibility which were judged to be generally better than one would expect considering the high optical depths observed. Loiyengalani is located in an arid zone of East Africa with a moisture index of approximately 55 (National Atlas of Kenya, 1970). The surrounding terrain is barren except for scattered patches of bushed grassland. The ground albedo was measured photometrically in the mid-visible; however, only half this value was used in the calculations for the Rayleigh atmosphere to account for the low albedo over the waters of Lake Rudolf.

One can obtain a rough indication of the aerosol extinction scale height, H_A, (the thickness that an aerosol layer would have if it were distributed in a homogeneous layer with constant extinction coefficient equal in magnitude to the appropriate ground-level volume extinction coefficient) as follows: Horizontal visibility is defined as the distance where the constrast of a black-on-white target decreases to 2%. This means that the horizontal transmission approaches a value of 0.02. Assuming that Beer's law is valid, one can write $T_{Horizontal} = \exp-(\beta_{oR} + \beta_{oM})L = 0.02$ where $\beta_{oR}(\lambda)$ is the molecular "Rayleigh" ground-level extinction coefficient and β_{oM} is the ground-level aerosol coefficient, L is the horizontal visibility, and $T(\lambda)$ the horizontal atmospheric transmission. The equation implies that

$$L[\beta_{oM}(\lambda) + \beta_{oR}(\lambda)] = 3.9 \qquad 18)$$

We note that the vertical aerosol optical depth, $\tau_M(\lambda)$, may be derived by measuring the apparent intensity of the sun. Furthermore, the values of τ_M and τ_R can be set numerically equal to the product of the scale height, H, and a ground level extinction coefficient $\beta_o(\lambda)$ (i.e., $\tau_M(\lambda) = H_M\beta_{oM}$ and $\tau_R(\lambda) = H_R\beta_{oR}$). By combining these expressions, one obtains,

$$H_M = \frac{\tau_M(\lambda)}{\frac{3.90}{L} - \beta_{oR}(\lambda)} \qquad 19)$$

Thus by combining measurements of the horizontal visibility, L, with measurements of the Mie optical depth, τ_M, one can derive a value for the aerosol scale height, H_M. Doing this for the measurements in Kenya, we deduced that the aerosol scale height is of the order of 6 ± 2km; about 3 to 4 times larger than values typically found in interior Alaska in

spring. The larger values of H_M in the tropics no doubt arise from a combination of enhanced local convection and Hadley cell transport of surface-generated aerosols.

Figures 17a through 17c show measurements of sky intensity in the solar vertical and in the solar almucantar at λ = 500 nm and λ = 700 nm at Loiyengalani. The scattering phase function deduced from these data is illustrated (along with several other days' data) in Figure 18.

It is seen that considerable differences arise from one observation period to the next. This, of course, reflects the fact that the physical characteristics of the aerosols change with location, season, and synoptic situation. Notice that the phase function curve derived on 15 June at Loiyengalani, Kenya fits reasonably well to a Junge distribution (shown as light lines in Figure 18) with a value of the exponent, ν, equal to 2.5. This relatively small value of ν is almost certainly associated with the fact that the aerosols, in this particular instance, were predominantly large, typical of what one might expect for windblown dust (Joseph et al., 1973). Comparison with the large value of ν observed during the forest fire episode (predominantly small particles) indicates the usefulness of relating the measured aerosol scattering phase function to the size distribution function. This shows that the aureole method is useful in deriving information about origin of the aerosols.

Measurements on August 20, 1973

Figures 19a and b show curves of sky intensity measured on August 20, 1973, from Ester Dome, Alaska (64°53'N, 148°03'W). This was an

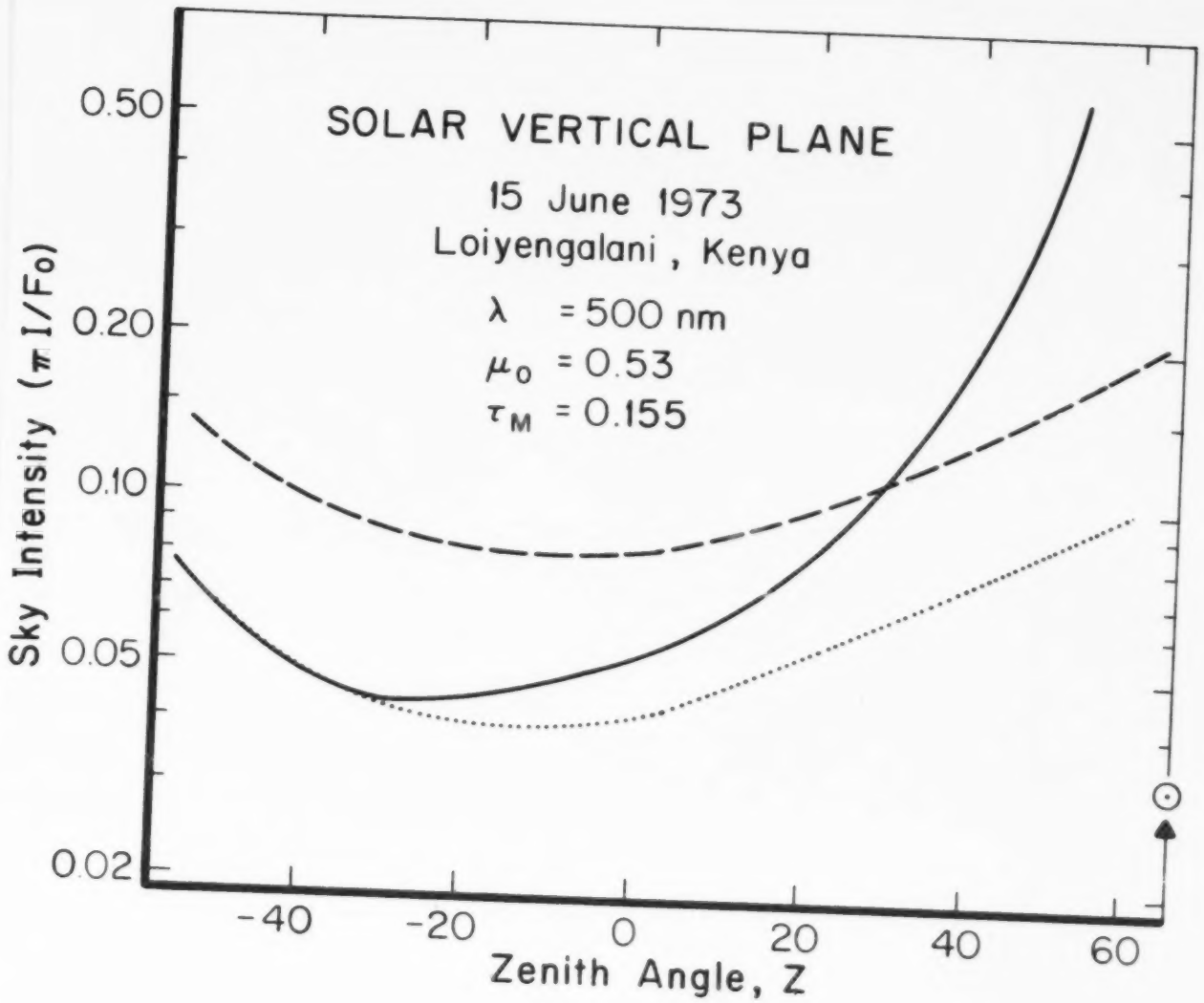

Figure 17a Sky intensity, $\pi I/Fo$, in the solar vertical at Loiyengalani, λ = 500nm.

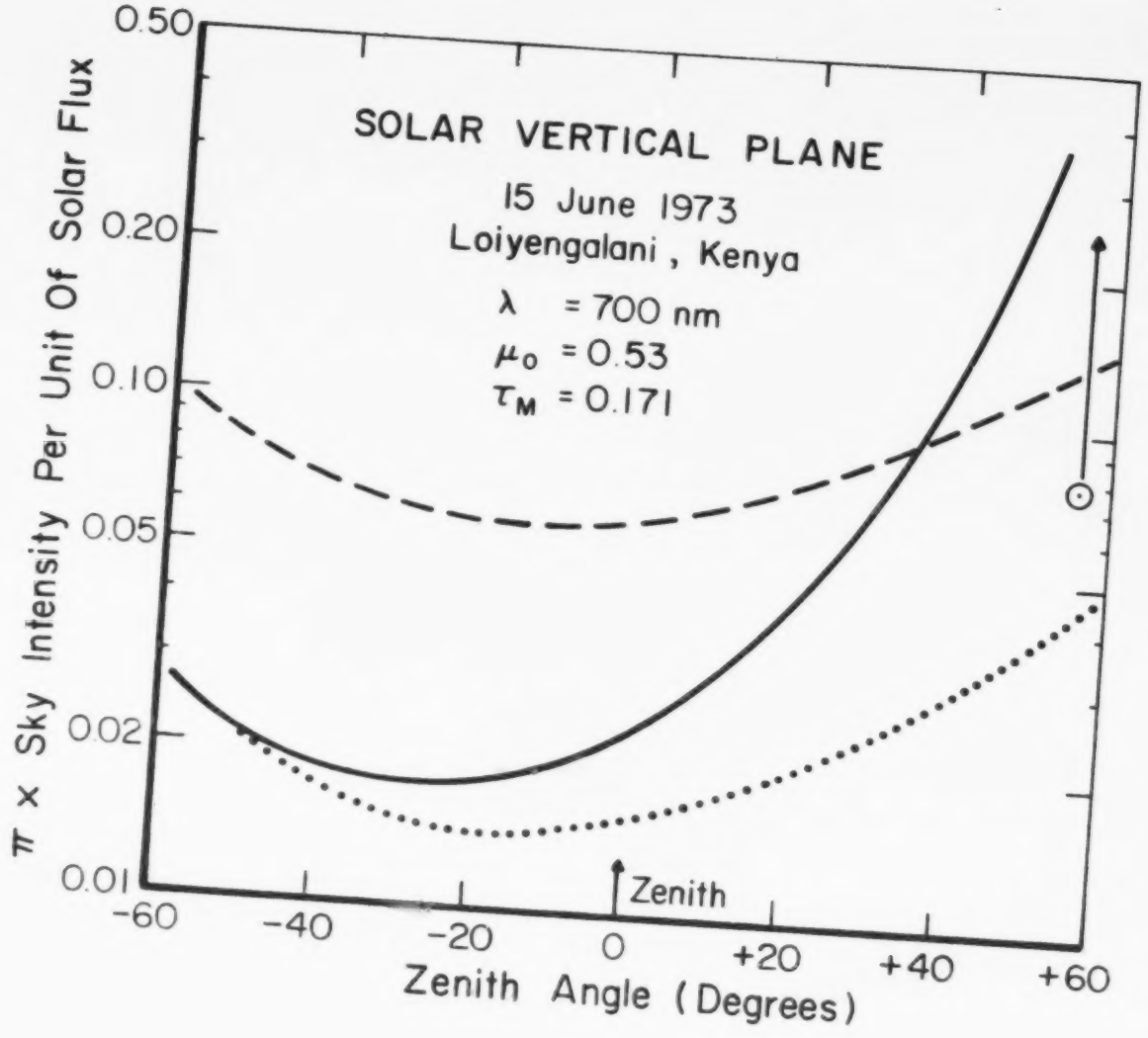

Figure 17b Same as above, except λ = 700nm.

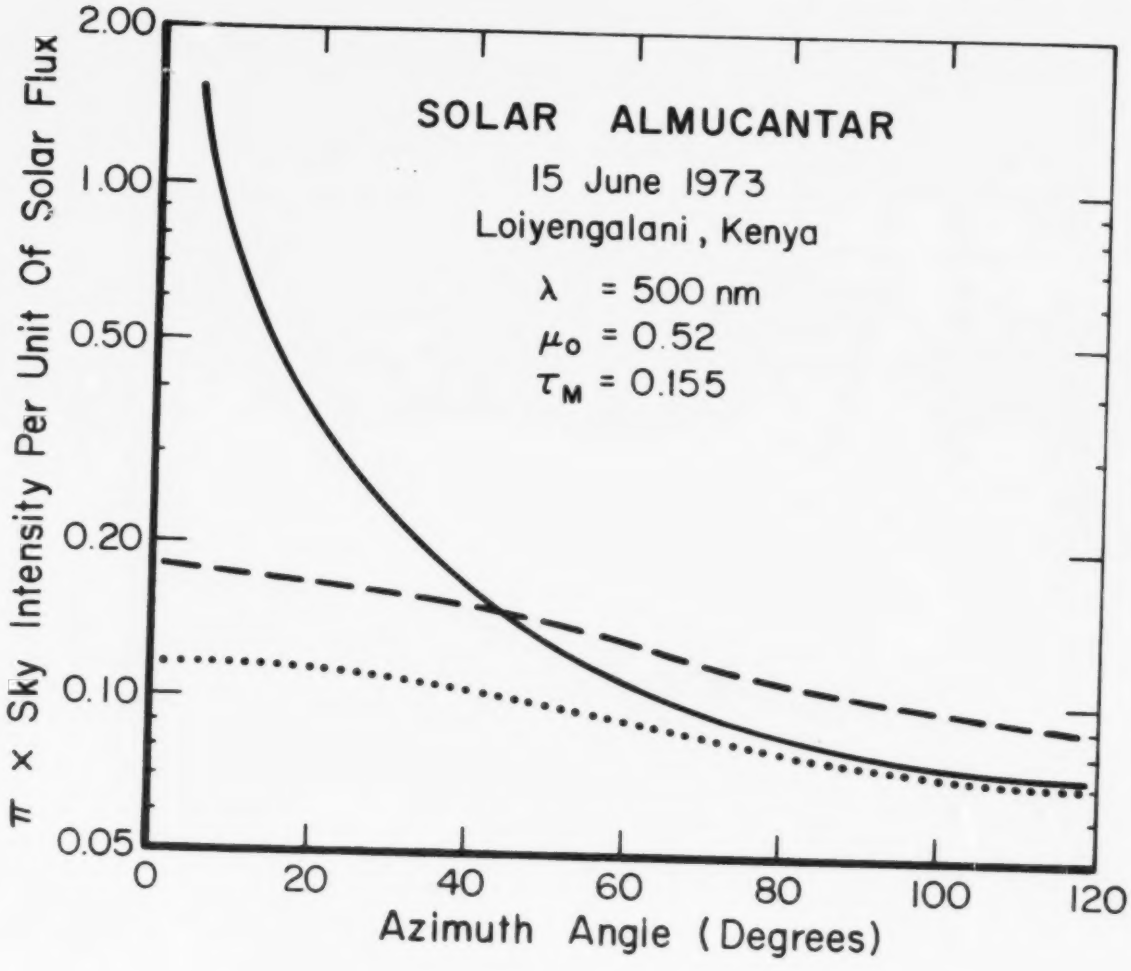

Figure 17c Sky intensity, πI/Fo, in the solar almucantar at Loiyengalani, λ = 500nm.

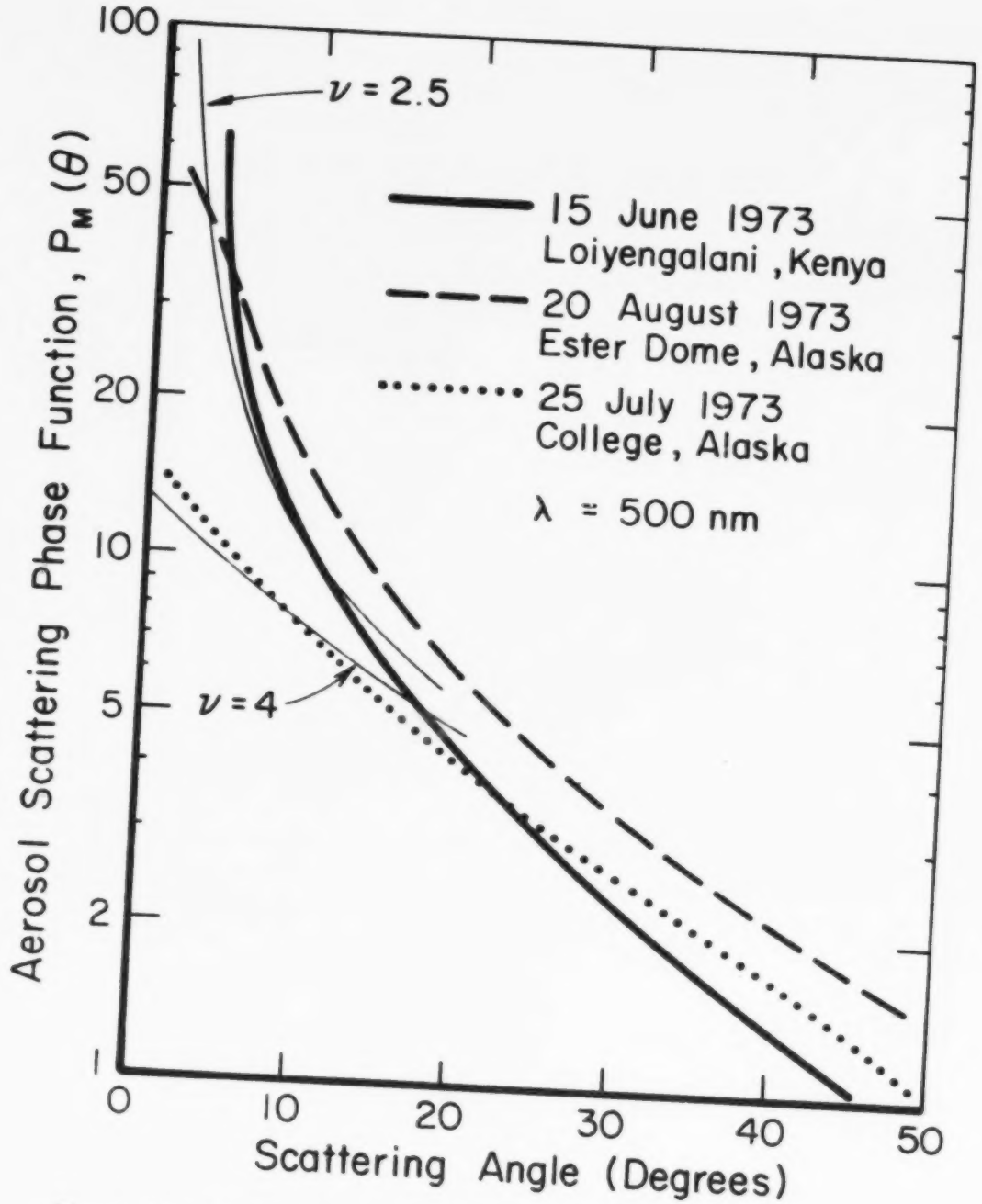

Figure 18 Aerosol scattering phase functions deduced from sky brightness measurements.

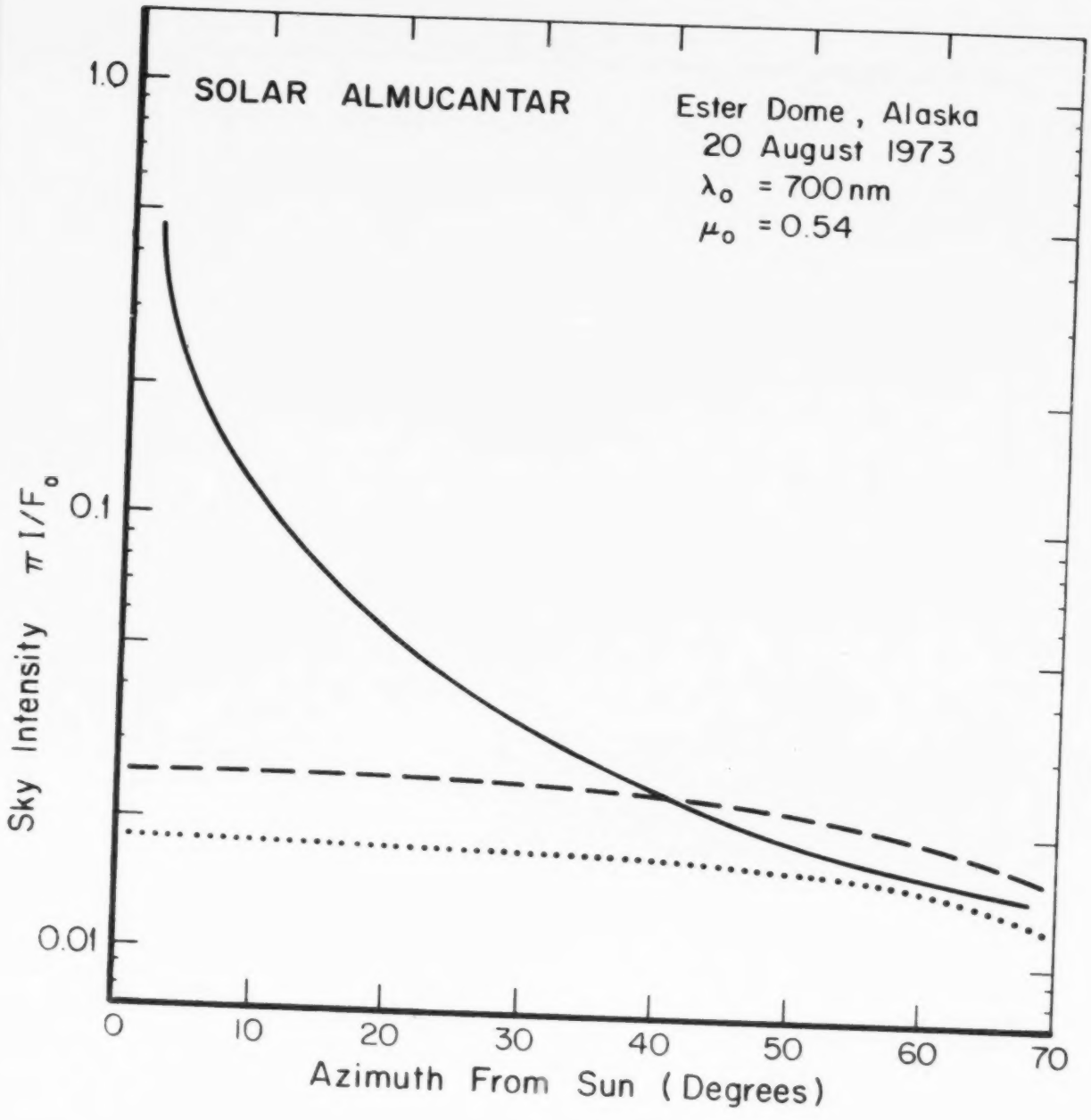

Figure 19a Sky intensity in the solar almucantar on August 20, 1973, λ = 700nm.

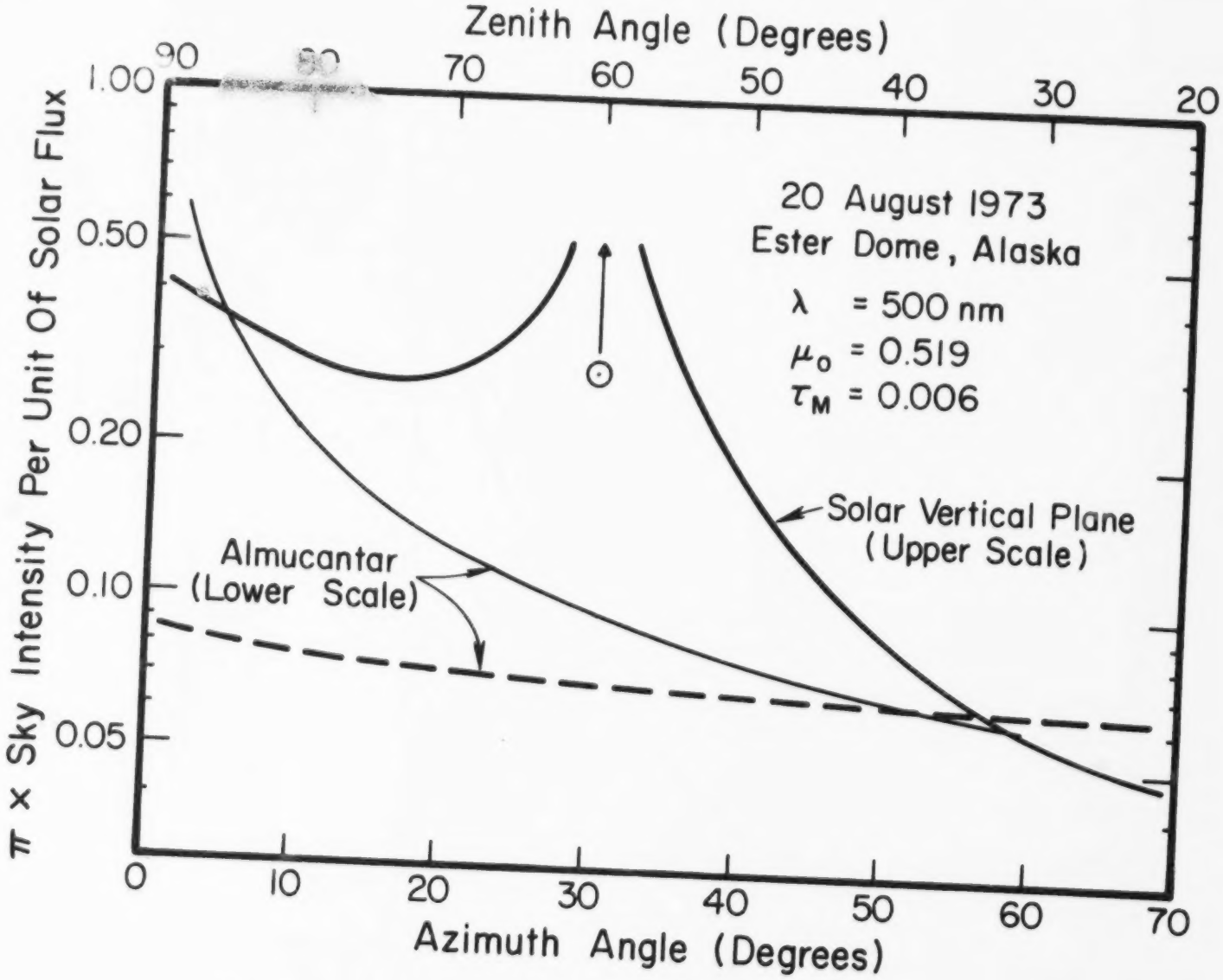

Figure 19b Sky brightness in the solar vertical plane on August 20, 1973, λ = 500nm.

extremely clear period with excellent sky conditons with no trace of striations. Horizontal visibility was estimated to be greater than 200 km since Mt. McKinley (distance 240 km) was easily visible with good contrast.

The optical depth arising from scattering and absorption from aerosols was so small on August 20th that it was extremely difficult to determine its value accurately from sun-photometer data. Even with this extremely minute aerosol optical depth, the effect of the atmospheric aerosols on sky intensity is obvious in Figure 19. The dashed lines in Figure 19 are calculated for an equivalent Rayleigh atmosphere having $\tau = \tau_{\text{Total Obs}}$ and the dotted line is for a pure Rayleigh atmsophere. The utility of the aureole method for assessing aerosols becomes apparent when one realizes that aerosol optical depths of these small magnitudes cannot generally be determined accurately when they are deduced entirely from sun-photometer methods.

Measurements on August 2, 1973

Figures 20a and b show diffuse sky intensity in the solar vertical on August 2, 1973. The data were taken from the roof of the C.T. Elvey building at the University of Alaska's Fairbanks campus. The optical depths were $\tau_M(500\text{nm}) = 0.10$, $\tau_M(700\text{nm}) = 0.069$. Perturbation theory analysis and comparison to pre-calculated curves of aerosol phase functions indicate a value of ν of approximately 2.5 which seems to imply large aerosols which may have originated at the surface and been carried upwards by convection which was obviously taking place this day since scattered cumulus were apparent along the horizon. (Incidently, the

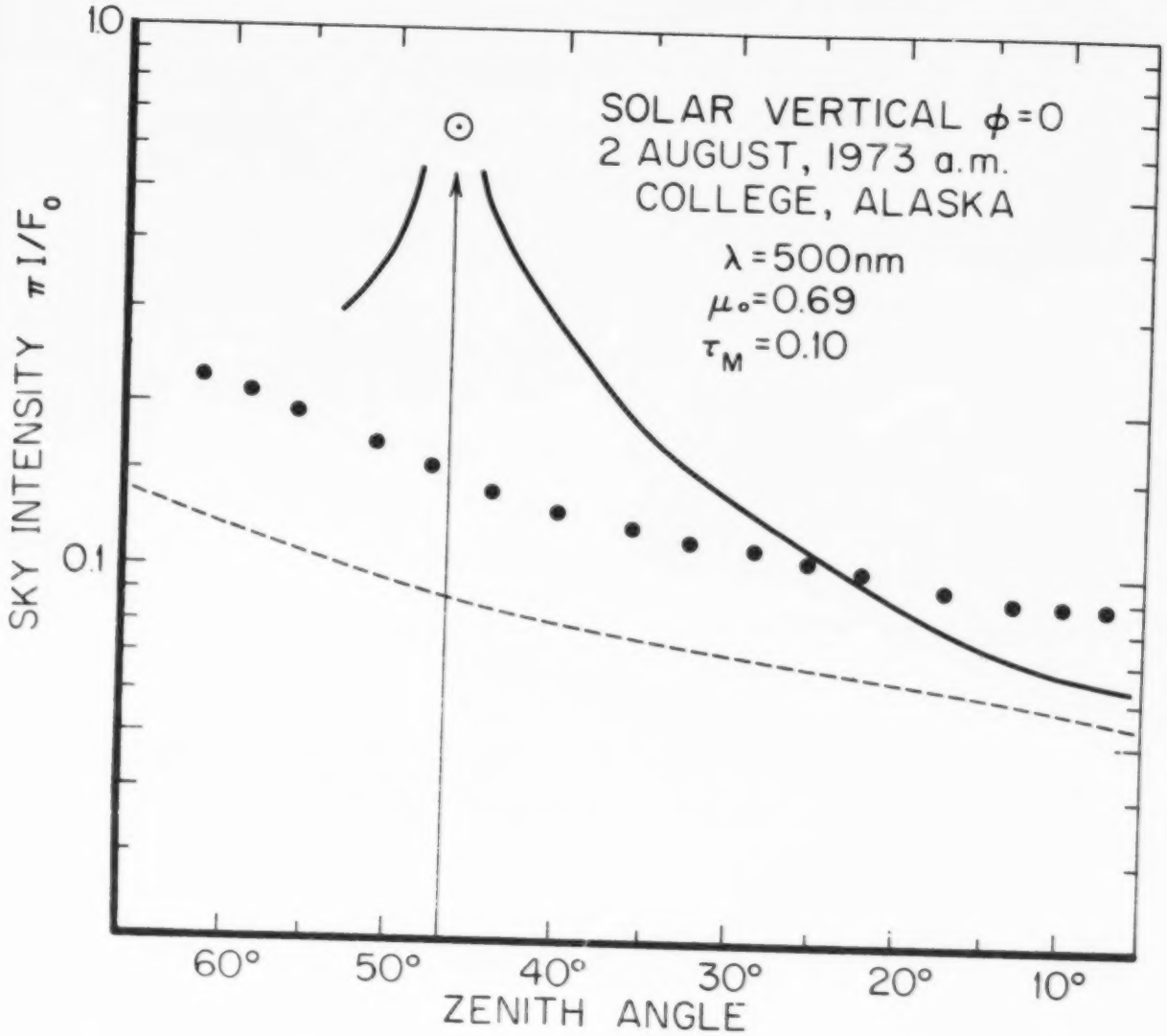

Figure 20a Sky intensity in the solar vertical plane on August 2, 1973, λ = 500nm.

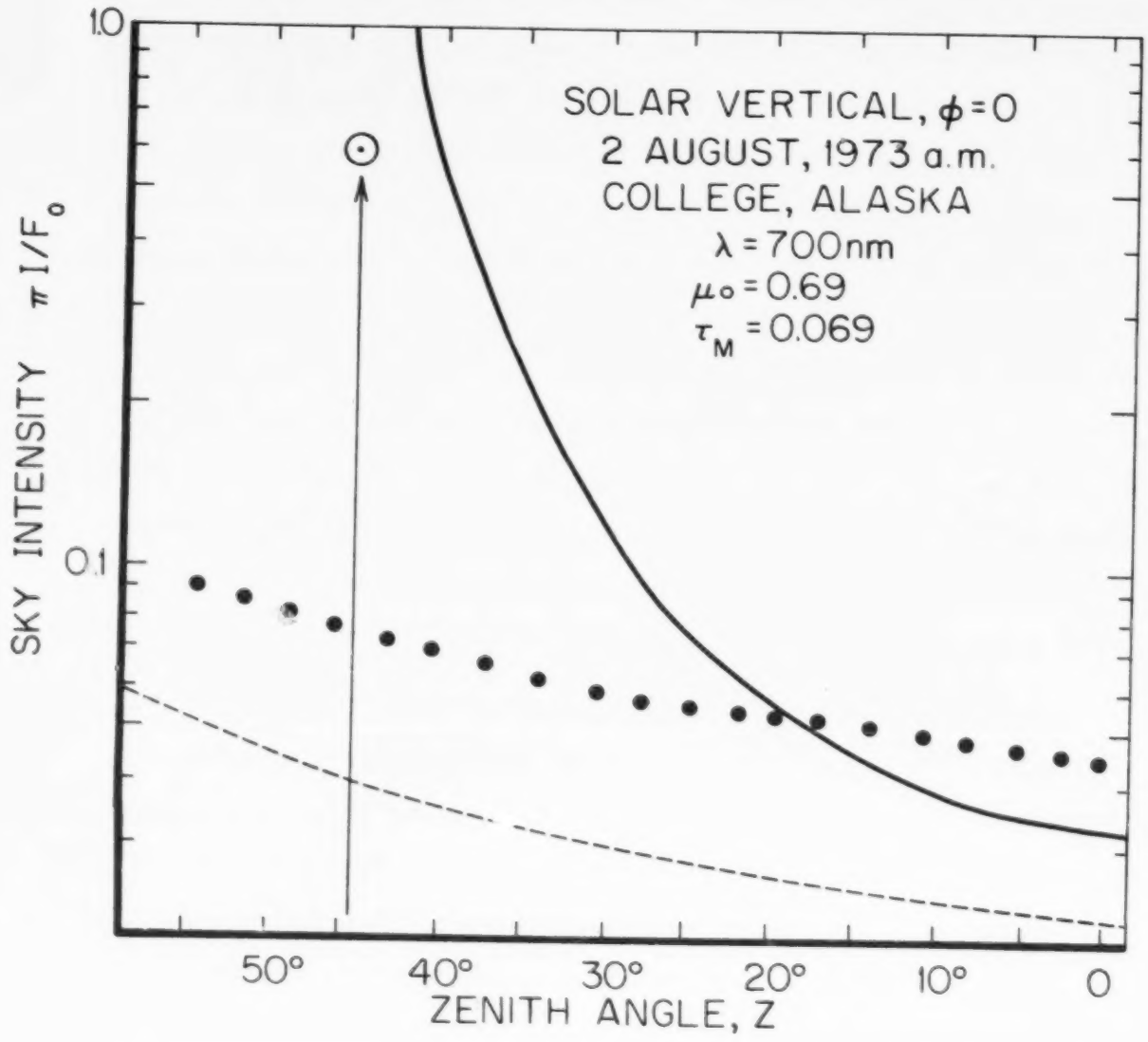

Figure 20b Same as 20a, except for λ = 700nm.

analysis is probably not as accurate when there are scattered clouds near the horizon, since their presence undoubtedly affects the sky brightness; however, on this day the clouds were not extensive and were mostly located close to the horizon, and therefore the error may not nave been large.) We remark that interior Alaska is extensively covered by eolian loess (wind deposited glacial silt) which would add to the large aerosol population under these conditions. Precipitation occurring ten hours before the observations probably scavenged out small aerosol particles in the air mass.

The unstable atmosphere, the extensive coverings of loess and the previous rain washout, along with the small ($\nu = 2.5$) value of power-law exponent all point to a mechanism of windblown fine dust carried upward by convective currents as the responsible agent for introducing aerosols into the air mass during this observation period.

The Effect of Cirrus Clouds on Sky Brightness

The presence of thin cirrus clouds modifies the sky radiation environment dramatically, especially at small scattering angles because of diffraction of light around the ice crystals. To illustrate the effect, we show, in Figure 21, the temporal variation of circumsolar sky intensity as measured with the coronameter. Measurements are shown for two wavelengths, 500 nm and 700 nm. At 12:50 LMT, a cirrus band of approximate width equal to 15^{0} was centered over the sun. This cirrus band was caused from a jet contrail which had been seeded approximately ten minutes earlier and which had spread out in a broad arc across the sky. As time progressed, the cirrus band diffused out and eventually evaporated. Figure 21 shows the attendant decrease of circumsolar sky

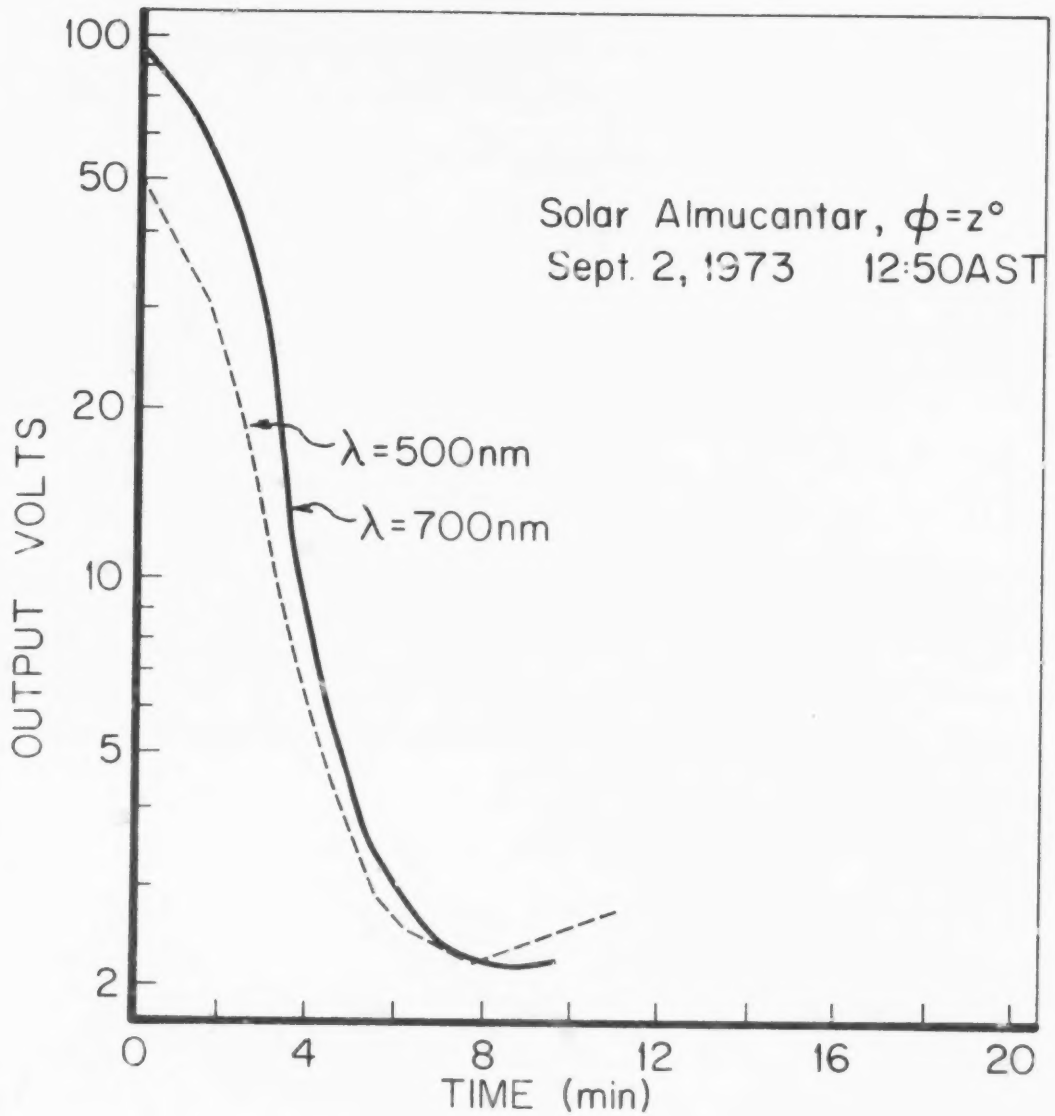

Figure 21 Temporal variation of sky intensity centered on an evaporating jet contrail.

intensity with time. Unfortunately, the coronameter was not calibrated and so the ordinate values can not be given in absolute units.

During the dissipation of the cirrus contrail, the Red/Green sky intensity ratio decreased with time and this implies a change of scattering particle size with time. Although these measurements are preliminary, it appears that it may be feasible to use this method of sky photometry to study the microdistribution of cloud particles.

Measurements on September 3, 1973

Figure 22 shows sky radiance at λ = 500nm on September 3, 1973. The solid lines refer to measurements made from Ester Dome (elevation 720m msl); the dashed line refers to measurements made from the University campus (elevation 213 m msl). Differences between the two can mostly be attributed to aerosols contained in the height interval 213m < h < 720m, (between Ester Dome and Fairbanks campus) although part of the change is due to a slight solar elevation change. The dotted line in Figure 22 indicates sky brightness for a pure Rayleigh atmosphere with τ_0=0.55. Although we have not done so, it is possible in this way to determine size distribution data on atmospheric aerosols contained in thin horizontal layers.

Aerosol Mass Loading

The mass of aerosols contained in a vertical column of air with unit cross-section, (g cm^{-2}), may be calculated if one has knowledge of the aerosol micro-distribution function (presumed not to vary with altitude) and the optical depth at one wavelength. Figure 23 shows the volumetric aerosol extinction coefficient, β(500nm) calculated for an assumed Junge power-law distribution function (Junge, 1963) with a

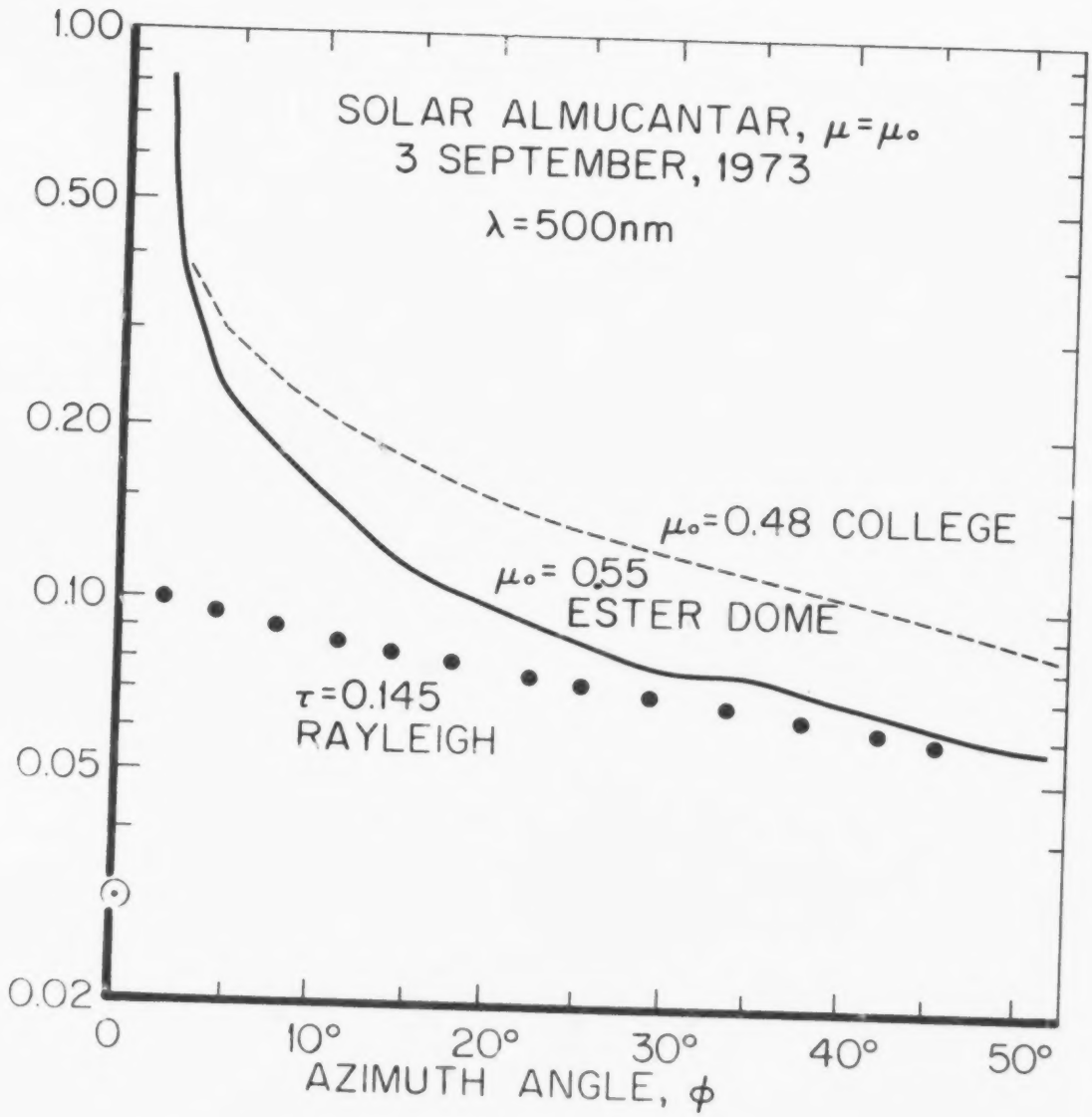

Figure 22 Sky intensity πI/Fo, on September 3, 1973, in the solar almucantar from Ester Dome, Alaska (solid) and from College (dashed).

constant volumetric mass-loading of 50 $\mu g\ m^{-3}$ and upper and lower cut-off diameters of 10μ and 0.01μ, respectively. The abscissa is equal to the Junge power-law exponent ν. It can be seen that, for a constant mass loading of aerosols, a power-law exponent numerically equal to 3.1 is most "efficient" for attenuating a light beam by scattering.

It is elementary to show that the following relation is true provided that the normalized size-distribution function is independent of height:

$$\Gamma = (1 \times 10^{-3})\ \tau(500nm)\ \frac{\gamma_o}{\beta_o} \qquad (g\ m^{-2}) \qquad 20)$$

where Γ is the aerosol columnar mass loading ($g\ m^{-2}$), τ the aerosol optical depth referred to the vertical, $\gamma_o = 50\ \mu gm^{-3}$, and β_o is the volume extinction coefficient (km^{-1}) calculated for γ_o at the appropriate wavelength (Figure 23) and value of inferred Junge exponent ν.

Using this technique we have calculated mass-loading values for several clear days; the results are summarized in Table 4.

Table 4

Values of Columnar Aerosol Mass Loading, Γ

Date	Location	$\tau_M(500nm)$	ν^*	$\Gamma(g\ m^{-2})$
15 June '73	northern Kenya	.155	1.7	0.26
25 July '73	Fairbanks, Ak.	.21	4.0	0.27
2 Aug '73	Fairbanks, Ak.	.10	2.5	0.07
20 Aug '73	Ester Dome, Ak.	.006	2.3	0.01
2 May '74	Fairbanks, Ak.	.18	3.4	0.09
27 March '74	Barrow, Ak.	.13	2.3	0.11
28 March '74	Barrow, Ak.	.11	3.3	0.06
30 March '74	Barrow, Ak.	.13$^+$	3.2	0.06$^+$
31 March '74	Barrow, Ak.	.13$^-$	2.5	0.09
2 Apr '74	Fairbanks, Ak.	.05	2.0	0.06
4 Apr '74	Fairbanks, Ak.	.03$^+$	3.1	0.02
17 July '74	McKinley Park, Ak.	.09	3.0	0.05

* ν is the value of the estimated Junge power-law exponent.

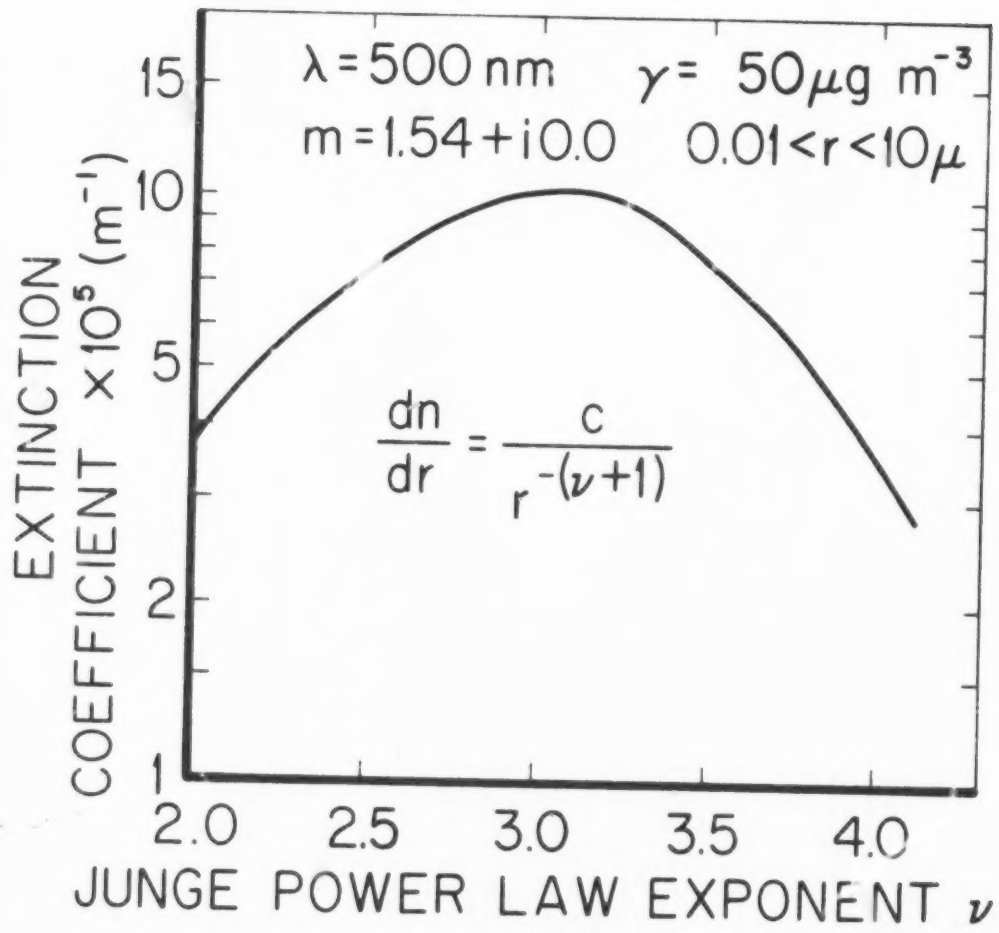

Figure 23 Volume extinction coefficient calculated for Junge power-law distribution for constant aerosol mass loading of 50 $\mu g/m^3$.

Measurements in Arctic Alaska, March 25-31, 1974

Sky brightness and solar intensity were measured near Barrow, Alaska at the NOAA background observatory ($71^{o}19'N$, $156^{o}37'W$). The sky was completely clear during the entire period March 26 to March 31; winds were out of the northeast at approximately 8 $msec^{-1}$ and the mean day air temperatures were typically about -20 to $-24^{o}C$. All local sources of man-caused pollution (i.e., the village of Barrow and various military radar stations) were downwind during the entire measurement period. A rough trajectory analysis at the 700mb level indicates that the air had passed almost directly over the North Pole and had veered down over the northern extremities of the Canadian Arctic hence into Barrow.

Unfortunately, the sky-brightness collimator photometer was not available at Barrow. The sky intensity measurements were carried out entirely with the coronameter at a mean wavelength of λ = 550nm and mean scattering angles of 1.10^{o} and 6.2^{o}. Optical depth, derived from sun photometry, was measured at λ = 500, 660, 700, 750, 850, 950, and 1,000 nm. In addition, although they will not be discussed here, vertical profiles of aerosols were made with an airborne sun photometer. The optical measurements were supplemented with acoustic sounder measurements of the boundary layer which were being carried out at the time in conjunction with the 1974 Lead experiment being conducted jointly by the Universities of Oregon, Washington and Alaska. Also, in conjunction with the "lead experiment" ice crystals in the free atmosphere were replicated and analyzed.

During the entire period mentioned above, one would expect, in view of the conditions, that the air clarity would be excellent; there were

no obvious sources of pollution or dust since the Arctic Ocean was frozen and the surface was covered with a hard windblown snow pack. However, visual observations indicated that there was a haze present in the atmosphere. The horizontal visibility was estimated to be between 10 and 20 km, although this is difficult to reckon because of a lack of reference points on the flat Arctic tundra. We did, however, attempt to determine the horizontal visibility more accurately on one or two occasions by making airborne observations. These involved flying at a constant altitude of several hundred feet until a reference point, such as a barrel or a caribou, appeared to "emerge" out of the haze; it was then a simple matter of flying toward the object at a known airspeed and measuring the time interval from "first sighting" until the airplane passed directly over the object. Typically, the values of horizontal visibility obtained in this fashion, varied between 10 to 20 km. In addition to the low lying haze near the surface, there were also indications that elevated haze layers existed at altitudes of one to two km. Some of these layers appeared brownish-yellow probably reflecting the fact that the aerosols in the haze layers had absorbtion features in the visible region.

In addition to the multi-wavelength measurements of solar intensity, we also carried out broadband measurements with a Linke-Feussner Actinometer with OG1, RG2 and RG8 Schott-glass cut-off filters.

Generally speaking, the optical depths and circumsolar sky radiance were large; much larger than one might expect for clear polar air. Figure 24 shows values of optical depth arising from scattering and absorbtion by aerosols as a function of wavelength. Notice that the optical depth at 950nm is anomalously large; this is due to the $\rho\sigma\tau$ water

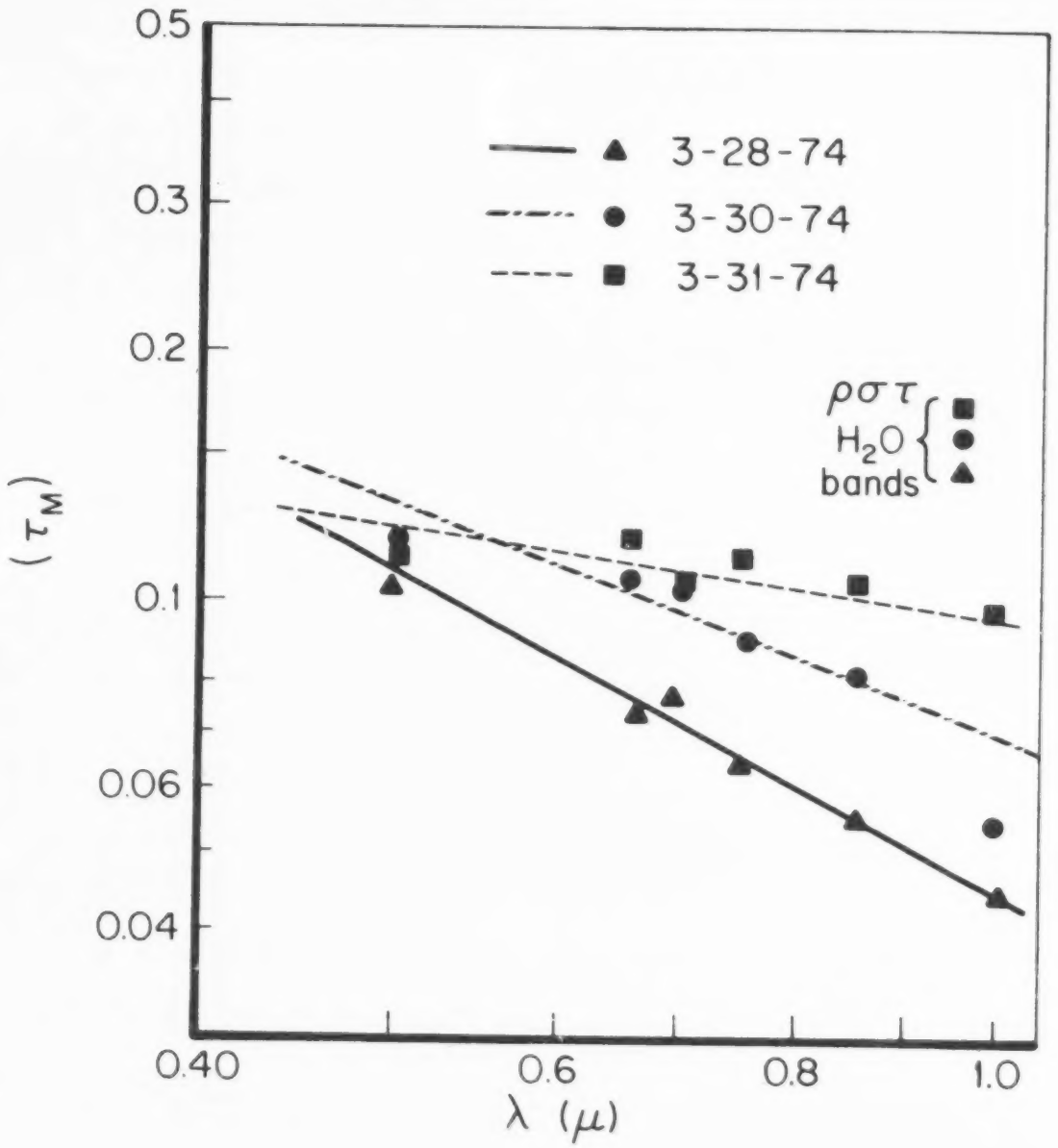

Figure 24 Aerosol optical depth versus wavelength for 3 days in March 1974, Barrow, Alaska.

vapor absorption features. In principle, one can determine the precipitable water content in the atmosphere from the ratio $\tau(950)/\tau(1000\text{nm})$. We are now calibrating this optical-hygrometer.

It is interesting and heartening to observe that the course of optical depth with wavelength seems to obey a λ^{-n} type of dependency which one would expect if the aerosols were distributed according to a Junge power-law distribution over a sufficiently large range of particle radii. Figure 25 shows the relation between the ratio of columnar mass loading to aerosol optical depth, τ/τ_M, as a function of wavelength λ, for a Junge power-law distribution. These curves were calculated using the Mie theory, with an index of refraction = 1.54 + i0.0, and a mass loading of 50μg m^{-3}. As can be seen from Figure 25, the Junge distribution generally gives, at least approximately, (with the degree of approximation depending slightly upon the choice of r_1 and r_2) a λ^{-n} dependency.

The circumsolar sky intensity was measured at Barrow with the sky brightness coronameter at mean scattering angles of 1.1^o and 6.2^o. A remarkably large variation occurred from day to day and even during shorter time periods measured in minutes. Figure 26 is an example taken from a chart record that shows the temporal variation in sky intensity with time. The circumsolar sky intensity at a scattering angle of 1.1^o varied much more than at 6.2^o.

We believe that the cause of the large sky intensity and atmospheric extinction at Barrow is due primarily to the presence of ice crystals which form at a high humidity region near the top of the mixing layer. According to the acoustic sounder records, the mixing depth at Barrow is approximately 200 meters thick. We found that there was a

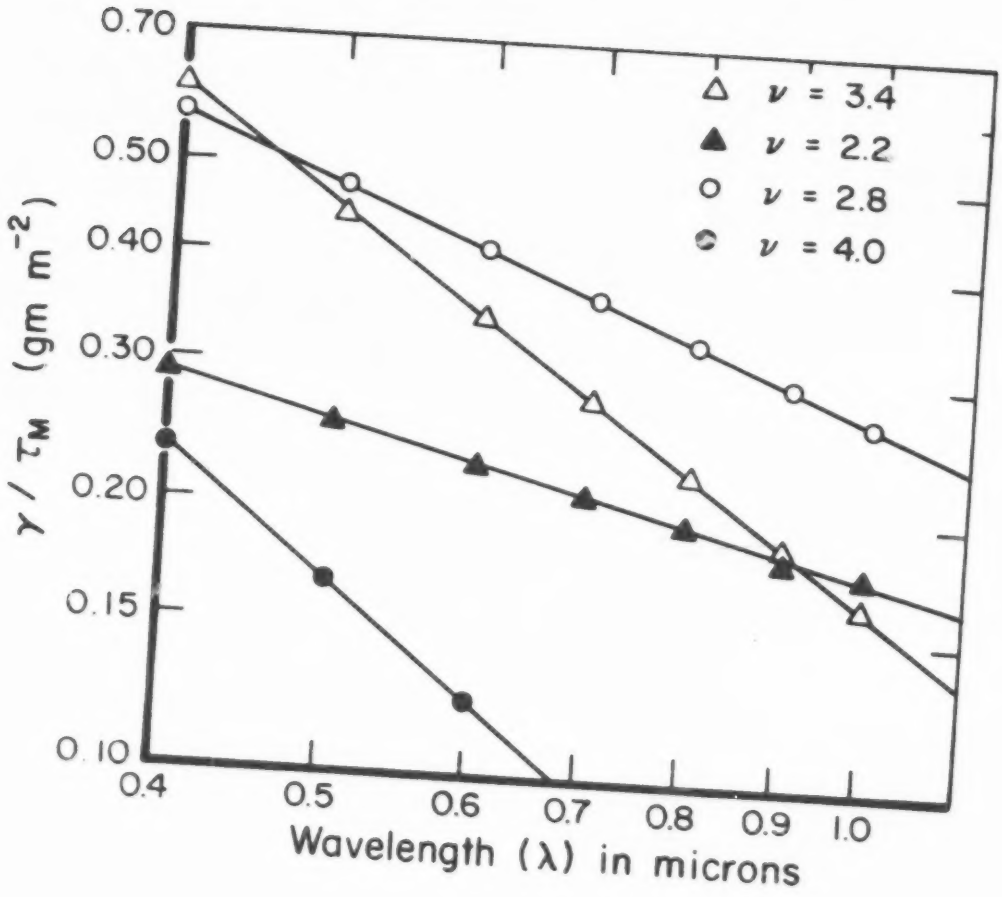

Figure 25 Volume extinction coefficient versus wavelength calculated for Junge size distribution function and constant volumetric mass loading for various combinations of lower, r_1, and upper, r_2, cutoff radii.

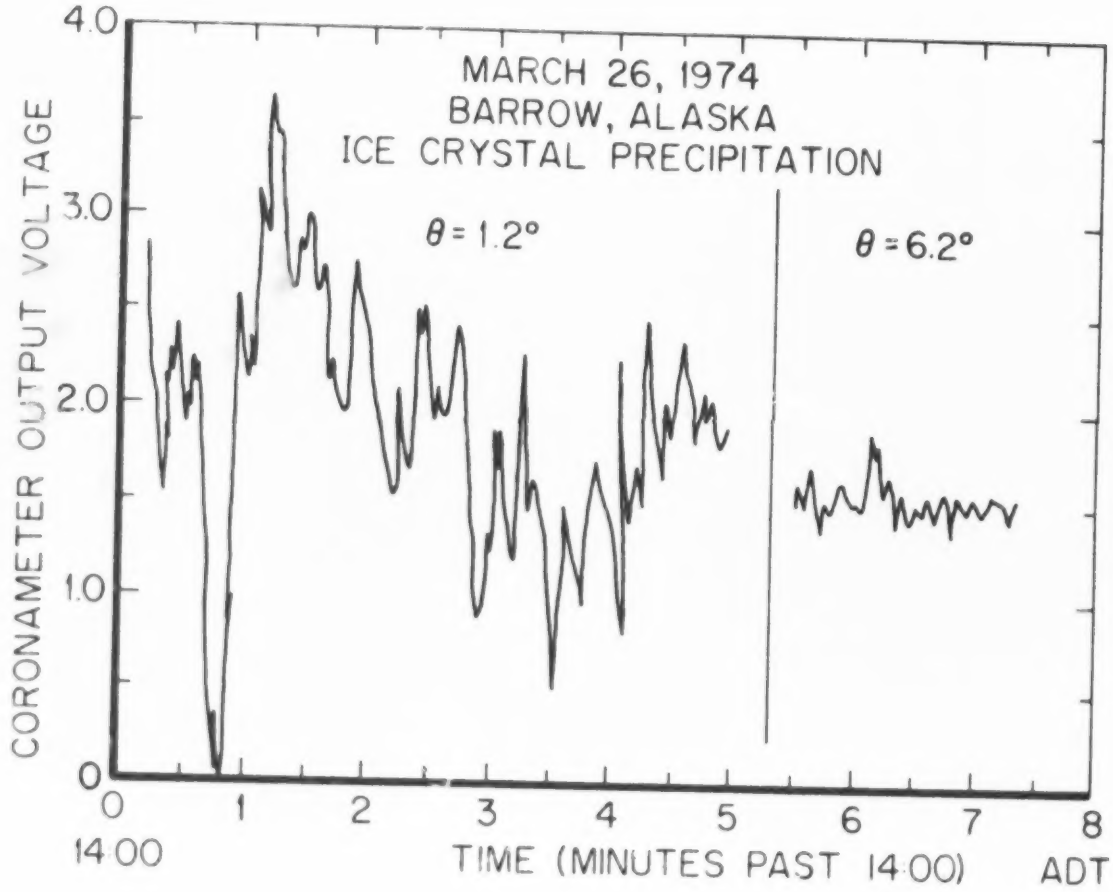

Figure 26 Temporal variation of coronameter output voltage, Barrow, Alaska.

diurnal variation in mixing depth with larger (i.e. 250m) values found during mid-day and smaller values (i.e., 150m) typically occuring at night. From radiosonde data, and also from airborne temperature measurements we found that the mixing layer is generally "capped" by an elevated inversion with a strength of approximately $5^{o}C$. From the observations, it appears that the onset of ice crystal precipitations are associated with the daytime expansion of the mixing layer, most likely as the elevated inversion passes through humid layers to cause super saturations. The radiosonde data often show a 100% humidity (with respect to water) layer which is, we think, the responsible agent for the ice-crystal precipitations.

In keeping with the aforementioned theory of ice-crystal formation, we noticed that the ice crystal precipitation seems to start within an hour or so from local noon; at that time, as the ice crystal concentration increases, the sky intensity, especially near the sun (at 1.1^{o} scattering angle) increases manyfold. As an example of this we show in Figure 27 a record of the sky intensity on March 26th. Coincident with the high values at mid-morning, we observed optical effects including circumzenith arcs, and 22^{o} and 46^{o} halos around the sun.

One would expect the diffraction of light around large (200μ dia) ice crystals to produce a strongly peaked phase function. The steepness of the brightness gradient, $I(1.1^{o})/I(6.2^{o})$, of the circumsolar intensity supports the assertion that there are large aerosols (ice crystals) in the atmosphere. Thus it is quite clear that, at least on many occasions, the ice crystals in the Arctic atmosphere are responsible for

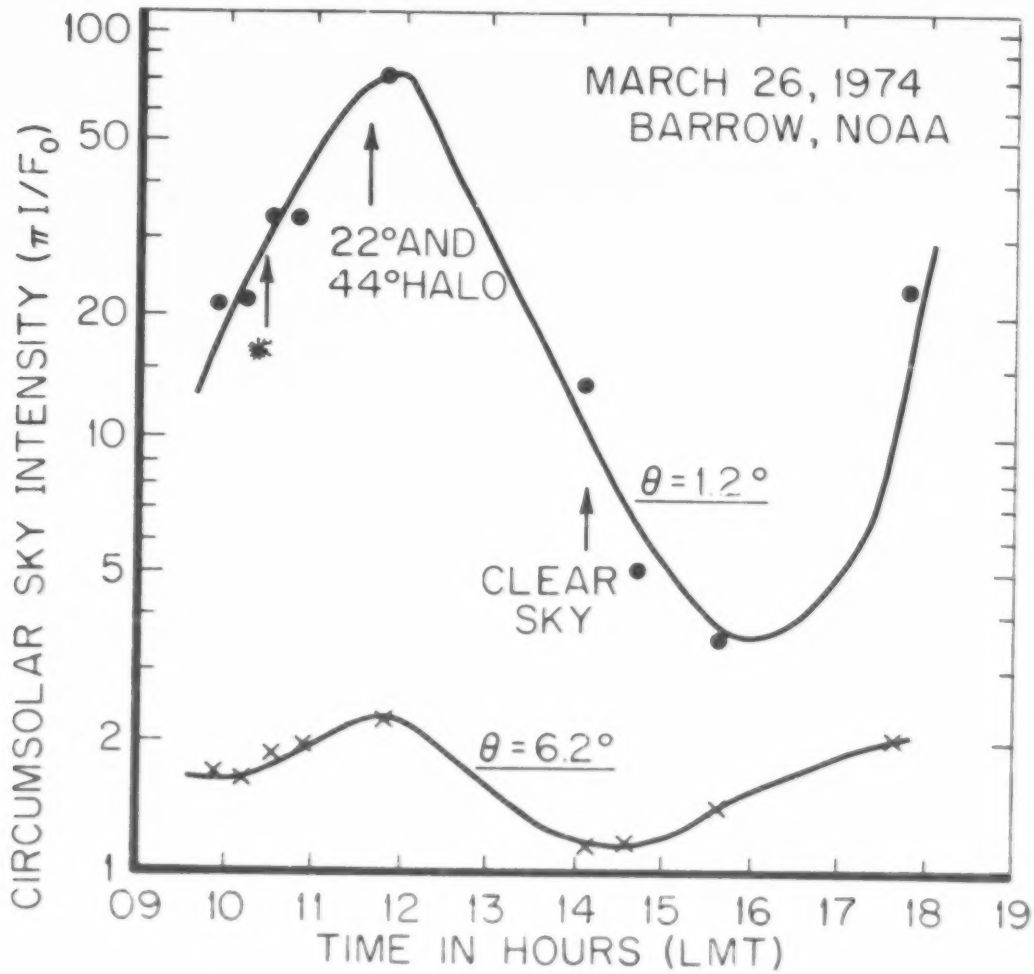

Figure 27 Diurnal variation of circumsolar sky intensity at angular distances of 1.2° and 6.2° from the sun's limb on March 26, 1974 at Barrow, Alaska.

causing a large modification in sky intensity. Their presence almost certainly cannot be neglected when assessing the heat budget of the earth-atmosphere system.

In addition to the ice crystals, as we remarked earlier, there are apparently some other types of aerosols present in the Arctic atmosphere as evidenced from the yellowish streaks that were observed near the horizon, from an altitude of one to two km, and also from the fact that exposed millipore filters turned grey after passing air samples through them. The aerosols were sampled with a flow-rate of 30 l/sec, an exposure time of twenty-four hours, and a cross-sectional filter area of 10.0 cm^2. The pore size was 8μ diameter. On every occasion, for a total of six days, the filter collected enough aerosols to form a visible film. Optical spectrophotometric measurements are presently being made of the deposited aerosol film and preliminary results indicate that the optical depth due to these aerosols is approximately 10% of the total observed optical depth (at the mid-visible, λ = 550nm). We tentatively conclude that the ice crystals are primarily responsible for the observed anomalies in circumsolar radiation and atmospheric extinction, but, in addition, there may be another "chemical aerosol," possibly nitrates for example, which may be present, and due to absorption, could conceivably have an effect on the heat budget in the Arctic Basin. This conclusion is surprising since the relevant air mass had had a long trajectory extending for thousands of kilometers over frozen ice and snow. Six days prior to our observation, according to a geostropic trajectory analysis at the 700mb level, the air mass was in the vicinity of northeast United States. It may be possible that the observed absorbing chemical aerosols had come from man-caused pollution.

Measurements on May 2, 1974

We conclude our examples of sky brightness measurements with some observations made on May 2, 1974, from the roof of the C.T. Elvey building at the University of Alaska's Fairbanks campus. This example is especially important for two reasons:

a) The sky was absolutely clear of clouds and no mottling or inhomogenities could be seen; the sky appeared utterly homogeneous and dark blue, and

b) At the time of these measurements, the equipment which had been under development during the course of this study was reasonably complete and this was an excellent opportunity to operate all of the instruments simultaneously so intercomparisons could be made.

Conditions were as follows: the winds were from the NE to E at approximately 4 $msec^{-1}$; snow had melted and the surface was approximately 80% exposed. During the entire period, there were no clouds. The high sky purity was impressive.

Figure 28 illustrates the sky intensity in the solar almucantar on May 2, 1974. The measurements were made with a well-baffled collimator photometer up to 10^{o} from the sun; triangles mark the coronameter readings. Figure 29 shows the Langley plot of the direct sun radiation and Figure 30 shows the wavelength dependence of the aerosol extinction (optical depth). The aerosol source very likely resulted from surface material mixed upward, or possibly advected in from the NE. Vegetation was, for the most part dormant, and it is therefore unlikely that turpines could have been a major contribution (Went, 1966) to the aerosol loading for this particular period.

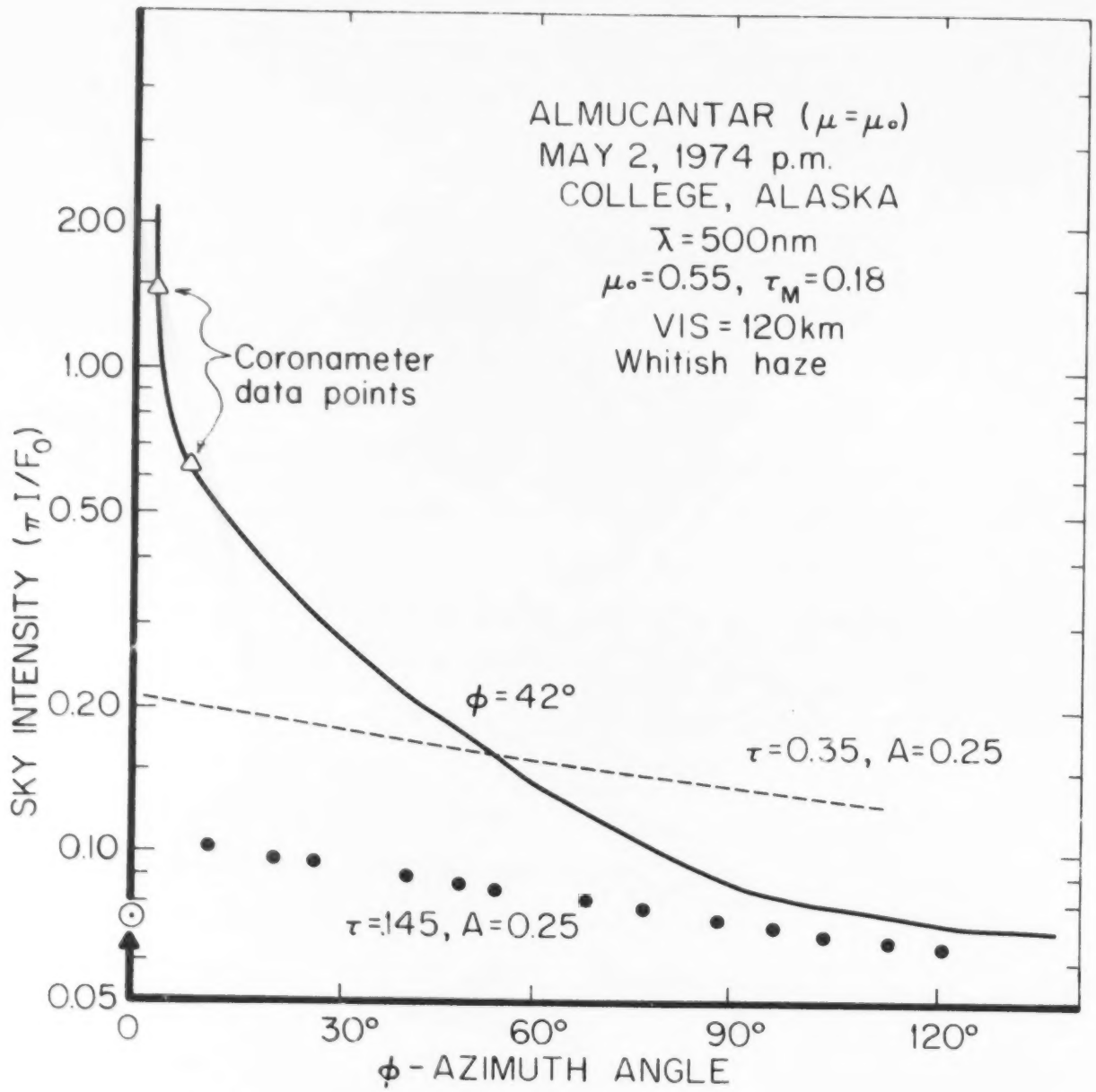

Figure 28 Sky intensity, $\pi I/Fo$, in the solar almucantar on May 2, 1974, λ = 500nm, College, Alaska.

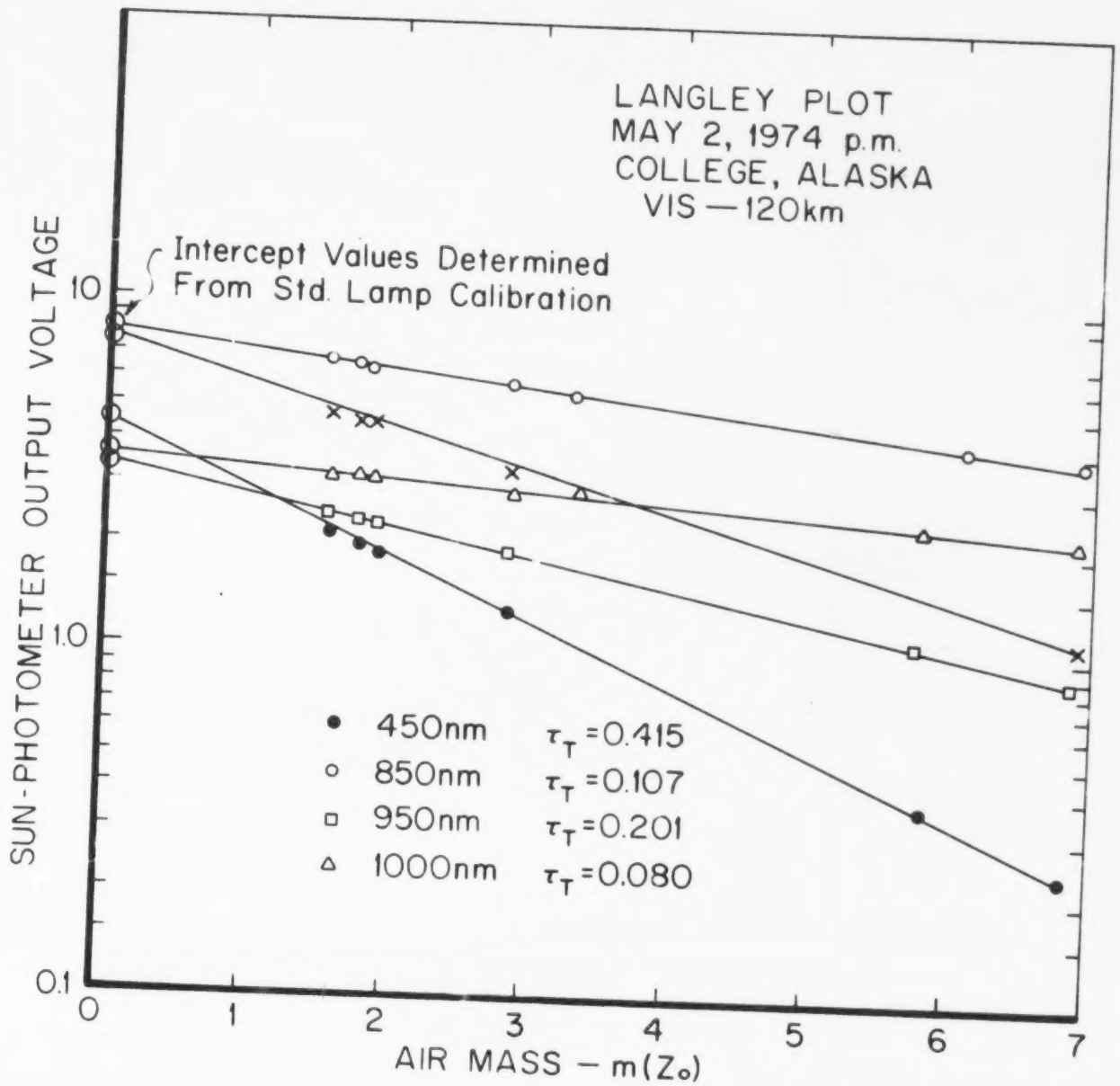

Figure 29 Langley plot of direct-sun data on May 2, 1974 at College, Alaska.

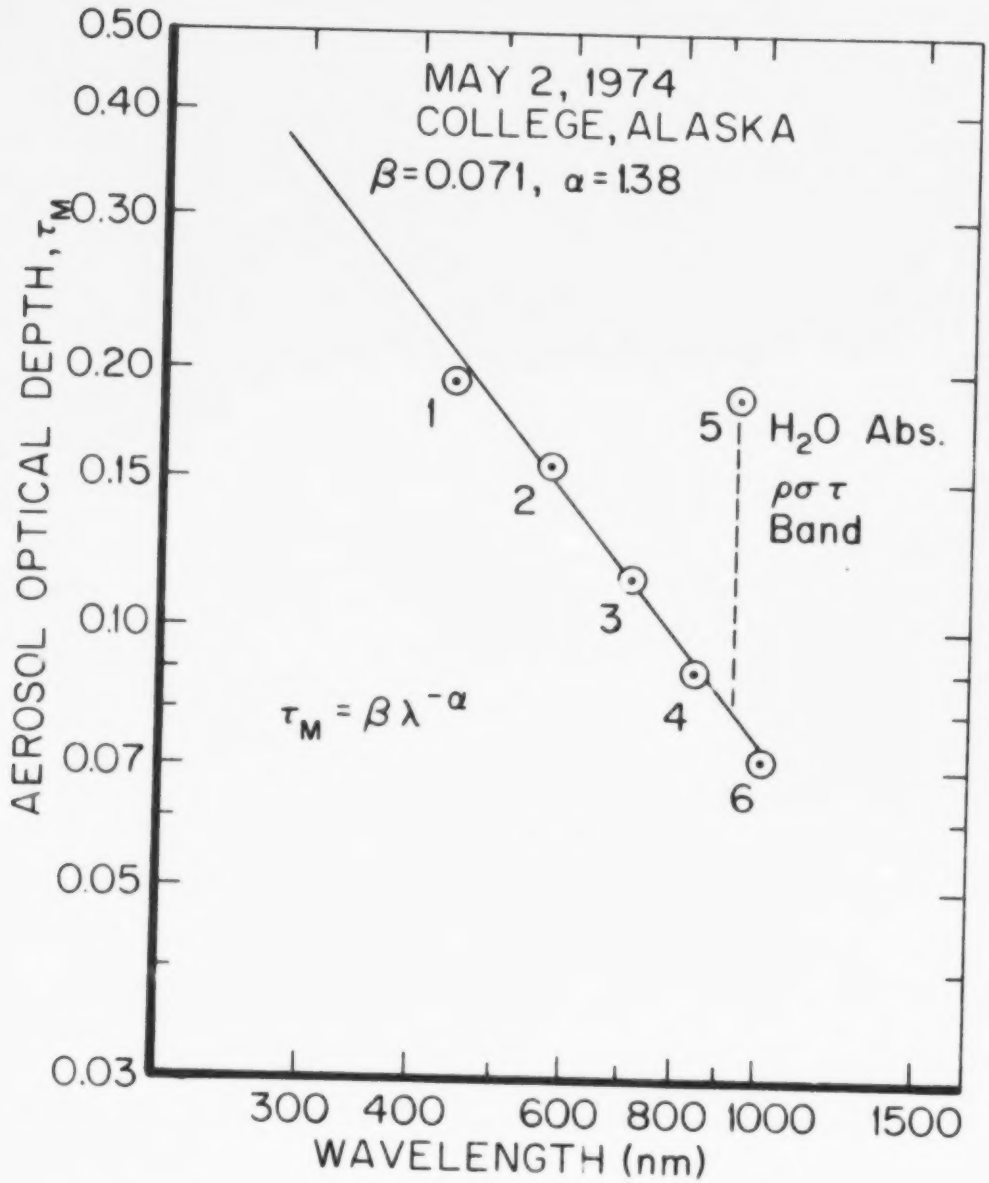

Figure 30 Wavelength dependency of aerosol optical depth on May 2, 1974 at College, Alaska.

THE RELATION BETWEEN THE JUNGE POWER-LAW EXPONENT AND THE AUREOLE BRIGHTNESS GRADIENT

As has been mentioned previously, suspended aerosols in the atmosphere strongly diffract light into the near forward directions. At least for the larger aerosols ($r>1\mu$), the distribution of scattered energy is in rough accord with results predicted by classical Fraunhofer diffraction theory. That is, the angular extent of the primary diffracted energy increases as the scattering particle size decreases. Therefore, small scatterers will yield a relatively large aureole while larger aerosols will diffract energy into a relatively smaller core. If size distribution of aerosols were mono-disperse, one would observe colored diffraction rings around the sun; however, this usually does not happen in practice because of coagulation resulting from Brownian motion and precipitation due to gravity acting together to yield a broad aerosol spectrum covering a wide range of particle radii. Theoretical analysis by Freidlander (1961) shows that a power-law distribution function of a form suggested by Junge, would result in a steady-state situation of coagulation-gravitational fallout.

In view of what has just been said, we see that the hypothetical "diffraction pattern" formed by a mono-disperse distribution of particulates in the atmosphere would be blurred and one would expect instead to find a diffuse whitish glow around the sun superimposed on the blue sky, and this is exactly in accord with what one generally observes (except in special rare cases, Deirmendjian, 1971). However, from the arguments just presented, the intensity gradient close to the sun will depend on the steepness of the aerosol size distribution function. All

other factors being equal, a rapidly falling spectrum (large power-law exponent, ν) will have relatively more small particles per unit volume than a size distribution with a more gradual fall-off of number concentration with increasing radii (small value of ν). We conclude that large values of ν will be associated with a larger, more homogeneous aureole than the converse.

Numerical modeling using Mie theory to generate aerosol scattering phase functions, $P(\theta)$, for the Junge size distribution with different values of ν shows that this is indeed the case. Figure 31 illustrates the intensity gradient, $I(1.2^{o})/I(6.5^{o})$, as a function of the Junge power-law exponent, ν. We see that the ratio approaches unity for large values of ν, which indicates that, at least within an angular distance less than 6.5^{o} from the sun, the aureole would be homogeneous and flat (lacking a brightness gradient) if ν were numerically equal to 4.0. On the other hand, a small value of ν, say $\nu = 2.5$ as we find to be typical for windblown dust, gives a strongly peaked brightness gradient with a ratio of $I(1.2^{o})/I(6.5^{o})$ equal to about 4.

To eliminate the effects of molecular scattering, one must first subtract out the Rayleigh "blue sky" from the observations and use the subtracted intensity values. These values are designated with a subscript "M" in Figure 31, and they more closely resemble the brightness gradient for the aerosol component alone.

Assuming that a Junge power law distribution adequately describes the aerosol spectrum, then the exponent value, ν, can simply be determined from the ratio of the coronameter's readings by using the curve in Figure 31. Conversely, if one begins with a size spectrum such as

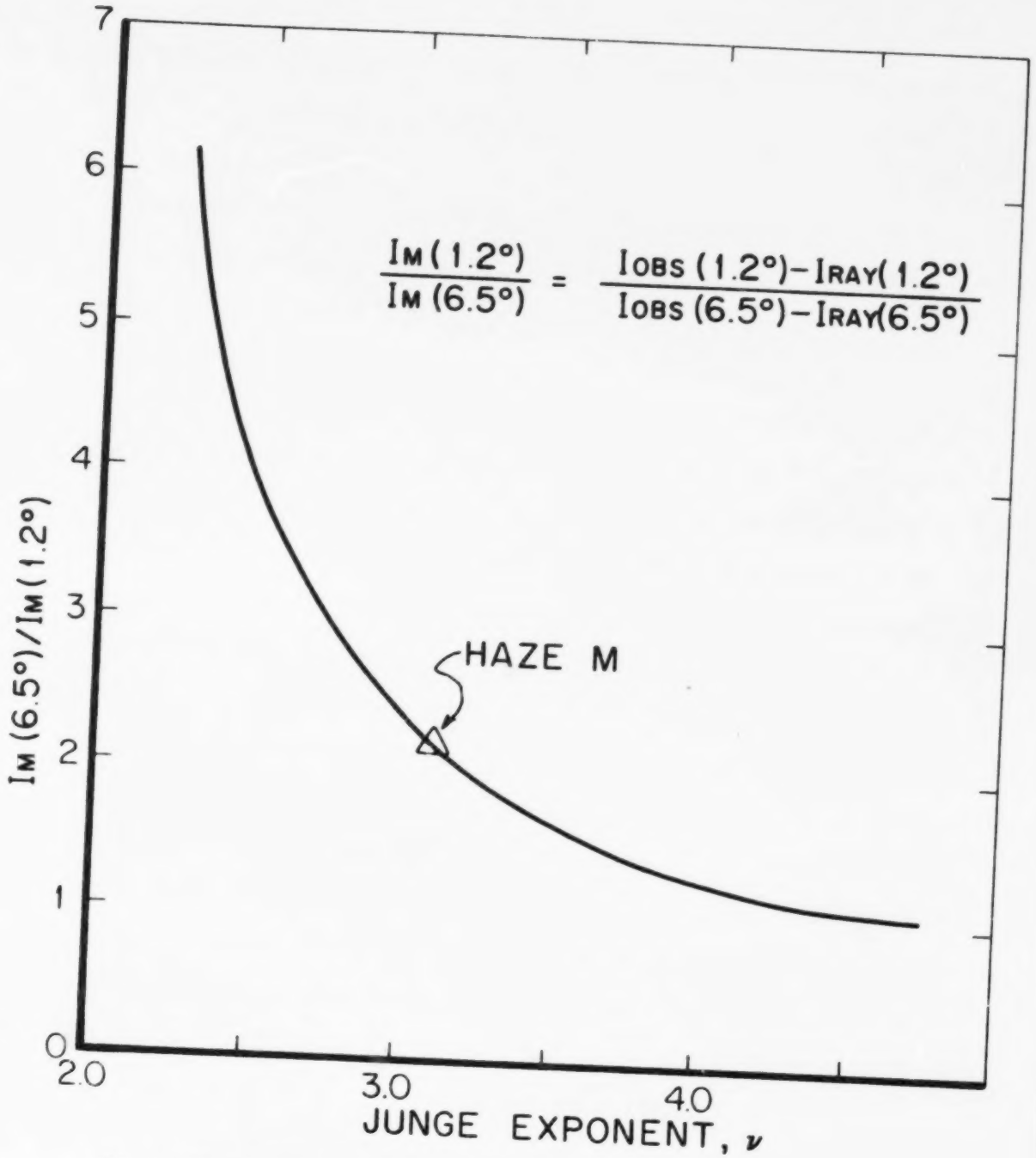

Figure 31 Ratio of sky intensity at 1.2^0 and 6.2^0 as a function of the Junge power-law exponent, ν.

that given by Deirmendjian as HAZE M, the brightness gradient can be found on the ordinate opposite the appropriate point on the curve in Figure 31. Of course, to be more accurate and quantitative, one should evaluate (by using the method that we have described) the aerosol scattering phase function out to 30 or 40 degrees and relate the curve to a size distribution function by either a formal inversion process or by using a curve-matching technique. As we have pointed out before, however, the accuracies with which one can actually determine the phase function is limited by a combination of such things as uncertainities in surface albedo, instrument absolute calibration, inherent difficulties in the perturbation approximations, etc. We feel, after having taken much data and worked with the numbers, that one can probably not use the photometer measurements of the aureole to derive extremely fine structure in the size distribution function, and, again, we find that a simple function such as the Junge power-law distribution or the modified gamma function can be made to fit by choosing various parameters within the limits of the uncertainties.

In summary, a Junge size distribution seems to be a reasonable first choice when attempting to match sky brightness data with calculated curves. Usually the results are quite consistent (at least for continental aerosols, the only ones which we have studied), and the aureole brightness gradient, $I(1.2^{o})/I(6.5^{o})$, provides a simple means for estimating a quantitative index (value of ν) of the aerosol size distribution.

References

Allen, C. W., Astrophysical Quantities, 2nd Ed., University of London, The Athlone Press, London, 1963.

Bullrich, K., "Scattered radiation in the atmosphere," Advances in Geophysics, 10, Academic Press, N.Y., 1964.

Chandrasekhar, S., Radiative Transfer, New York, Dover Publications, 393 pages, 1950.

Coulson, K. L., J. V. Dave, and Z. Sekera, Tables Related to Radiation Emerging from a Planetary Atmosphere with Rayleigh Scattering, Berkeley and Los Angeles, Univ. of California Press, 548 pages, 1960.

deBary, E., B. Braum, and K. Bullrich, Tables related to light scattering in a Turbid Atmosphere, Vol. 1, 2 and 3, Air Force Cambridge Research Laboratory Report, AFCRL-65-710, 1965.

Deirmendjian, D., Electromagnetic Scattering on Spherical Polydispersions, American Elsevier, New York, 1969.

Deirmendjian, D., Use of Scattering Techniques in Cloud Microphysics Research 1. the Aureole Method., RAND report R-590-PR, October 1970.

Diermendjian, D., Global Turbidity studies I, RAND Report R-886-ARPA, October 1971.

Eddy, J. A., The stratospheric solar aureole, Ph.D. Dissertation, University of Colorado, Boulder, Colorado, 1961.

Eiden, R., Calculations and Measurements of the Spectral Radiance of the Solar Aureole, Tellus XX, p. 380, 1968.

Elsasser, H., The Zodiacal Light, Planet. Space Science, 11, 1015-1033, 1963.

Elterman, L., UV, Visible and IR Attenuation for Altitudes to 50km, 1968, AFCRL Report No. 68-0153, Environmental Research Paper No. 285, Bedford, Massachusetts, April 1968.

Evans, J. W., A Photometer for Measurement of Sky Brightness Near the Sun, JOSA, 38, #12, 1083, 1948.

Fletcher, J. O., The Heat Budget of the Arctic Basin and its Relation to Climate, United States Air Force Project RAND Report R-444-PR, October 1965.

Freidlander, Theoretical considerations for the Particle size spectrum of the Stratospheric Aerosol, J. of Meteor., 18, 753, 1961.

Green, A., A. Deepak and B. Lipofsky, Interpretation of the Sun's Aurecle Based on Atmospheric aerosol models, Applied Optics, 10, No. 6, 1263, June 1971.

Herman, B. M., S. R. Browning and R. J. Curran, The Effect of Atmospheric Aerosols on Scattered Sunlight, J. Atmos. Sci., 28, No. 3, 419-428, April 1971.

Joseph, J. H., A. Manes and D. Ashbel, Desert aerosols transported by Khamsimic depressions and their climatic effects, J. Applied Meteor., 12, 792-797, 1973.

Junge, C. E., Air Chemistry and Radioactivity, Academic Press, New York, 382 pages, International Geophysical Series-Volume 4, 1963.

Kasten, F., A new table and approximate formula for the relative optical air mass, Tech. Dept. 136, CRREL, AD610554, 1964.

Lloyd, J. W. F. and S. M. Silverman, Measurements of the Zenith Sky Intensity and Spectral Distribution during the Solar Eclipse of 12 November 1966 at Bage, Brazil, and on an Aircraft, Applied Optics, 10, No. 6, 1220, June 1971.

Mie, G., Beitrage zur Optik Truber Medien, Annalen der Physik, 25, January 1908.

Mitchell, J. M., Jr., The Effect of Atmospheric Aerosols on Climate with Special Reference to Temperature Near the Earth's Surface, Journal of Applied Meteorology, 16, 703, 1971.

Rasool, S. I. and S. H. Schneider, Atmospheric Carbon Dioxide and Aerosols Effects of Large increases on Global Climate, Science, 173, 138-141, 9 July 1971.

Shaw, G. E., Sky brightness and polarization during the 1973 African eclipse, Appl. Optics, February 1975.

Stair, R., W. E. Schneider and J. K. Jackson, A new standard of spectral irradiance, Applied Optics, 2, No. 11, 1151-1154, 1963.

Thekaekara, M. P., Solar irradiance measurements from a research aircraft at 38,000 feet, Report X-322-66-304 (Goddard Space Flight Center, Greenbelt, Maryland) August 1968.

Van de Hulst, H. C., Light Scattering by Small Particles, John Wiley and Sons, New York, 1957.

Went, F. W., On the nature of Aitken condensation nuclei, Tellus, 18, 549-556, 1966.

APPENDIX A UNITS OF SKY BRIGHTNESS

Units of Sky Brightness

Diffuse intensity is expressed in a bewildering array of units. Each discipline (astronomy, aeronomy, meteorology etc.) seems to have its preferred system. For the benefit of the reader who may want to express intensity measurements in other units, we present a discussion of the commonly used units and the relation among them.

a) Physical units of absolute intensity, $I_p(\lambda)$, (commonly expressed in $\mu w\ cm^{-2}\ nm^{-1}\ sr^{-1}$, identical to erg $cm^{-2} sec^{-1} \text{Å}^{-1}$).

The power passing through an aperture of a photometer, $p(\lambda)$, having a circular field of view of angular diameter, θ, is,

$$p(\lambda) = I_p(\lambda)\, dA\, d\omega\, d\lambda \qquad A1)$$

where, for example, p is the radiant power in microwatts, dA is in cm^2, $d\omega = \theta^2/4$ (θ measured in radians), and $d\lambda$ is a wavelength interval in nm.

b) Sky intensity expressed in units of mean sun brightness, $B(\lambda)$.

Solar astronomers often express sky intensity in "millionths of the sun's brightness." The following expression defines $B(\lambda)$:

$$B(\lambda) = I_p(\lambda)\, \frac{d\omega_o}{F_o(\lambda)} \qquad A2)$$

where I_p is expressed in $\mu w, cm^{-2} nm^{-1} sr^{-1}$ then F_o, the extraterrestrial solar flux, would have to be in $\mu w\ cm^{-2} nm^{-1}$. $d\omega_o$ is the solid angle of the sun as viewed from earth. ($d\omega_o = 5.95 \times 10^{-5} sr$). It should be remembered when using intensity expressed in units of mean sun brightness, that the values are referenced to the extraterrestrial value of solar flux and not to the observed ground-level solar flux which is smaller due to atmospheric extinction.

c) Sky intensity expressed in rayleighs/angstrom, R′.

This unit is in common usage among researchers in aeronomy as a means of expressing the volume emission of the airglow integrated along the line of sight as equivalent to a surface brightness. To prevent confusion one should remember that there are two distinct situations: 1) expressions for the total intensity of an individual spectral line (such as the forbidden atomic oxygen line at 5577Å). In this case, the brightness is expressed in "rayleighs," R. 2) expressions for the brightness of an extended source with a continuum-type of spectrum. An example is the non-resonant scattered sunlight in the atmosphere. In this case one must express the intensity in per-unit wavelength interval (rayleighs per angstrom, R′).

The intensity of an extended object (not a point object) in rayleighs/Å is defined as:

$$R'(\lambda) = 4\pi \times 10^{-6} \frac{n}{d\omega\, dA\, d\lambda} \qquad A3)$$

where n = photon flux entering the photometer aperture (sec^{-1})

$d\omega$ = solid angle of the photometer's field of view (sr)

dA = entrance aperture in cm^2

$d\lambda$ = wavelength width in Å

The photon number density, n, (sec^{-1}) is given by,

$$n = \frac{\lambda p}{hc} \qquad A4)$$

where λ is the wavelength (m)

p the incoming power (watts)

h = Plancks constant = 6.624×10^{-34} joule-sec

c = speed of light = 3.00×10^{8} (m/s)

for mid-visible light at a wavelength of 550 nm, $n = 2.76 \times 10^{18} p$ (sec^{-1}).

Equation A1, A2, and A3 can be combined to yield a convenient relation between intensity $I_p(\lambda)$ in ($\mu w\ cm^{-2} nm^{-1} sr^{-1}$) and $R'(\lambda)$ (rayleighs/Å):

$$R'(\lambda) = 6.32 \times 10^6 \lambda_m I_p(\lambda) \qquad A5)$$

where λ_m = mean wavelength in μm.

d) Stellar magnitude, m_v

Stellar magnitudes are used by astronomers to express radiant flux (not intensity). They are commonly used to express the brightness of stars. The absolute stellar magnitude, m_v, is related to absolute incoming flux $F(\lambda)$ by,

$$\log_{10} F(\lambda) = 0.40 m_v - 8.42 \qquad A6)$$

where F is in ($\mu w\ cm^{-2} nm^{-1}$).

e) Chandrasekhar's convention for radiant flux

The definition of radiant flux, F_c, as given by Chandrasekhar (1950) incorporates a factor of π which in the past has caused some confusion. A case in point is the somewhat common practice of expressing intensity in units of incoming flux. For example, in the well-known tables of Coulson et al., are listed solutions to the equations of transfer for Rayleigh scattering atmospheres, and the intensity values are expressed in units of incoming flux, assuming a radiant flux which has incorporated the value of π in its definition. In using such numerical tables, one must use care in the interpretation of the values.

Flux, as defined by Chandrasekhar, is,

$$F_c(\lambda) = \frac{1}{\pi} \int I(\lambda) \cos\theta d\omega \qquad A7)$$

which has the advantage of yielding $F_o = I$ for an isotropic radiation field.

On the other hand, in solar radiation work it is common to drop the factor of π and to express the solar flux, instead, as simply:

$$F_o(\lambda) = \int_{\omega_o} I(\lambda) \cos(\theta)\, d\omega \qquad \text{A8)}$$

where the integral extends over the solar disk. This is the definition that was used for flux in part b) of this section.

Thus, if one uses the tables of Coulson et al., the sky intensity, $I(\lambda)$, is related to the tabulated values, TV_c, as follows,

$$. \; TV_c = \frac{I(\lambda)}{F_o(\lambda)} \pi \; . \qquad \text{A9)}$$

In DeBary et al.'s tables (1965), the tabulated values of diffuse sky intensity are expressed directly in units of cal $cm^{-2} min^{-1} sr^{-1} (100\text{Å})^{-1}$ assuming that the extraterrestrial flux is given by the Tables of Nicolet (1951).

f) Numerical examples of diffuse intensities and direct fluxes for various sources.

It is perhaps useful to present a table giving the intensity of various natural objects in terms of the above definitions so that the the numbers can be compared, and so one can obtain a more quantitative "feeling" for the brightness of natural objects. Table A1 lists the intensities and fluxes for commonly observed sources of interest. One should realize that in some cases, the actual brightness of objects varies depending upon conditions.

Table AC-1

Radiant Intensities of Some Natural Sources at λ=550nm.

Source	Intensity $I_p(\lambda)$ ($\mu wcm^{-2}nm^{-1}sr^{-1}$)	B(2) (In units of solar brightness)	$R'(\lambda)$ (Rayleighs/Å)	m_v^* Magnitude	Remarks & References
Average solar disk	3.30×10^{6}	1.00	1.13×10^{13}	-27	Thekaekara 1968:
Zenith sky for a pure Rayleigh atmosphere	5.08×10^{0}	1.75×10^{-6}	1.74×10^{7}		Coulson, Dave, Sekera (1960) A=0, μ_0=0.6.
Full moon	1.44×10^{0}	4.97×10^{-7}	5.00×10^{6}	-12.7	Allen, 1963.
Zenith sky during total eclipse	6 to 30×10^{-4}	2.1 to 10×10^{-10}	2 to 10×10^{3}		Lloyd, Silverman, 1971 Shaw, 1974.
Zodical Light	1.15×10^{-6}	3.97×10^{-13}	4.00×10^{0}		Elsassar, 1963, $\phi = 30^0$
Stellar Background at Galactic Pole	1.20×10^{-7}	4.14×10^{-14}	4.4×10^{-1}		Allen, 1962 100 10th mag. stars per square degree
Darkest Night Sky at Galactic Pole	2.9×10^{-9}	1.00×10^{-15}	1.0		Kitt Peak Observatory publication

*Stellar magnitudes pertain only to objects with finite angular dimensions such as the stars, sun or moon.

APPENDIX B

COMPUTATION OF GEOMETRICAL PARAMETERS

A. The Solar Zenith Angle

The zenith angle of the sun, z, is computed by solving the celestial triangle. In terms of terrestrial coordinates, it may be expressed as,

$$\cos(z) = \sin \ell \sin \delta + \cos \ell \cos \delta \cos H \qquad B1$$

where ℓ = observer's latitude

δ = solar declination at time of observation

H = solar hour angle measured westward from the southern meridian.

The sun's hour angle, H, is computed according to the formula,

$$H = LST + SLD - LLD - E + 12 \text{ hr.} \qquad B2$$

where the symbols refer to times units as follows:

LST is the Local Standard Time of the observation,

SLD is the standard time zone difference, in hours, to the prime meridian;

LLD is the longitude of the observation site in units of time (15^{o} per hour of time); and

E is the equation of time.

One may determine E for the time and date of observation from an ephemeris tabulation, or it can be calculated by using:

$$E = 2e \sin(l_o - w) - \tan(\tfrac{C}{2})^2 \cdot \sin(2\, l_o) \qquad B3$$

where e = eccentricity of earth's orbit

l_o = longitude of sun,

w = longitude of sun's perigee,

C = obliquity of the ecliptic.

Preceding page blank

The terms e, w and C can be taken from an ephemeris for any given year. Equation B3 has the advantage that it may be used to make calculations for multiple periods in any given year thereby saving looking up E for each observation period which can become inconvenient if large numbers of observation dates are to be calculated.

The solar longitude, l_o, is measured along the ecliptic from the first point of Aries. It can be easily computed from

$$l_o = (D_{eqn} - D_{obs})\ 360/365.25 \qquad \text{degrees} \qquad \text{B4}$$

where D_{eqn} and D_{obs} represent the dates (in decimal days from an arbitrary reference point, say January 1 at 00 hours) for the local equinox and the observation date respectively.

B. The Air Mass, m(z).

The solar air mass, m(z), represents the amount of absorbing/scattering medium, in a unit cross-sectional area, through which an incoming ray from the solar disk passes. It is measured in units of absorbing/scattering material for a ray entering from the local zenith direction. For relatively large solar elevation angles, the air mass can be derived to a high degree of approximation by considering the atmosphere to be a horizontally homogeneous plane parallel layer. For such a model, the air mass is simply given as,

$$m = \sec(z) \qquad \text{B5}$$

When the sun's elevation angle becomes small, the curvature of the atmosphere can no longer be neglected and the sec(z) expression becomes progressively more inaccurate. In instances of low sun angle, the air mass must be calculated by integrating along the absorption and scattering medium encountered by a ray bundle of incoming solar rays con-

tained in a unit area and passing through the atmosphere. Refraction of the incoming ray by the varying atmospheric density with height must be included in the computation, particularly for solar elevation angles of a few degrees. One finds, by analysis, that the magnitude of the air mass, for low sun angles, becomes dependent on the nature of the vertical distribution of aerosols and gaseous molecules. Tables have been constructed by several investigators for various kinds of model atmospheres giving the air mass as a function of "apparent" zenith angle. We used the tables prepared by Kasten (1964) which list the air mass function for an ARDC model atmosphere.

The air mass values tabulated by Kasten were fitted to an empirical expression of the form,

$$m(e) = \frac{1}{\sin e + a(e + b)^{-c}} \qquad \text{B6}$$

Kasten gives the following values for the constants in equation B6: $a = 0.1500$, $b = 3.885$, $c = 1.253$.

The formula B6 fits the computed data points to an accuracy of better than 1.5% over the entire range of elevation angles from zero to 90^{o}. For most zenith angles the accuracy is considerably better, on the order of a few tenths of one percent, completely adequate for most radiation transfer purposes.

C. Scattering Angle, θ.

The scattering angle, θ, is measured along a great circle arc from the direction specified by a zenith angle, z, and an azimuth angle, ϕ, and the direction of the sun specified by corresponding coordinates z_0 and ϕ_0; it may be expressed as,

$$\cos(\theta) = \mu\mu_0 + \sqrt{(1-\mu_0^2)(1-\mu^2)}\,\cos(\theta-\theta_0), \qquad \text{B7}$$

where μ and μ_0 refer to the cosine of Z and Z_0.

D. Effects of Altitude, h.

The air mass, m(z), is, as was explained above, referred to the amount of absorbing and scattering media in a vertical column above the observer. One should recall, however, that the absolute amount of material, and hence the extinction coefficient, depends on the observer's elevation above sea level. The effect of elevation change can be related to change in the total vertical optical depth by accounting for the pressure change. Therefore, if one has available tables of optical depth arising from Rayleigh on molecular scattering, $\tau_R(\lambda)$, evaluated for STP, then one may estimate the pressure-corrected optical depth by scaling according to

$$\tau(h,\lambda) = \tau(0,\lambda)\,\frac{p(h)}{p_0} \qquad \text{B8}$$

where p(h) and p(0) are atomspheric pressure at height h and at sea level. For most purposes one may obtain p(h) from a standard atmosphere model.